DESIGN, CONSTRUCTION, AND EVALUATION OF LOW-COST ELECTRICAL IMPEDANCE-BASED MULTIPHASE FLOW METER WITH TWO-PHASE FLOW IN LARGE DIAMETER PIPES

A Thesis

by

CRAIG RANDALL NOLEN

Submitted to the Office of Graduate and Professional Studies of
Texas A&M University
in partial fulfillment of the requirements for the degree of

MASTER OF SCIENCE

Chair of Committee,	Gerald L. Morrison
Committee Members,	Michael Pate
	Karen Vierow
Head of Department,	Andreas A. Polycarpou

December 2015

Major Subject: Mechanical Engineering

ABSTRACT

Because of the high cost of many of industry's current multiphase flow meters, there is a desire to develop low-cost solutions to the multiphase flow measurement problem. One such potential solution is an electrical impedance based device placed downstream of a slotted orifice plate. The electrical impedance based part allows one to measure the density, while the slotted orifice plate measures the total volumetric flow rate. This type of device has been proven effective for NPS 2" piping, but not for larger piping with higher flow rates and pressures. This thesis describes the design, testing, and evaluation of one such multiphase flow meter (MPFM) designed for an NPS 6" pipeline carrying an air/water mixture. The MPFM was tested in a closed loop test facility capable of operating at various flow rates, pressures, and gas volume fractions (GVFs). The test set-up also included a venturi tube flow meter downstream of the MPFM for additional flow rate verification.

The electrical impedance portion passes a multi-frequency signal through the fluid between two electrodes diametrically opposed on the pipe. The signal gain across them was measured and shown via analysis of variance (ANOVA) techniques to be correlated to total flow rate and pressure as well as the GVF of the fluid. The flow rate correlation had not been seen in smaller diameter pipes using this MPFM concept. A multi-variable regression was applied accordingly, resulting in a calibrated equation that predicted the fluid GVF with an uncertainty of ±5.85% GVF with 95% confidence.

The slotted plate flow rate data is believed to have been affected partially by the presence of large plastic pieces in its upstream piping, but removing the anomalous data showed an average

measurement uncertainty of ±8.80% with 95% confidence. The venturi was capable of predicting the flow rate with an uncertainty of ±4.53%.

Because of the interdependence of GVF and flow rate predictions, an iterative technique was used to achieve the accuracies described above. The technique assumes an initial guess for flow rate and uses that guess in the GVF prediction equation. The GVF prediction is then used in the flow rate equation to obtain a better flow rate estimate. This improved flow rate estimate is then used in the GVF equation, and the process repeats itself until flow rate and GVF converge on a solution. This technique resulted in total mass flow rate predictions with an uncertainty of ±6.14%, and GVF predictions with an uncertainty of ±5.85% GVF. These results imply that the electrical impedance-based MPFM concept is applicable to pipes as large as 6".

DEDICATION

This work is dedicated to my family, friends, and fiancé—for all of their love and support throughout the years. I owe my success to you.

ACKNOWLEDGEMENTS

My greatest thanks go to Dr. Morrison for all of his patience and guidance throughout the making of this thesis, and for his generous support of my educational goals. Secondly, I would like to thank Mr. Sujan Reddy for teaching me everything I needed to know about our test rig, and for all of his help from turning wrenches to listening to my latest theoretical musings. I would also like to thank all of my other Turbolab colleagues who were willing to lend their time, muscle, and brainpower whenever needed. Finally, I would like to thank Texas A&M University and the numerous people who have made my education not only possible, but much more enjoyable for the past 5 years.

NOMENCLATURE

V_s — Superficial velocity

Q — Volumetric flow rate

A — Cross-sectional area of pipe

V_o — Circuit output voltage

V_i — Circuit input voltage

G_x — Fluid mixture resistance

C_x — Fluid mixture capacitance

G_f — Filter resistance

C_f — Filter capacitance

ω — Excitation frequency in rad/s

f — Excitation frequency in Hz

T — Fluid mixture temperature

$Gain$ — Ratio of output signal magnitude to input signal magnitude

$\Delta Gain$ — Temperature correction factor

SS — Sum of squares of factor or interaction

$d.f.$ — Degrees of freedom of factor or interaction

MS — Mean square of factor or interaction

F — Calculated F-ratio for factor or interaction

F_{crit} — Critical F-ratio for significance at a specific confidence level

p — Confidence level

$\dot{m}$ — Total mass flow rate

P — Fluid static pressure

GVF — Gas volume fraction of fluid mixture

C_D — Discharge coefficient of slotted plate

β — Effective diameter ratio

A_f — Area of slot flow area of slotted plate

ρ — Fluid mixture density

Δp — Pressure drop across slotted plate

A_t — Total area of slotted plate

$C_{D,v}$ — Coefficient of discharge of venturi flow meter

A_1 — Pre-convergence diameter of venturi

A_2 — Converged diameter of venturi

TABLE OF CONTENTS

Page

LIST OF FIGURES

Page

LIST OF TABLES

Page

1. INTRODUCTION

Various industries today have an increasing interest in multiphase flow measurement. The deep sea oil and gas industry, for example, would benefit greatly from improved multiphase flow measurement technology, as they frequently encounter multiple fluids in a single well (e.g. oil, water, gas). Industry currently uses several different types of technology to measure these types of flow.

One method, using large separator equipment, is a costly venture, and is especially so when done on the deep sea floor. This method splits the different mixture phases into separate pipelines, where single phase flow measurement devices read the individual flow rates of each component before they are mixed again and continue on down the pipeline. Reducing the amount of equipment needed can provide enormous savings [1].

A method of multiphase flow measurement using much less equipment uses microwave or gamma radiation to measure the density of a fluid mixture. While this method does allow for an in-line type of device, managing nuclear sources requires navigating a multitude of rules and regulations that are unnecessary for other types of devices. This, along with the relatively high cost of these devices, leaves much incentive for an improved multiphase flow measurement system [1].

A method with potential cost savings involves measuring the percentage of one phase relative to the other using electrical impedance. If the two phases of a mixed fluid have different electrical characteristics, then a mixture of the two takes on a combination of those characteristics that varies with the mixture composition [2]. This electrical impedance technique, in combination with an obstruction-type flow meter to measure the total volumetric flow rate, allows one to calculate the individual flow rates of each component of a multiphase flow [3][4][5].

An electrical impedance-based multiphase flow meter using a slotted orifice plate as the obstruction-type flow meter has been shown to be effective at measuring the flow rate of mixed air-water flows on the 2” scale [3].

This thesis describes the design, construction, experimental testing, and subsequent analysis of the results of a low-cost electrical impedance-based multiphase flow meter (MPFM) for air and water mixtures in a NPS 6 inch pipe. The MPFM was tested at a much wider range of flow rates (305-820 gpm vs. 10-80 gpm in previous experiments) and pressures (50-350 psig vs. 20-80 psig in previous experiments) with a desire to prove its viability in more extreme conditions.

2. LITERATURE REVIEW

This section will discuss the relevant information surrounding the concepts used in this study's MPFM design. Particular attention is focused on the specific flow measurement devices used as well as the electrical impedance techniques.

2.1 Flow Regimes

In a two-phase flow, different flow rates and ratios of the mixture components can have very different flow patterns. These different manifestations of the flow, which are difficult to predict, are known as flow regimes. The difficulty lies in the fact that the flow regime depends on the individual flow rates of both components, the pressure, pipe geometry, and other operating conditions. Additionally, there is no clear transition from one regime to the next [6].

Mandhane proposed the flow regime map for horizontal pipe flows seen in Figure 1 [7]. This map takes into account varying pipe diameters by using superficial velocities of the gas and liquid components on the x- and y-axes. Superficial velocity is defined by Equation 1, V_s is the superficial velocity of a component, A is the flow area of the pipe, and Q is the volumetric flow of that component through the pipe. Figure 1 was constructed using air-water data, but Mandhane provides a correction factor for different fluid combinations. Coleman showed that while the Mandhane map works well, it does not hold for smaller tubes, as surface tension and other factors begin to affect the flow as well [8].

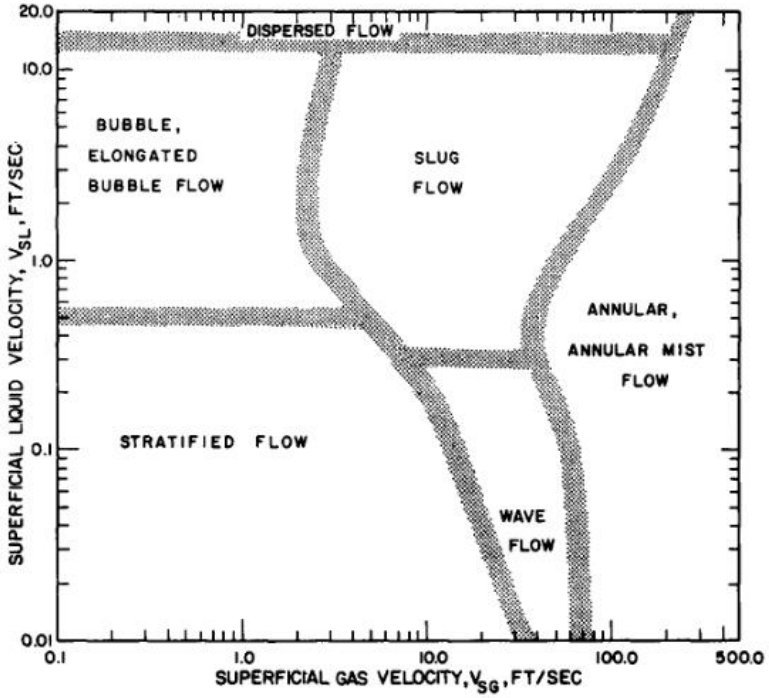

Figure 1. Flow regime map proposed by Mandhane [7]

$$V_S = \frac{Q}{A} \tag{1}$$

The various flow regimes are visually represented in Figure 2 [3]. In a stratified flow, the flow rates of both components are slow enough that gravitational forces can separate the two phases vertically in the pipe. As air flow rate increases from a stratified flow, the water layer becomes increasingly wavy until eventually, the water layer is pushed against the outer diameter of the pipe as air flows through the center. This is known as an annular flow. At higher water flow rates, with a lower air flow rate, the flow is mostly water with bubbles mixed throughout, known as bubbly flow. Increasing the air flow rate increased the bubble size and count until large coalesced bubbles or "plugs" begin to form. This is known as plug or elongated bubble flow. Increasing yet further causes these plugs to become so large that it is now intermittent "slugs" of

water that pass through the pipe in air, or slug flow. Even more air flow yields, again, an annular flow regime. [9]

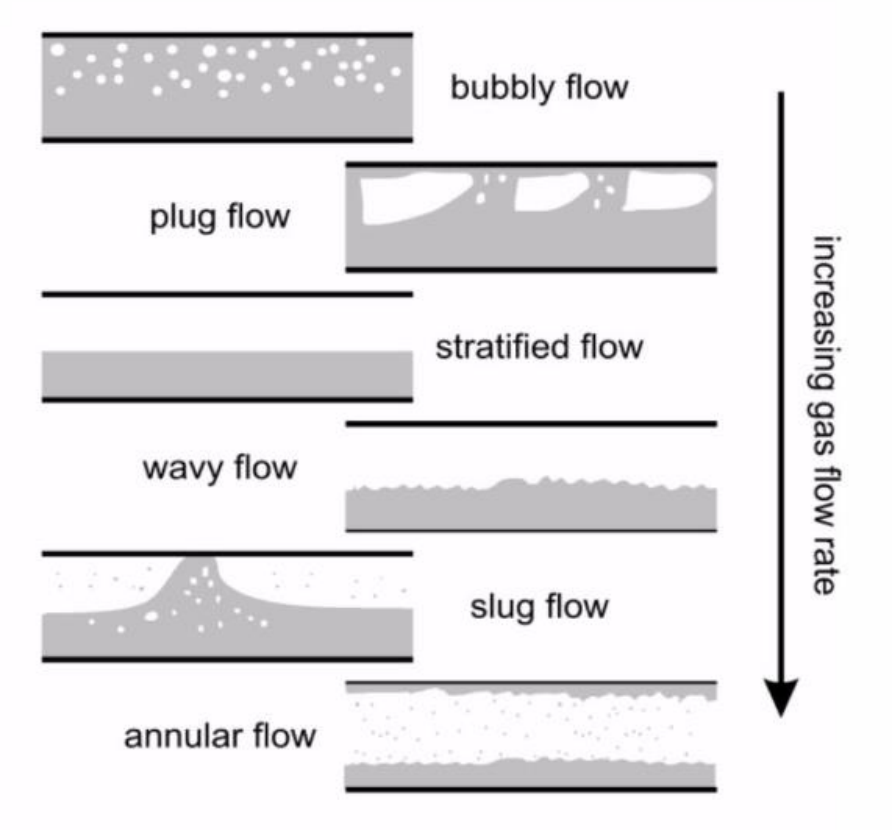

Figure 2. Visual representations of the flow regimes in a horizontal pipe [2]

2.2 Standard Orifice Plate

The orifice plate is commonly used in industry as a flow measurement device in pipes. It is simply a flat plate oriented perpendicularly to the flow with a circular hole cut in its center. The hole allows fluid to pass through, but creates losses that manifest as a differential pressure across the plate. This differential pressure is correlated with the flow rate through the pipe. By measuring it, one can estimate the flow rate within the pipe with ±1-4% accuracy [10][25].

This accuracy is affected by several factors: geometry of the plate (β, the square root of the ratio of hole area to pipe area), swirl in the flow, and upstream straight pipe distance being the most apparent [9]. The effects of these factors can be mitigated by following certain design criteria, many of which have been standardized in ISO 5167. For instance, according to ISO 5167, 6 pipe diameters upstream distance between a globe valve and a $\beta = 0.5$ orifice plate is necessary to achieve added uncertainty of less than 0.5%.

Its simplicity does not come without drawbacks, however. As an obstruction-based flow meter, there is a significant pressure drop across the device that in many applications is wasted useful energy. Additionally, its coefficient of discharge C_D (a constant calculated to calibrate the meter) changes significantly with flow rate and swirl in the flow [9][11].

2.3 Slotted Orifice Plate

The slotted orifice plate was developed to be a superior alternative to the standard orifice plate in 1993 [12]. It is similar to the standard orifice plate, except instead of the flow area consisting of a single circular hole in the center, the flow area is distributed across the pipe's diameter in a pattern of radially oriented slots.

Macek showed that the slotted plate performs better than the standard orifice plate by being less sensitive to upstream velocity profiles and swirl [12]. Morrison showed that the pressure recovery length is shorter, it creates less head loss, and less upstream straight pipe distance is required before the slotted plate for accurate operation [11].

In 2001, Morrison proved that the slotted plate behaves well even with two-phase flows, given that the density is well known [13]. Sparks showed that the slotted plate is able to homogenize an incoming two-phase flow regardless of the incoming flow regime [14]. The C_D of the slotted plate was shown to vary significantly only with density by Morrison in 2013 [4]. A study by

Annamalai calculated that the flow is most homogeneous approximately 1.5 pipe diameters downstream of the slotted plate [15].

2.4 Venturi Tube Flow Meter

A venturi tube flow meter is an inline flow measurement device that consists of a converging and then diverging section of pipe. Pressure taps are located before the converging section and in the "throat" between the converging and diverging sections. The pressure measurements from these taps can be used to estimate the fluid flow through the pipe given a calibration similar to that for an orifice plate. Uncertainty in flow measurements can be below 1% [10]. The diverging section is designed so that the fluid does not recirculate during pressure recovery [16]. Because the venturi does not lie perpendicular to the flow, and its diverging section gradually increases in diameter back to the original pipe diameter, the pressure loss through the venturi is significantly less than that of the standard or slotted orifice plate. This makes it a very popular choice when a higher component cost is justified [16].

It has been shown that a venturi meter can also be used to measure two-phase wet gas flows within the bubbly flow region using the traditional single-phase equations [17]. As the flow transitions from bubbly to slug flow, the equations began to deviate from experimental results, requiring additional correction factors.

2.5 Electrical Impedance

Electrical impedance is a property of a fluid that has been used in a multitude of different ways to measure multiphase flow. The electrical impedance of a fluid is generally modeled as both a resistor and a capacitor in parallel [2]. This property has been shown to correlate with the gas volume fraction of a liquid-gas flow, as the impedance of a multiphase fluid is generally some combination of the individual phases' impedances [18]. Being a complex property, it also varies

significantly with the excitation frequency used. Finally, the mixture flow regime (stratified, annular, bubbly, etc.) has been shown to influence the impedance [19].

Da Silva used an auto-balancing bridge to measure the impedance of a two-phase flow similar to that seen in Figure 3. This type of circuit is resistant to stray capacitance, and so analysis of the circuit is much simpler. Additionally, it typically has a high signal-to-noise ratio [2].

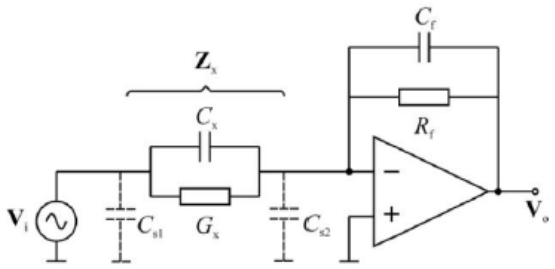

Figure 3. Auto-balancing bridge circuit (Sihombing [3])

Equation 2 is the governing equation of the circuit, where V_o is the output voltage of the op-amp, V_i is the excitation signal, R_x is the fluid mixture resistance, R_f is the bridge's resistance, C_x is the fluid mixture capacitance, C_f is the bridge's capacitance, and ω is the excitation signal frequency in rad/s. The magnitude of the gain given by Equation 2 is given by Equation 3 where f is the excitation frequency in Hz.

$$\frac{V_o}{V_i} = -\left(\frac{G_x + j\omega C_x}{G_f + j\omega C_f}\right) \tag{2}$$

$$Gain = \left|\frac{V_i}{V_o}\right| = \frac{\sqrt{G_x^2 + (2\pi f)^2 C_x^2}}{\sqrt{G_f^2 + (2\pi f)^2 C_f^2}} \tag{3}$$

By using the gains from two different frequencies, one has enough information to calculate both the resistive and capacitive part of the impedance. This then allows one to know the ratio of one fluid to the other.

Sihombing tested the effect of fluid mixture temperature on measured gain for an electrical impedance-based multiphase flow meter in a 2" pipeline. The two fluids used were air and water. His results showed that temperature indeed had a significant effect, as to be expected given that water's conductivity varies with temperature, and that this effect was roughly linear in nature. Thus, it was simple to model using linear regression techniques. These models were then used to correct the measured gain values such that the temperature effect was eliminated. It was also shown that at lower GVFs (below 40%), the temperature effect on gain varied little with increasing GVF [3].

3. OBJECTIVES

The following objectives were pursued in this experiment:

- Design and construct a low-cost electrical impedance-based MPFM for use in larger diameter (6”) pipes.
- Determine what variables affect the signal gain of the MPFM.
- Determine the ability of the MPFM to measure both the % GVF and total flow rate through a pipe.
- Determine whether the electrical impedance-based design can function accurately in a 6” pipeline.
- Determine whether the electrical impedance-based design can function at higher flow rates and pressures than previous experiments.
- Develop calibration equations to convert measured data into flow rate measurements for each component of a two-phase flow.

4. EXPERIMENTAL FACILITIES AND METHODS

This section will describe the design and construction of the MPFM as well as the test facility used to evaluate its performance.

4.1 MPFM Conceptual Design

Figure 4 and Figure 5 display SolidWorks renderings of the MPFM used in the study. It follows a wafer-style design, and is made to fit in line with NPS 6" schedule 40 piping. The MPFM is compressed between two 600# flanges with both ends sealed using spiral-wound gaskets. It consists of both an alumina-enclosed electrode assembly and a slotted orifice plate meter, both contained in a stainless steel housing.

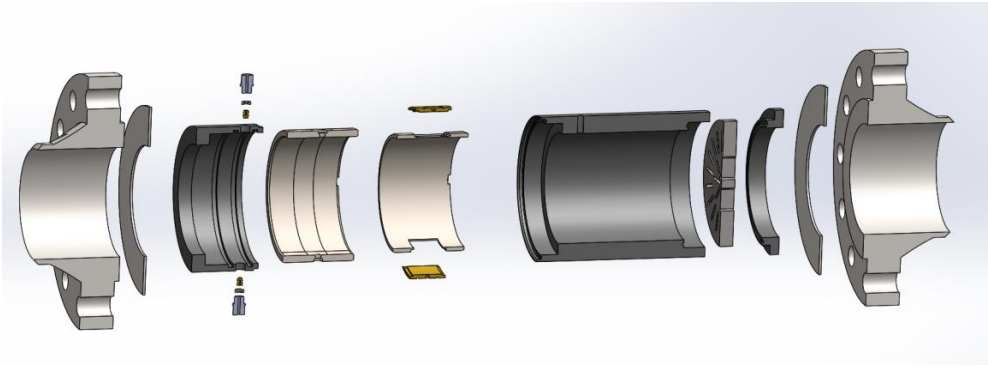

Figure 4. Exploded view of MPFM assembly

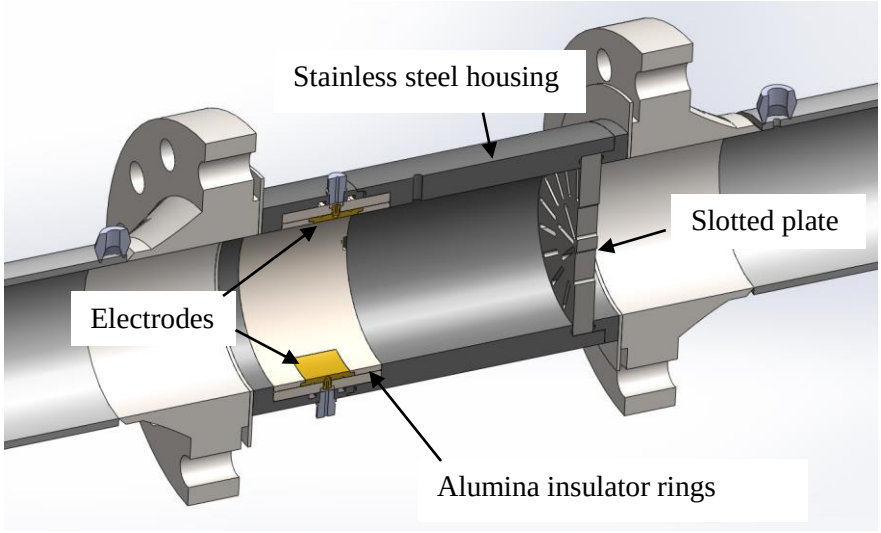

Figure 5. Design of MPFM

Previous electrical impedance-based MPFM designs for smaller pipes (such as those used by Sihombing) also used the slotted plate and diametrically opposed electrodes. However, their piping was primarily non-conductive PVC piping, and relatively low pressure. For the 6" MPFM in this thesis, stainless steel design was necessary to handle the high pressures, and so the electrodes could not be threaded or glued directly into the pipe wall due to electrical isolation issues.

The brass (Alloy 360) electrodes from which the electrical signal is passed through the fluid are designed to be flush with the pipe inner diameter in order to reduce pressure drop through the device. The electrodes are electrically isolated from the 304 stainless steel housing by means of concentric alumina ceramic rings. The curved electrode piece fits through a slot in the inner alumina ring so that the inner and outer diameter of its curvature matches that of the alumina, as seen in Figure 6. An o-ring on the outer surface of the electrode (Figure 6) forms a seal between the electrodes and the outer alumina ring. The outer alumina piece slides over the inner piece

after the o-rings are in place, completing the electrode assembly. The outer alumina piece has holes through which electrical wire can pass to be bonded to the electrode.

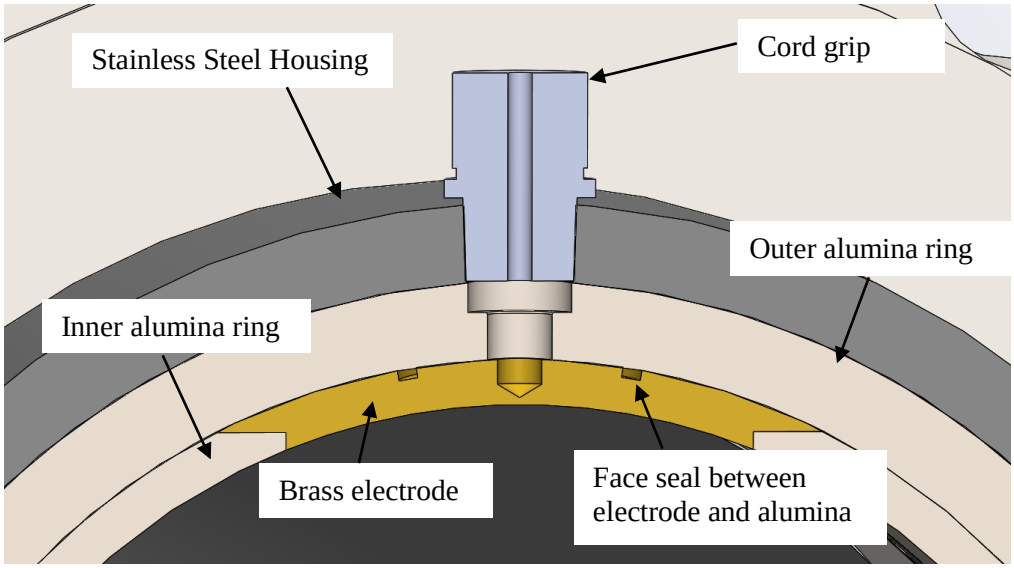

Figure 6. Axial cross-sectional view of MPFM for electrode sealing and wiring detail

The housing is made of three interlocking stainless steel pieces. Between these fit both the slotted orifice plate and the electrode assembly alumina ring. An o-ring face seal is used to seal between the two pieces that surround the electrode assembly, as seen in Figure 7. O-ring grooves are also present in order to form face seals on both sides of the slotted plate, as seen in Figure 8. Between the stainless steel shell and the electrode assembly, o-ring gland seals were used to prevent leakage through the electrode wiring holes, as seen in Figure 7.

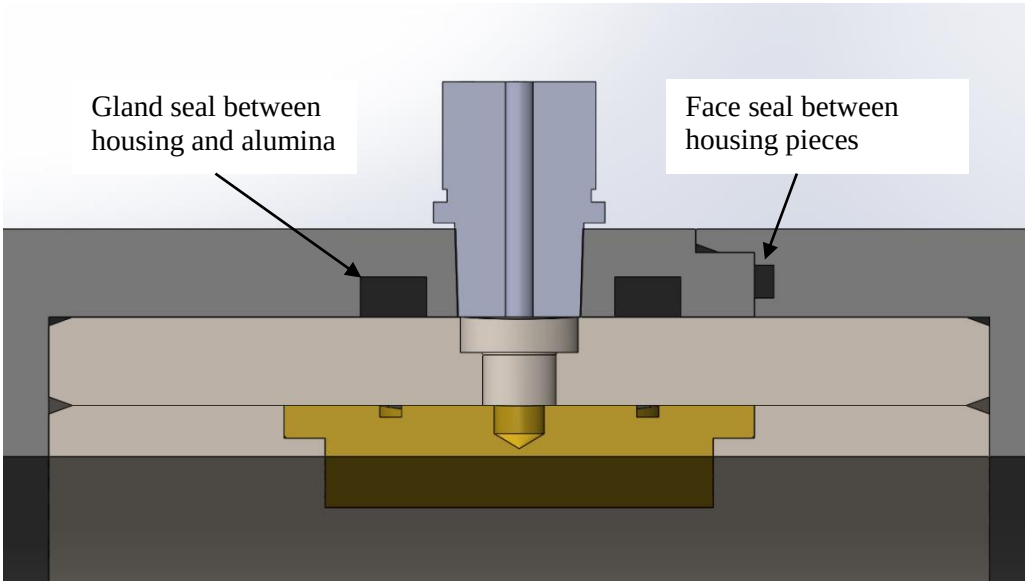

Figure 7. Radial cross-sectional view of MPFM to show housing o-ring details

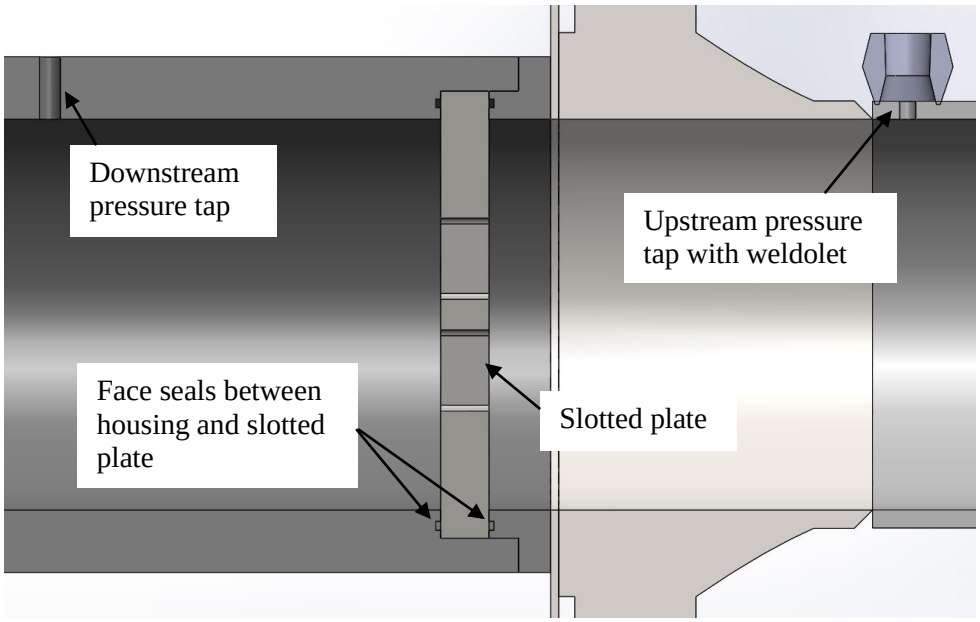

Figure 8. Radial cross sectional view to show slotted plate sealing detail and pressure taps

The electrodes are located approximately 1.5 diameters downstream of the slotted plate (9 inches). This ensures the most homogeneous flow at the electrodes, according to Annamalai

[15]. The electrical wiring is bonded to the electrodes using a high conductivity silver epoxy and held in place using cable grips threaded into the housing.

The slotted plate was designed with a beta ratio β of 0.496. This ratio is very close to the ideal two phase performance ratio for a slotted plate of approximately 0.5 [13]. The slot sizes and arrangement relative to the overall pipe diameter are identical to those used by Sihombing with 2" pipe, and so it is a direct scale-up of these 2" slotted plates [3]. This simplifies comparison of the performance. The number of concentric rings of slots and number of slots per ring was selected by previous researchers for its ability to produce a roughly parabolic velocity profile coming out of the plate, improving the distance needed for a fully developed profile [22].It was manufactured using electric discharge manufacturing.

A pressure tap is located in the housing after the slotted plate to allow the measurement of the pressure at that location, while the upstream pressure tap is actually located in the upstream piping as seen in Figure 8. The upstream tap is used to measure the absolute pressure, the upstream temperature, and the high pressure end of a differential pressure measurement.

4.2 Measurement and Data Acquisition

An Omega PX429-500GI pressure transducer was used to measure the absolute pressure in the MPFM upstream pressure tap. This transducer has an operating range of 0-500 psig and an accuracy of ±0.4 psig. An Omega TQSS-18U-6 T-type thermocouple was used in the upstream tap to measure temperature. It has a measurement accuracy of ±0.6 °F, and can withstand temperatures up to 220 °C. A Rosemount 3051CD3A22A1A differential pressure transducer was used to measure the pressure difference across the slotted plate, with the high pressure line using the upstream tap, and the low pressure line using the downstream tap. It has an operating range of 36 psig, with ±0.05 psig accuracy, and generates a 4-20 mA signal.

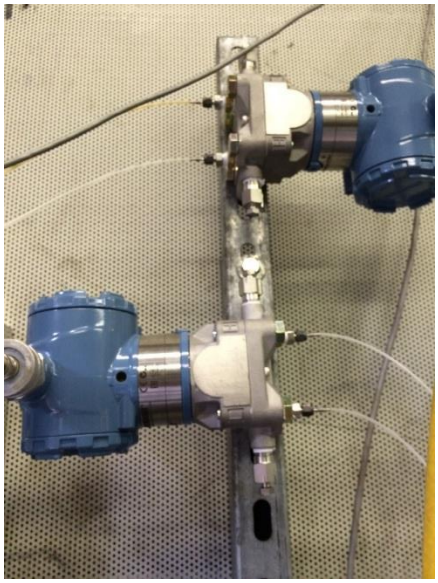

Figure 9. Rosemount pressure transducers used to measure slotted plate and venturi differential pressures

Figure 10. Omega pressure transducer

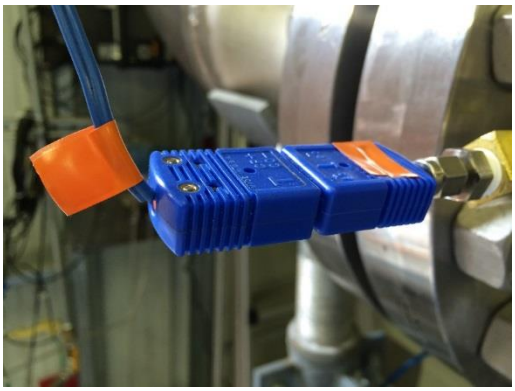

Figure 11. Omega thermocouple

GVF was measured using the electrical impedance method proven by Pirouzpanah (2014) and Sihombing (2015) [20][3]. A Picoscope 5442B oscilloscope/function generator device was used to generate the various frequencies to be passed through the fluid as well as measure the signal conditioner output. Its arbitrary waveform generator (AWG) can generate signals at 200 MS/s and it has a 500 MS/s sampling rate with 12-bit resolution. Using two channels in this experiment divided the sampling rate so that it has a maximum of 250 MS/s per channel. The twelve frequencies used in the experiment were: 200 kHz, 600 kHz, 1 MHz, 1.28 MHz, 2.37 MHz, 3.46 MHz, 4.55 MHz, 5.64 MHz, 6.73 MHz, 7.82 MHz, 8.91 MHz, and 10 MHz. These twelve frequencies were added together to produce one combined signal that was uploaded to the Picoscope as the AWG's reference waveform. The combined signal output was passed through the fluid mixture and signal conditioning circuit. Both the direct output from the Picoscope and the output from the fluid mixture and signal conditioner circuit were monitored using the Picoscope's input channels, as seen in Figure 12.

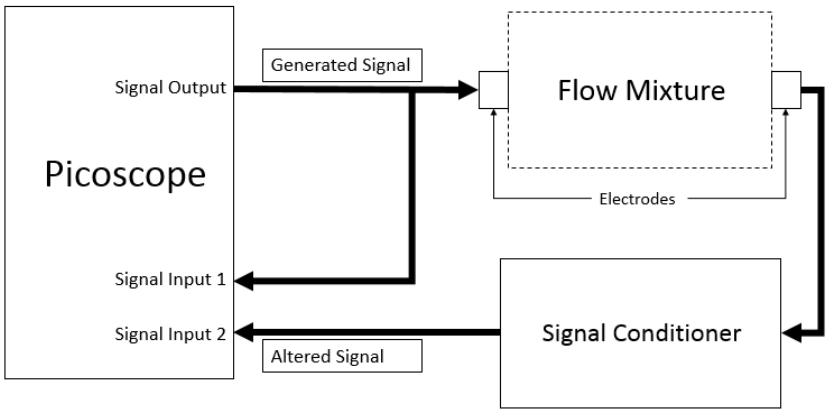

Figure 12. Signal generation and capture schematic.

LabVIEW programs were used in the control room to operate the test rig remotely. Figure 13 shows the program used to monitor the pump's performance and the various pressures, temperatures, and flow rates throughout the test loop. It also used PID control algorithms to operate the loop's control valves in order to maintain the user's desired pump inlet pressure, water flow rate, and GVF of the fluid mixture. Pressure transducer signals were read using NI 9205 voltage measurement modules in an NI cRIO-9074 chassis. Thermocouples were connected to an NI 9213 thermocouple measurement module in the same chassis.

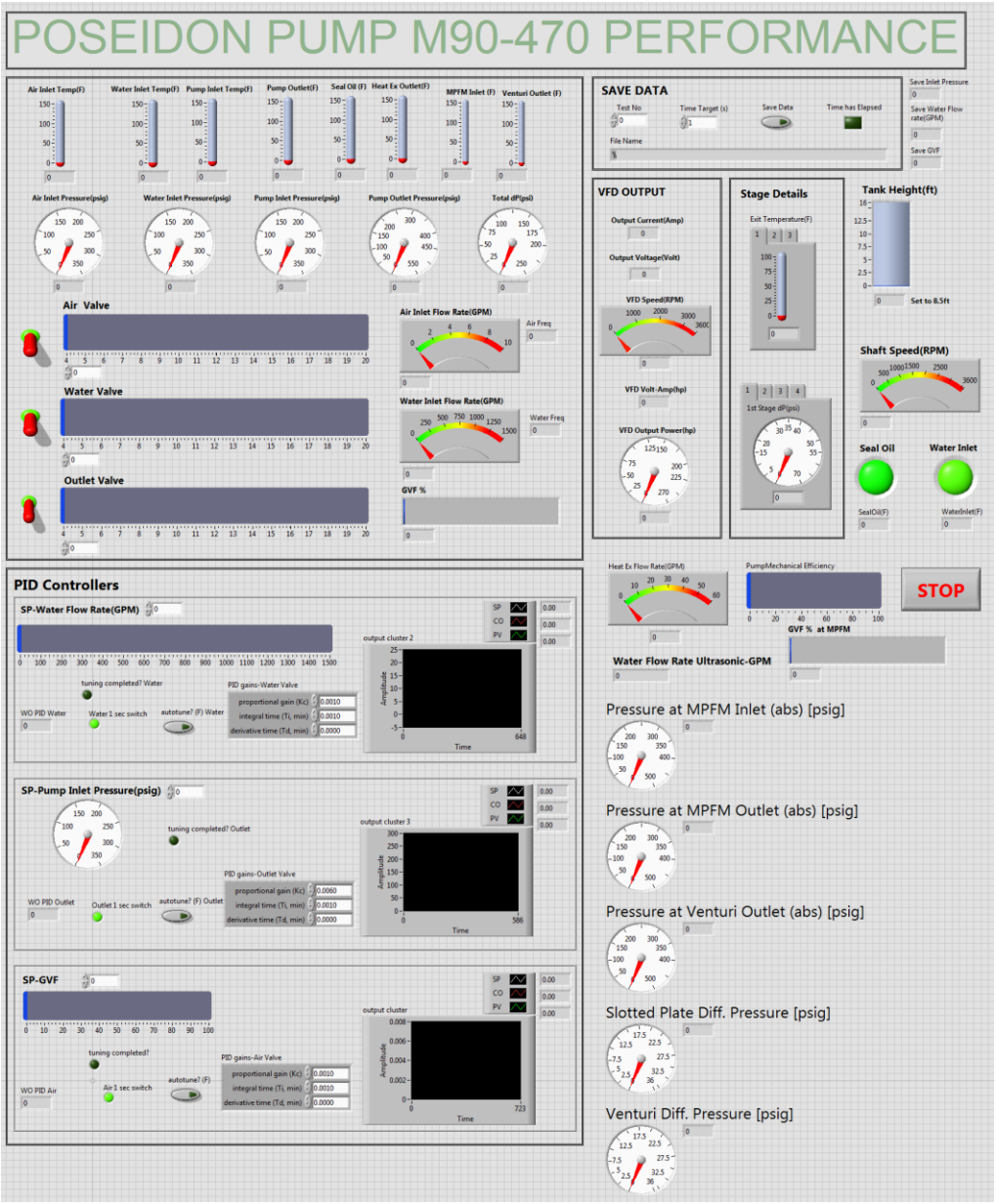

Figure 13. Pump control and fluid flow monitoring program

Figure 14 shows the program used to monitor the pump's vibration performance. In this experiment, this was used solely to ensure that the pump shaft's orbit did not indicate any impending mechanical failure.

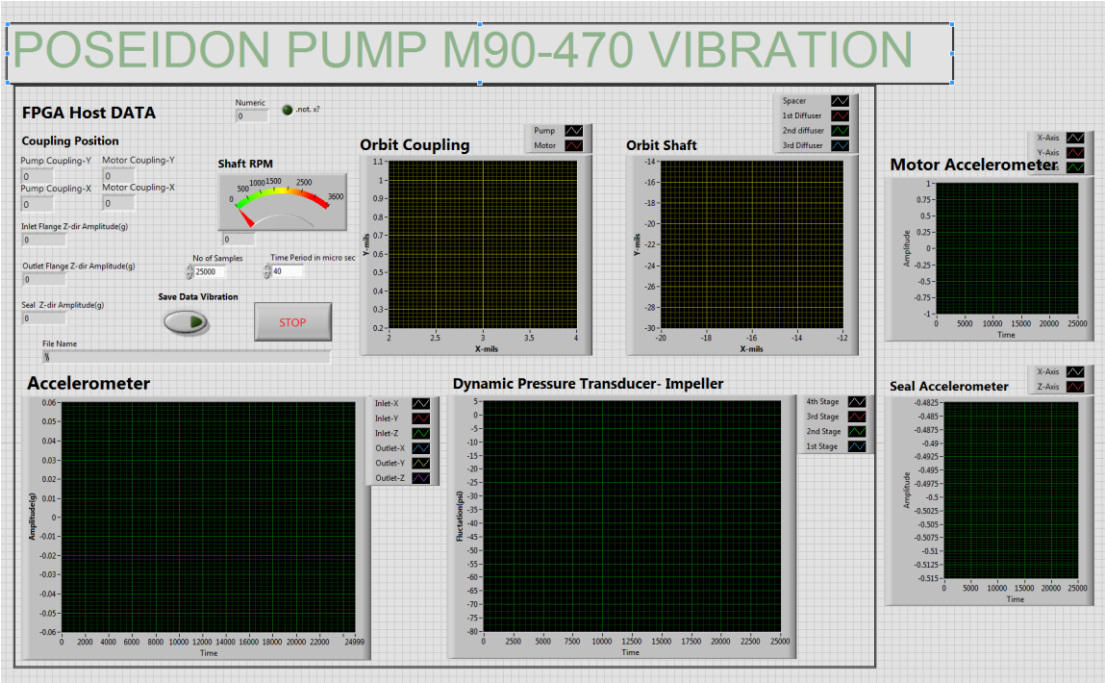

Figure 14. Pump vibration monitoring program

Figure 15 shows the program used to control the Picoscope and collect the MPFM signal data. It is set up to be able to operate all input channels at one time, but only two channels were activated during the experiment. The user pushes the "Take Data" button to copy the Picoscope's current memory buffer to the computer for further data processing. The program automatically names the collected data files using the current flow conditions in the loop.

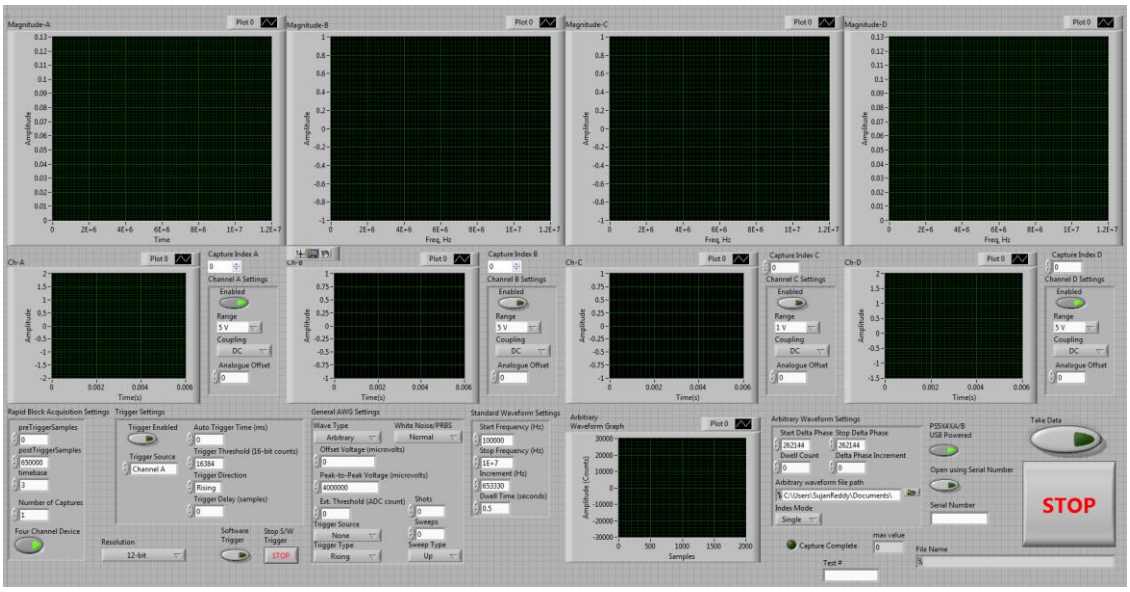

Figure 15. Picoscope control and MPFM data capture program

Figure 16 shows the circuit to be used to determine the frequency response of the test flows. The flow itself is modeled as a resistor and capacitor in parallel. The signal conditioning part of the circuit is an analog low-pass filter amplifier with a cut-off frequency of 15.9 MHz to filter out unwanted noise above the max generated signal frequency of 10 MHz. The op amp used in the circuit was a Texas Instruments LM7171 op amp with max current output of 100 mA and a supply voltage requirement of ±15V.

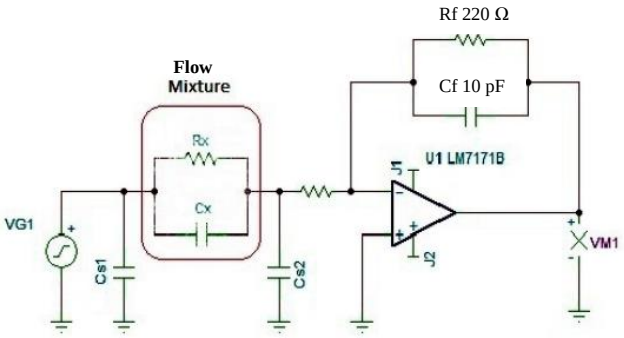

Figure 16. Circuit diagram for MPFM

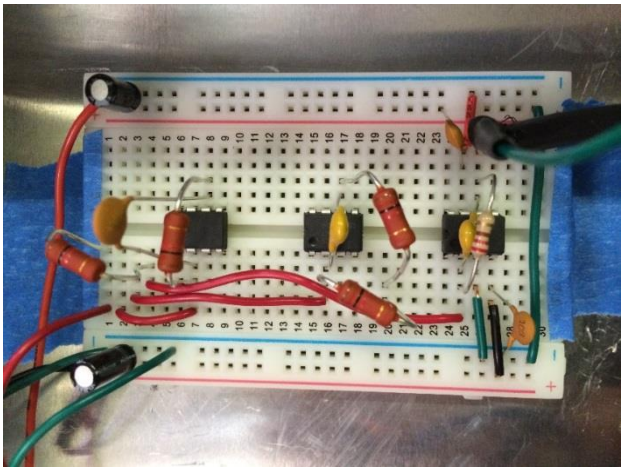

Figure 17. Filter circuit with 3 different amplifier circuits

Ordinarily, the Picoscope interfaces with a computer using USB. However, because the Picoscope was located inside the test cell (in order to reduce signal noise due to wire length), a USB-to-ethernet adapter was used to reach the computer in the control room. The equipment used was an IOGear GUWIP204 as seen in Figure 18. This device acts as a router that the computer can access to communicate across its multiple USB ports.

Figure 18. Inside of MPFM circuitry box with filter circuit, USB-to-ethernet converter/extender, and Picoscope signal generator/digital oscilloscope

4.3 Closed-loop Test Facility

Figure 19 is a process and instrumentation diagram of the flow loop used during testing, while Figure 20 is a SolidWorks rendering of the loop. It has three main fluid flow paths driven by a single pump: a water inlet line, an air inlet line, and a mixed outlet line. It is a closed loop system, with water and air lines converging at the pump inlet to create the air/water mixture that flows through the pump and then through the outlet line to a large stainless steel tank. The stainless steel tank acts as both a reservoir and a separator for the air and water. It can handle pressures up to 450 psi and has a total volume of 1760 gallons. Water is pulled from the bottom of the tank through the water inlet line, while air is pulled from the top of the tank through the air inlet line. The test loop is pressurized by injecting compressed air into the top of the tank until it reaches the desired pressure.

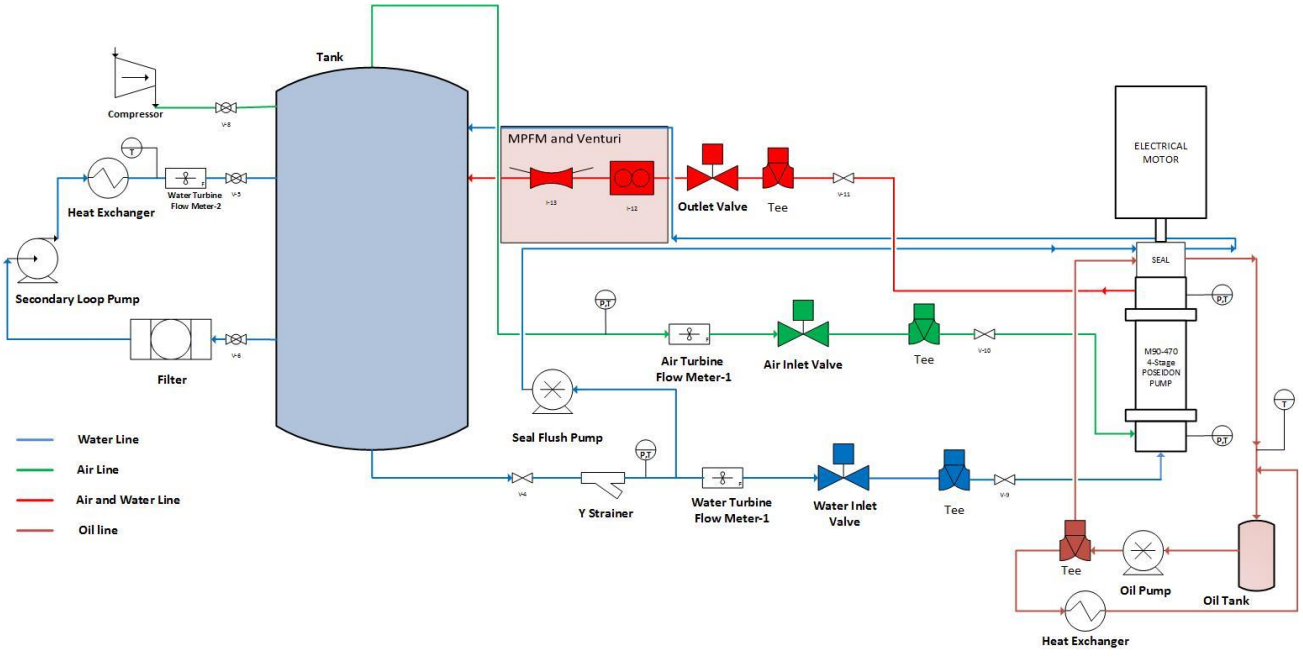

Figure 19. Process and instrumentation diagram of flow loop.

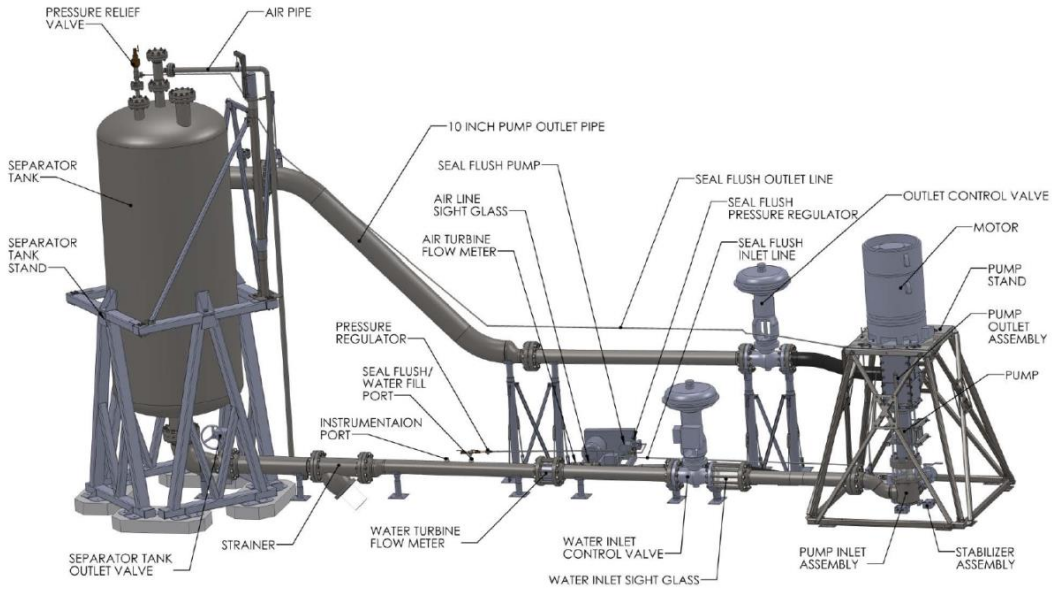

Figure 20. SolidWorks rendering of closed loop test facility (Kirkland [21])

Control valves (Figure 21) are located on the air and water inlet lines as well as at the pump outlet to control the water, air, and overall flow rates through the pump. They are operated remotely using a LabVIEW program, and follow a PID control algorithm. Turbine flow meters are also located on the air and water lines to measure the flow rates of each component (Figure 22). The water turbine meter is a Turbines, Inc. WM0600X6, and has an accuracy of ±1% over the range 250-2500 gpm. The air turbine meter is an Omega FTB-938 with an accuracy of ±1% and a range of 60-970 gpm. The flow rates obtained are used to calculate the GVF of the fluid flow.

Figure 21. Control valve on outlet line

Figure 22. Turbine meter used to measure water flow in the inlet line

It is important to ensure that air is not in the water line, nor water in the air line. Either case will negatively impact the flow rate measurements, and could even damage the turbine meters. In order to monitor the air and water inlet lines for this kind of contamination, visualization windows are installed inline, as seen in Figure 23 and Figure 24. The air window is made of glass, and can handle pressures up to 720 psig and temperatures up to 250 ºF. These constraints are far less restrictive than other system components. The water window, however, is made of

acrylic, and so the maximum water inlet temperature allowed for operation is 110 ºF. The window can handle pressures beyond the maximum operating pressure of the large stainless steel tank. A closed-circuit television system is used to view the windows remotely from the control room.

Figure 23. Visualization window for air line

Figure 24. Acrylic visualization window for water line with CCTV camera visible

The pump installed in the loop is a 4-stage helicoaxial pump manufactured by Schlumberger. It is made to handle higher GVF flows than other types of pumps due to its intended use as an

electrical submersible pump in deep-sea oil extraction. It is driven by a 250 HP electric motor controlled using a variable frequency drive (VFD) at speeds of up to 3600 rpm. The pump is mounted under a test stand made to withstand both the thrust generated by the pump and the weight of the electric motor that is mounted above. This setup can be seen in Figure 25.

Figure 25. Inside of closed loop test facility. Pump is beneath motor stand (right). Control valves and inlet/exit piping are at left.

The top bearing of the pump is cooled using an auxiliary oil loop, seen in Figure 26, that uses a heat exchanger to cool the oil. Room temperature water is used as the other process fluid in the

heat exchanger. The bottom bearing is located at the pump inlet, and so is cooled by the incoming air and water.

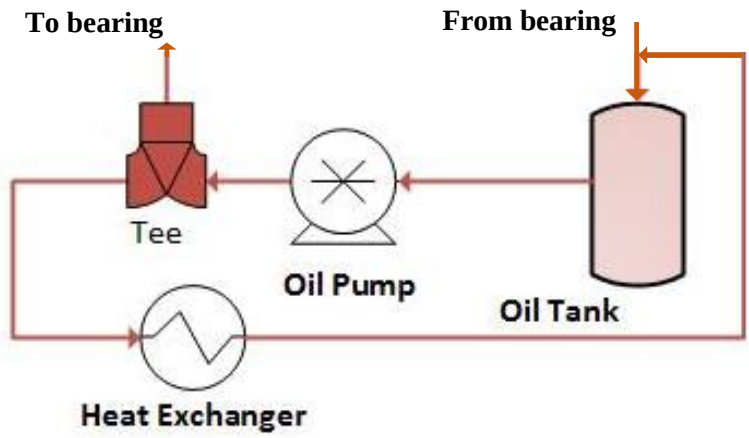

Figure 26. Bearing oil heat exchanger loop

A mechanical seal at the very top of the pump requires a constant flow of water to operate correctly. Thus, a seal flush pump is used to pump water from the bottom of the outside large tank through the seal and back into the tank. Figure 27 shows the seal flush pump skid.

Figure 27. Seal flush pump skid (disconnected during disassembly)

In order to prevent overheating of the air and water in the large tank, an additional heat exchanger loop takes water out of the bottom of the tank and runs it through a filter and large heat exchanger, seen in Figure 28. Temperature in the water inlet line must be kept below 110 ºF because of the clear acrylic pipe section. Figure 29 is a schematic of the heat exchanger loop.

Figure 28. Heat exchanger fan and pump (left) and large stainless steel tank for water/air reservoir (right).

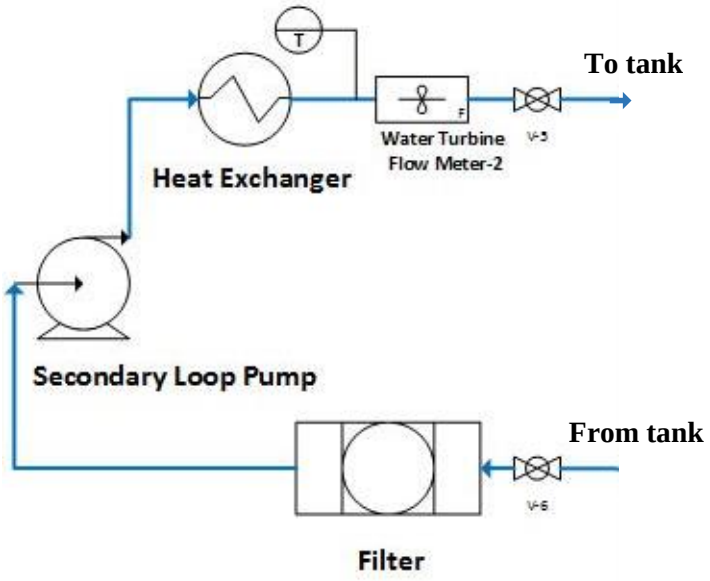

Figure 29. Heat exchanger loop

The MPFM assembly was placed after the outlet valve of the test loop's main pump. The piping was designed so that the entire MPFM would be at least 5 diameters downstream of the outlet valve to minimize flow effects associated with the valve.

A venturi flow tube was placed just downstream of the MPFM to provide additional flow rate measurement validation. It was manufactured within a pipe spool so that it could be easily swapped for a section of plain pipe if desired. Figure 30 shows this design concept. It has a beta ratio of 0.5, and three pressure taps: one at the inlet before the contraction, one in the contracted portion, and one at the outlet following the expansion. A Rosemount 3051CD3A22A1A differential pressure transducer identical to that used with the slotted plate was used to measure the differential pressure between the venturi inlet and its contracted portion. Omega PX429-500GI pressure transducers were also used to measure gage pressure at the venturi inlet and outlet pressure taps. Another Omega TQSS-18U-6 T-type thermocouple was installed at the

venturi outlet pressure tap. Given that venturi tubes have very high pressure recovery (and, thus, low losses) this outlet temperature reading should be the same as the temperature between the electrodes and was used as such.

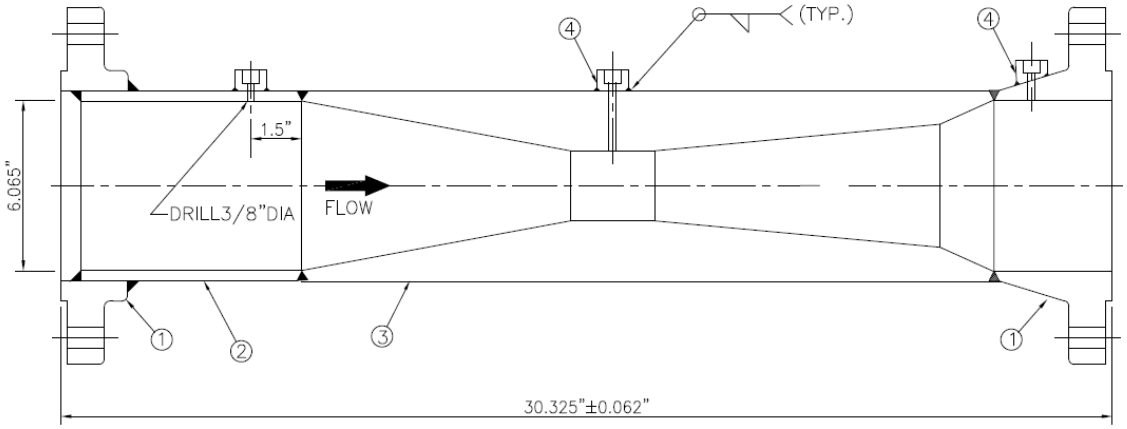

Figure 30. Drawing of venturi built inside pipe spool

4.4 Assembly

Figures 31-36 help illustrate the assembly and installation of the MPFM as manufactured. Figure 31 shows the brass electrodes with their o-rings in-groove. These were inserted into their mating slots in the inner alumina ring, which was then inserted into the outer alumina ring as shown by Figure 32. O-rings were placed in their grooves in the stainless steel shell pieces.

Figure 31. Brass electrodes with o-rings

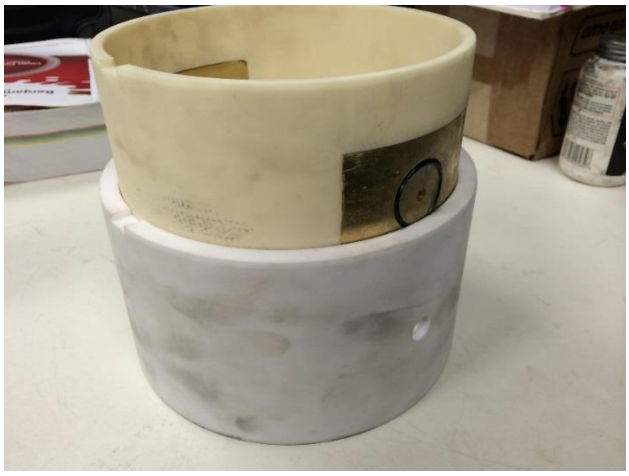

Figure 32. Insertion of inner alumina ring into outer with electrodes in place

The alumina assembly was then inserted into one half of the stainless steel shell as in Figure 33. This assembly was then inserted face-down into the second half of the stainless steel shell.

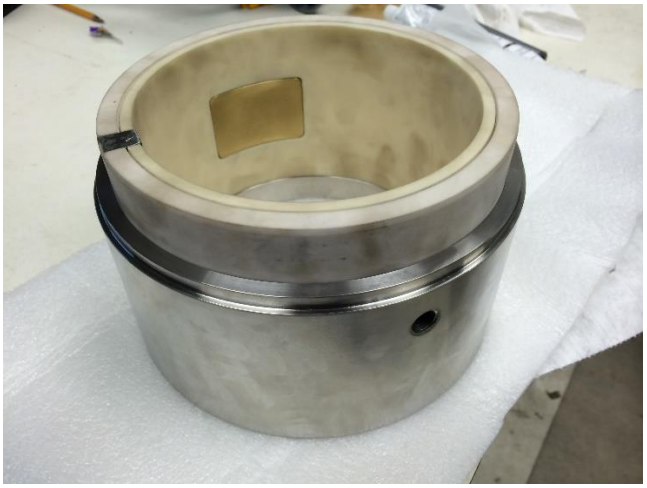

Figure 33. Alumina inserted into outer shell.

The slotted plate was placed between the final two shell pieces—completing the wafer assembly. Figure 34 illustrates the slotted plate's geometry.

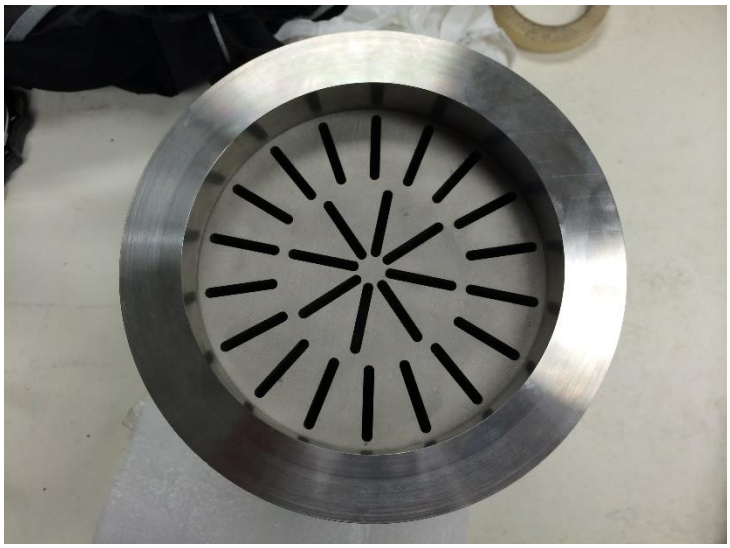

Figure 34. Slotted plate in assembled MPFM shell

Electrical wire was attached with high-conductivity silver epoxy to the electrodes and supported by cord grips to prevent breaking. The completed MPFM wafer was then inserted between two

6” 600 lb flanges and tightened to the corresponding torque. Figure 35 shows the MPFM being fitted between the two flanges—one of which belonged to the venturi tube. Figure 36 shows the assembly in place in the closed loop facility with all electrical connections, thermocouples, and pressure transducers installed.

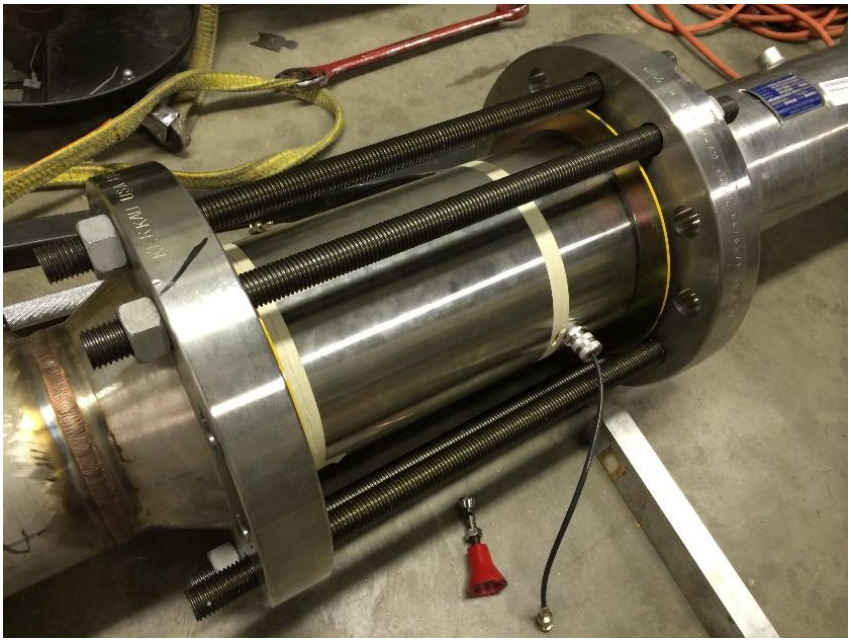

Figure 35. MPFM being installed between two pipe flanges. Electrical connections installed on sides.

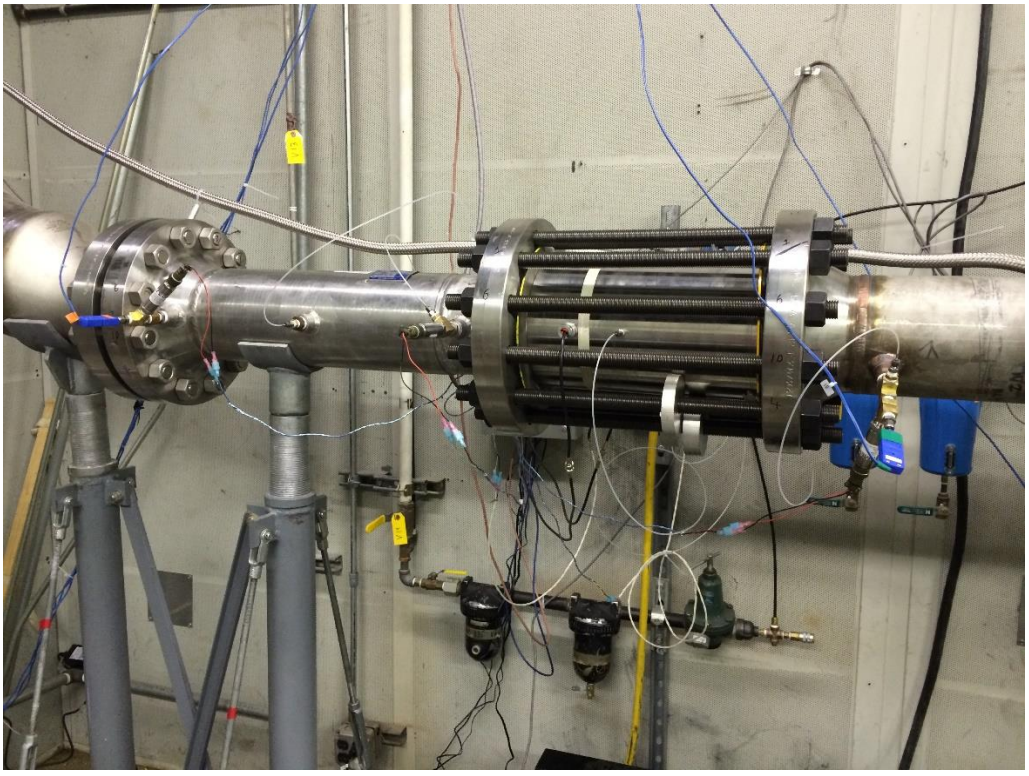

Figure 36. Finished assembly with all thermocouples, pressure transducers, and electrical connections intact.

4.5 Testing Plan

Once everything was installed, the pump was operated at various flow rates, pressures, and GVF's. Both the generated signal and the MPFM output signal were recorded for each flow condition in order to determine the MPFM's response to these varying conditions. The test matrix tested (as achievable by the pump) was:

- Pressure: 40, 100, 185, and 280 psi
- GVF: 0, 10, 20, 30, 40%
- Flow rate: 305, 395, 485, 570, 654, 737, 820 gpm

Each test session consisted of pressurizing the loop to the desired pressure and operating at that pressure for each combination of GVF and flow rate. Typically, only one pressure could be tested per day.

Temperatures were recorded for each condition to be used to treat the gain according to the technique developed by Sihombing [3]. In order to collect gain versus temperature data for the temperature correction method, separate tests were run for each GVF where flow rate, pressure, and GVF were held constant as the fluid temperature increased from room temperature to approximately 100 °F.

Slotted plate and venturi differential pressures were recorded for all conditions tested in order to calibrate their respective devices.

5. RESULTS AND DISCUSSION

This section will discuss the test results as well as develop calibration equations for the MPFM.

5.1 Flow Conditions Tested

At higher flow rates, it was not possible to achieve the higher GVF flows due to limitations of the pump. Additionally, it was proven difficult to achieve the lowest GVF flows for the lowest flow rates tested. Table 1 illustrates the flow conditions that were possible during testing. These limitations were consistent for each pressure tested, except for the 40 psi data, where 10% GVF and 395 gpm were also not possible.

Table 1. Flow conditions possible during testing

	Flow Rates (gpm)						
% GVF	*305*	*395*	*485*	*570*	*654*	*737*	*820*
0							
10	X						
20							
30							X
40						X	X

Not possible X Possible

5.2 GVF Measurements

The signal gain was calculated for each flow condition and frequency by dividing the signal amplitude coming from the MPFM electrodes by the signal amplitude generated by the Picoscope, as seen in Equation 4.

$$Gain = \frac{MPFM\ Amplitude}{Generated\ Amplitude} \tag{4}$$

Plotting the signal gains versus frequency for each GVF shows that, for most frequencies, increasing GVF tends to decrease the gain, as seen in Figure 37. Because of its large difference in gain between 0 and 40% GVF, 7.82 MHz was chosen as the primary frequency to be used for

subsequent analysis. This large gain difference at 7.82 MHz was consistent for all pressures and flow rates tested.

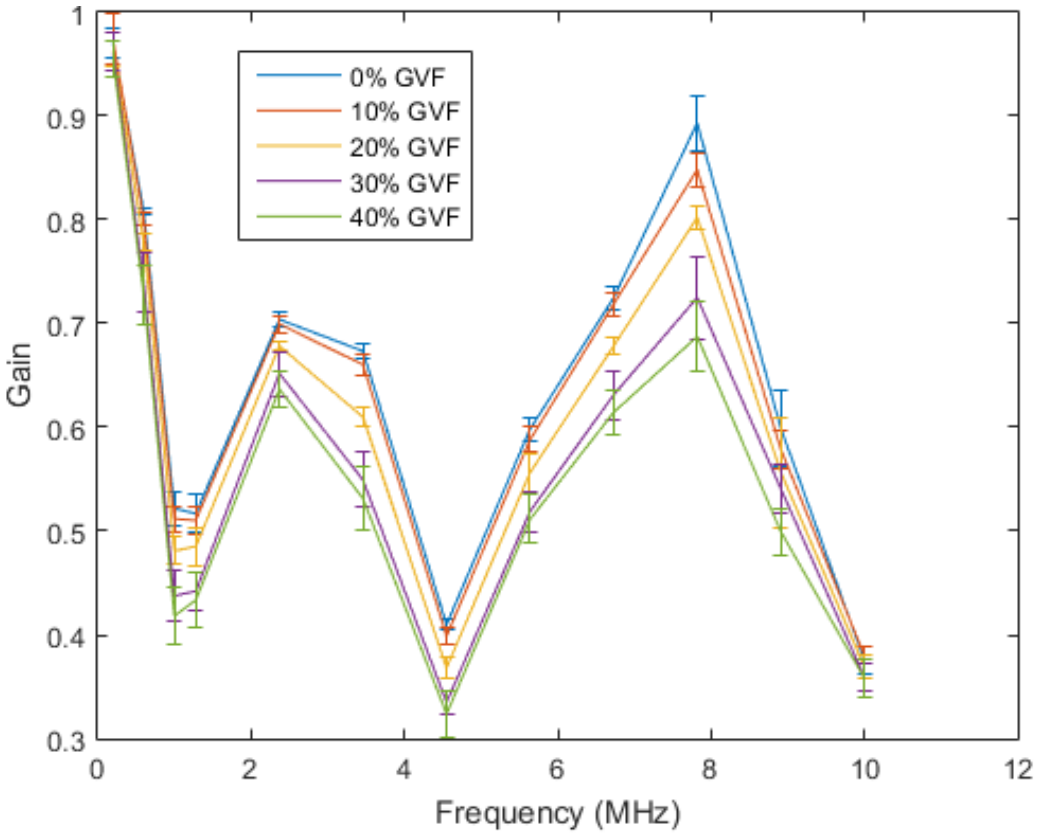

Figure 37. Gain vs. frequency (185 psi, 570 gpm) with 95% error bars shown

Because previous studies have shown a significant temperature effect on the gain, it was necessary to correct each gain based on its corresponding temperature [3]. This was accomplished, first, by plotting the gain versus temperature for each frequency while GVF,

pressure, and flow rate remained constant. A 2nd order polynomial regression was applied to the data as seen in Figure 38.

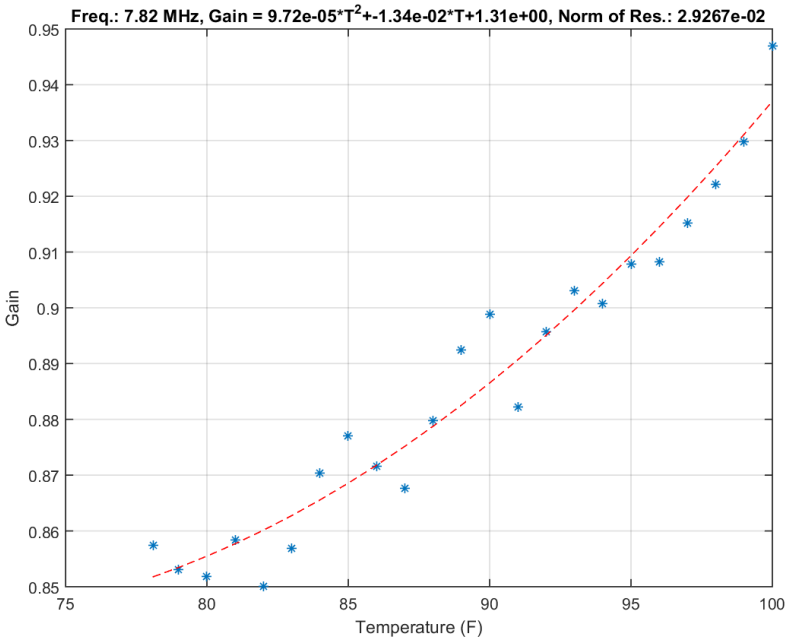

Figure 38. Gain vs. temperature (7.82 MHz, 0% GVF, 50 psig, 537 gpm)

Using the regression equation, it was possible to calculate the correction factor to be subtracted from each gain so that each gain has effectively the same temperature. Equations 5-8 detail this process, where $Gain_{ref}$ and T_{ref} are a reference gain and temperature relative to which the correction factor $\Delta Gain$ is calculated. The constants a, b, and c are the polynomial coefficients of the regression equation, and c_0 is a constant made to simplify the final gain correction factor equation.

$$Correction\ Factor = Gain - Gain_{ref} = \Delta Gain \tag{5}$$

$$\Delta Gain = (aT^2 + bT + c) - \left(aT_{ref}^2 + bT_{ref} + c\right) \tag{6}$$

$$\Delta Gain = aT^2 + bT + c_0, \quad \text{where } c_0 = -\left(aT_{ref}^2 + bT_{ref}\right) \tag{7}$$

$$Corrected\ Gain = Gain - \Delta Gain \tag{8}$$

The temperature effect's slope did not appear to vary much with GVF, pressure, or flow rate, as seen in Figure 39. The only exception appears in the 30% data, which shows a decreased slope. Because the goal of the experiment is to estimate the GVF of the fluid mixture, however, the GVF cannot be used during the temperature correction or else the conclusions would fall prey to circular reasoning. Additionally, the results of the work done by Sihombing (2015) showed that at low GVFs, the temperature effect did not vary much with changing GVF. Therefore, a single regression equation per frequency was used to correct the gain data.

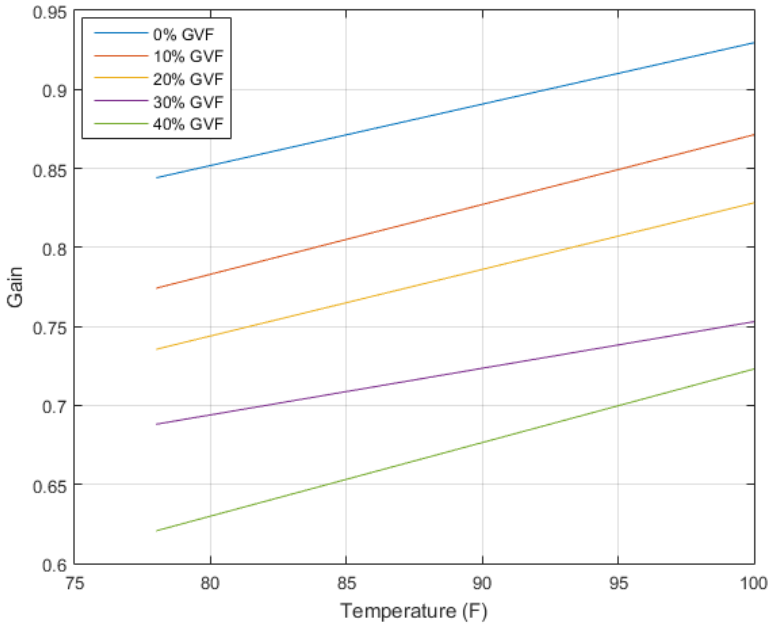

Figure 39. Gain vs. temperature for different GVFs

Table 2 displays the calculated correction factor equations for each frequency.

Table 2. Regression equations for temperature correction

Frequency **Gain Correction Coefficients**

$$(\Delta Gain = aT^2 + bT + c_0)$$

	a	b	c
0.2 MHz	-6.78E-06	0.001415	-0.06914
0.6 MHz	-2.23E-05	0.005708	-0.30951
1.0 MHz	-3.87E-05	0.00956	-0.51043
1.28 MHz	-6.06E-05	0.012605	-0.61428
2.37 MHz	-2.29E-05	0.005589	-0.29647
3.46 MHz	-1.72E-05	0.006538	-0.40559
4.55 MHz	-1.69E-06	0.00207	-0.15117
5.64 MHz	7.42E-06	1.84E-05	-0.04659
6.73 MHz	3.47E-05	-0.00394	0.096318
7.82 MHz	9.72E-05	-0.01343	0.455644
8.91 MHz	6.87E-05	-0.01177	0.499897
10.0 MHz	-2.65E-05	0.004535	-0.19256

The gain for each GVF was plotted versus its corresponding fluid static pressure in order to visualize how pressure affected the gain. This was done for each flow rate tested. As can be seen

in Figure 40, there was no clear visual trend with pressure within the uncertainties of the data. This was true for each flow rate tested.

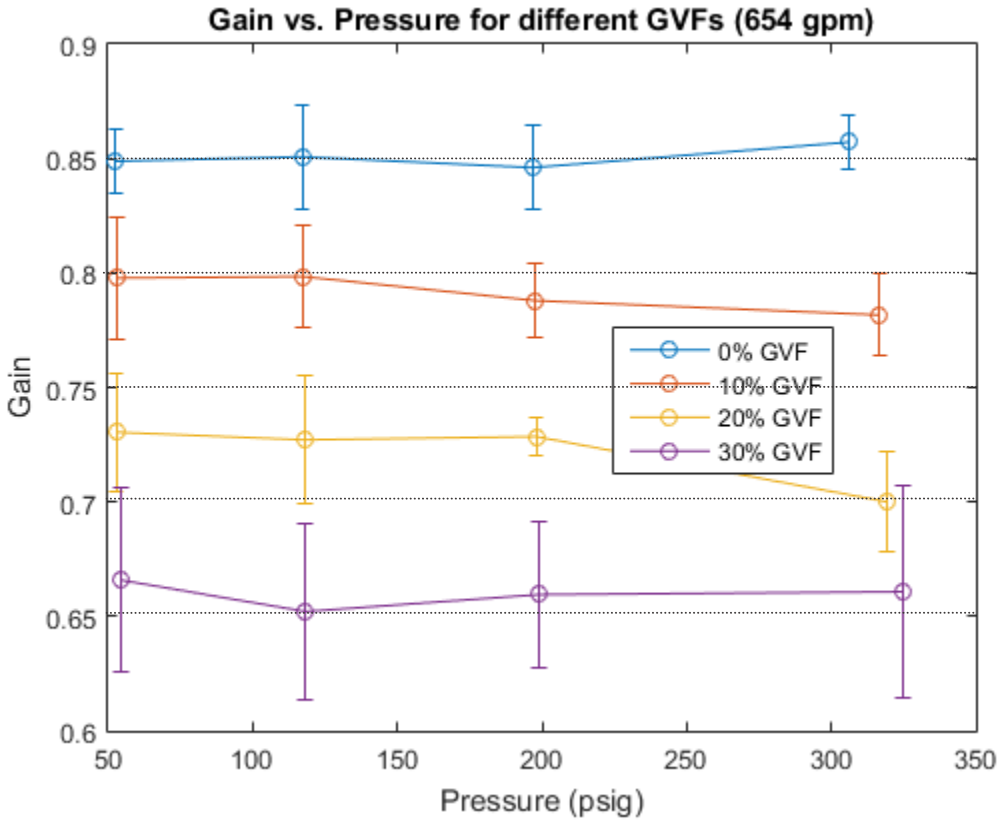

Figure 40. Gain vs. pressure for different GVFs (654 gpm)

The effect of water flow rate on gain was also investigated. Figure 41 shows gain plotted versus flow rate for different GVFs at 120 psig. It appears that water flow rate does have an effect on the gain: it decreases as the flow rate increases. However, this effect is only visible with air in the fluid, and appears to grow stronger with higher GVF. The fact that the water flow rate effect is not consistent across all GVFs and, in fact, appears to be dependent on GVF means that a simple correction like that used to correct for temperature is not possible. This flow rate effect

was not seen in the study conducted by Sihombing, and is thus likely to be a result of up-scaling the design. [3]

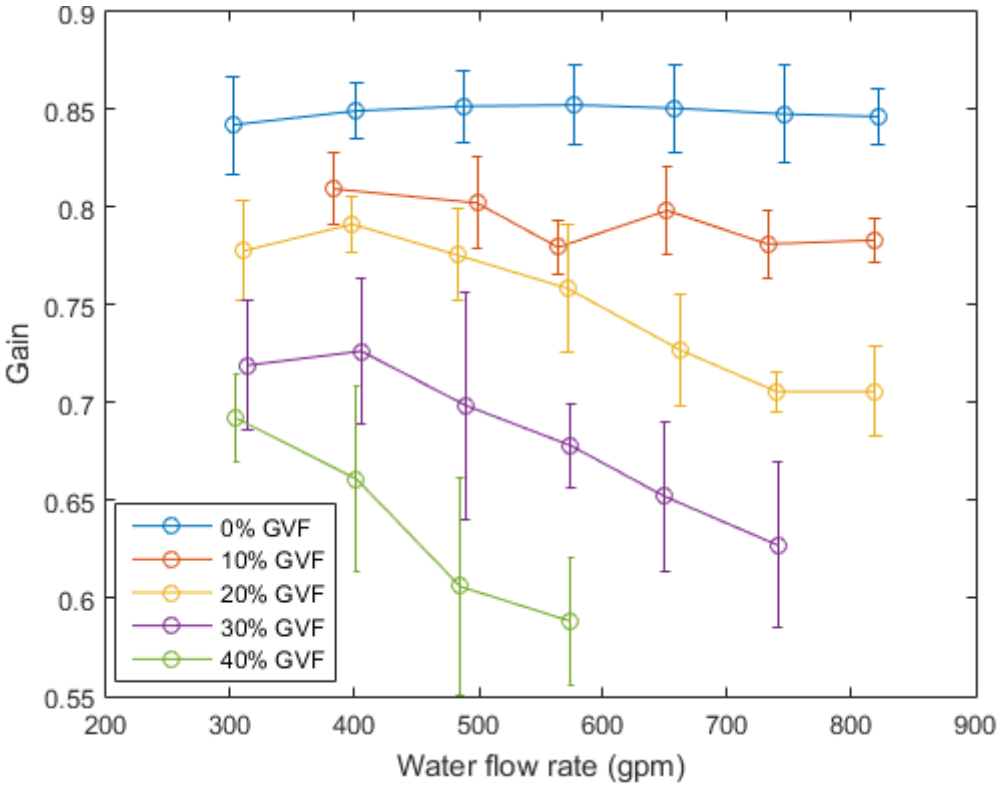

Figure 41. Gain vs. water flow rate for different GVFs (120 psig)

Although the position of the electrodes downstream of the slotted plate was chosen to be in the most homogeneously mixed region, the flow condition data was overlain on a flow regime map in order to help determine whether some sort of transition between flow regimes could explain the flow rate trend. Figure 42 shows this overlay. It is clearly seen that each flow condition was well inside the elongated bubbly flow region. So, even without a slotted plate mixing the flow, the flow should not undergo a regime transition.

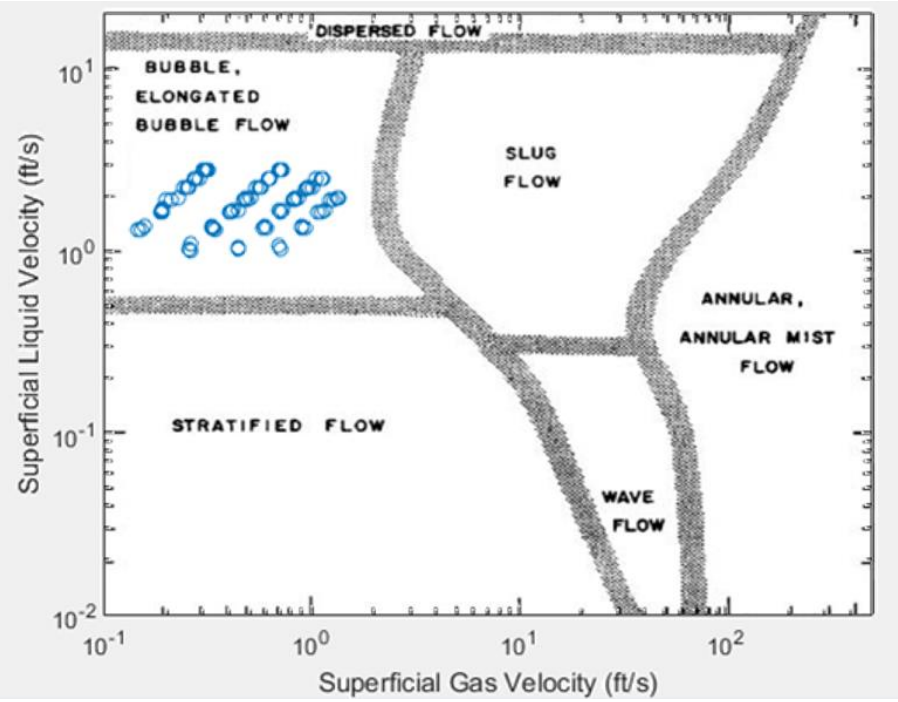

Figure 42. Flow regime map with experimental data overlayed (Mandhane, 1974 [7])

One possible reason for the flow rate and GVF trend is poor mixing from the slotted plate. When the slotted plate was designed, it was directly scaled up from a smaller version, and so the slot size is the same relative to the overall diameter of the pipe. These larger slots would likely not homogenize the flow to the same scale seen with the smaller slots. This would explain the larger variation in gains seen at higher GVFs, as there is more air passing through the plate needing to be mixed. The decrease in gain with flow rate could be due to the difference in electrical flow path geometry when larger bubbles are present.

Because visual inspection of graphs did not give many clear insights into whether the experiment's three remaining independent variables (pressure, flow rate, and GVF) had an effect on the gain, a 3-way analysis of variance (ANOVA) was performed on the data. However, the test matrix was imbalanced (i.e. some flow conditions could not be tested due to limitations of the pump), and so typical ANOVA techniques could not be applied. The number of levels of

each individual variable was reduced to that seen in Table 3 in order to have a balanced matrix. In theory, if the ANOVA results show significance for a variable or interaction between variables in the reduced table, it should also indicate significance in the full table. This is due to ANOVA taking into account the levels and degrees of freedom of the test matrix.

Table 3. Reduced test matrix for balanced ANOVA

Variable	Conditions	# of Levels
Flow Rate	305, 570, 737	3
Pressure	50, 300	2
GVF	0, 20, 30	3

Table 4 shows the results of the ANOVA. Main effects and interactions that passed the test for significance are highlighted. The results showed that with greater than 99.99% confidence, flow rate, pressure, and GVF affected the gain. Additionally, the interaction between GVF and flow rate is also highly significant.

Table 4. 3-Variable ANOVA of balanced data

	SS	*d.f.*	*MS*	*F*	F_{crit} *(p < 0.05)*	F_{crit} *(p < 0.001)*	*p-value*
Flow Rate	**3.73E-02**	**2**	**1.87E-02**	**49.30**	**3.13**	**7.64**	**< 0.0001**
Pressure	**6.35E-03**	**1**	**6.35E-03**	**16.78**	**3.98**	**11.8**	**< 0.0001**
GVF	**3.72E-01**	**2**	**1.86E-01**	**491.03**	**3.13**	**7.64**	**< 0.0001**
*Pressure*Flow Rate*	2.07E-03	2	1.04E-03	2.74	3.13	7.64	0.0713
GVF*Flow Rate	**9.96E-03**	**4**	**2.49E-03**	**6.58**	**2.5**	**5.2**	**0.0001**
*GVF*Pressure*	2.27E-03	2	1.13E-03	3.00	3.13	7.64	0.0560
*Pressure*GVF*Flow Rate*	7.44E-04	4	1.86E-04	0.49	2.5	5.2	0.7430
Error	2.72E-02	72	3.78E-04				
Total	0.457484	89					

Thus, the results of the ANOVA confirmed that flow rate and GVF were affecting the gain, as well as the inference that one was influencing the effect of the other. Additionally, it showed that pressure was affecting the gain despite it not being visually obvious.

Given the ANOVA results, a multi-variable linear quadratic regression with three independent and one dependent variable as well as interaction effects was applied to the data in order to find an equation to accurately predict GVF. The fluid static pressure, total mass flow rate, and signal gain were treated as the independent variables, while GVF was the dependent. Equation 6 is the regression result, where GVF_p is the equation-predicted GVF, P is the fluid static pressure, $\dot{m}$ is the total mass flow rate, and $Gain$ is the signal gain. Equation 9 has an r-square value of 0.963, and predicts the GVF within ±5.3% of its actual value with 95% confidence. Table 5 displays the coefficients for the equation.

$$GVF_p = A + B(P) + C(Gain) + D(\dot{m}) + E(P * Gain) + F(P * \dot{m}) + G(Gain * \dot{m}) + H(P^2) + I(Gain^2) + J(\dot{m}^2) \quad (9)$$

Table 5. Coefficients table for Equation 6

Coefficient	Value
A	7.60E+01
B	3.84E-03
C	1.43E+02
D	-2.25E+00
E	4.20E-02
F	-1.54E-04
G	2.53E+00
H	-9.73E-05
I	-2.73E+02
J	1.08E-03

Investigation of the relative contribution of each term in Equation 9 to the GVF prediction resulted in Figure 43. The contribution was calculated first by totaling the absolute value of each term in the equation, then by dividing each term by this absolute value total to obtain a percentage. Figure 43 shows that the major contributors to the calculation of GVF appear to be the constant term, gain and its squared term, flow rate, and the flow rate/GVF interaction. So, if

one desired to produce a simpler equation with fewer terms for calculations in the field, it is likely that one could perform a regression using only these terms and achieve similar accuracy.

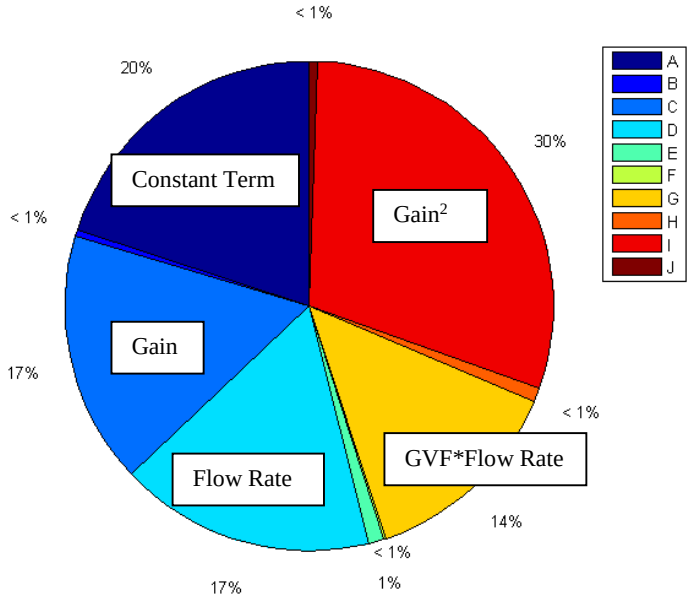

Figure 43. Graph of percentage contribution of each term (named by its coefficient) in Equation 9 to the GVF estimate.

5.3 Flow Rate Measurements

In order to have a fully functional MPFM, it is also necessary to calibrate the flow rate measurement devices. Equation 10 is the standard equation used for slotted plate orifice meters, where $\dot{m}$ is the total mass flow rate, C_D is the coefficient of discharge of the plate, A_f is the flow area of the meter, ρ is the fluid density, Δp is the pressure difference across the plate, and β is the area ratio defined by Equation 11, where A_t is the cross-sectional area of the pipe upstream

of the plate. Solving Equation 10 for C_D gives Equation 12, which was used to calculate the coefficient of discharge of the slotted plate for each flow condition tested.

$$\dot{m} = \frac{C_D}{\sqrt{1-\beta^4}} A_f \sqrt{2\rho\Delta p} \tag{10}$$

$$\beta = \sqrt{\frac{A_f}{A_t}} \tag{11}$$

$$C_D = \frac{\dot{m}\sqrt{1-\beta^4}}{A_f\sqrt{2\rho\Delta p}} \tag{12}$$

Figure 44 shows the calculated values of C_D plotted versus the density and mass flow rate of the flow. Most of the C_D values hover between 0.75 and 0.85 in Figure 44, but there is another cluster of C_D values that instead float between 0.6 and 0.7. Plotting the data with pressure on one independent axis rather than mass flow rate showed that most of these points belonged to the 50 psi static pressure data set (Figure 45).

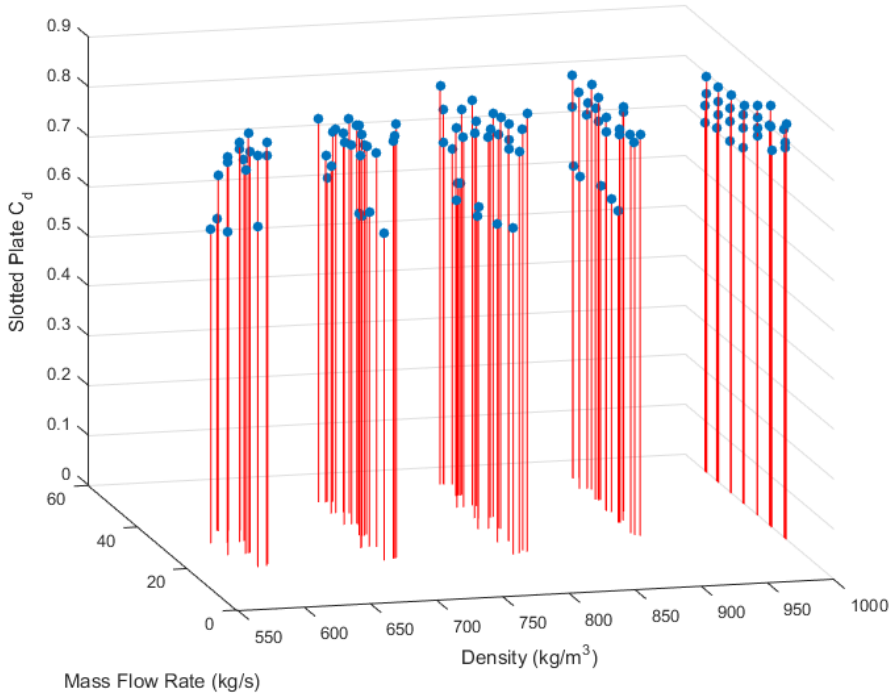

Figure 44. Slotted plate C_D vs. mass flow rate and density

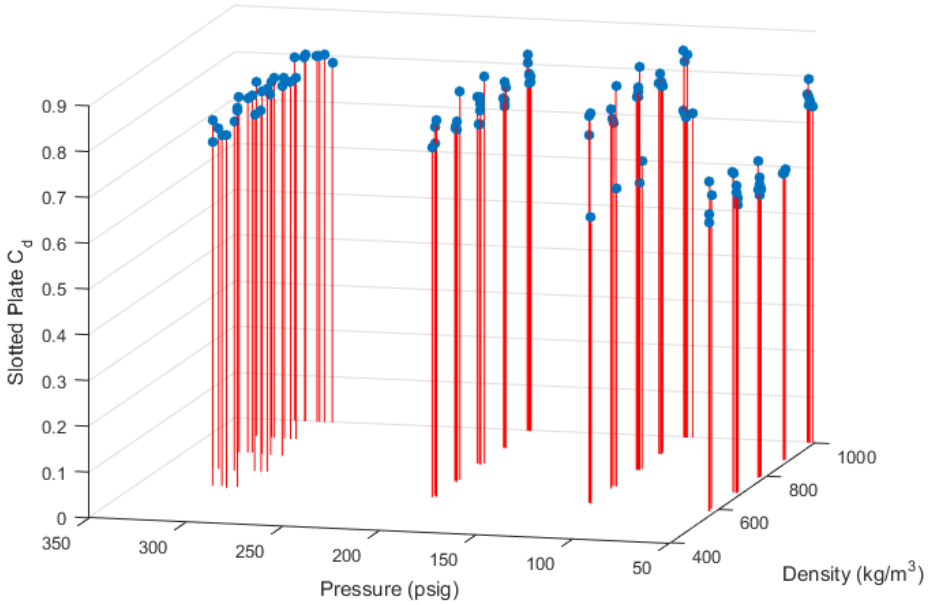

Figure 45. Slotted plate C_D vs. pressure and density

Plotting the data versus total mass flow rate showed a decreasing trend in the slotted plate's discharge coefficient with increasing total mass flow rate, as seen in Figure 46, Figure 47, Figure 48, and Figure 49. Any trend associated with changing GVF is difficult to discern except in the 300 psig data of Figure 49, where increasing GVF appears to lower the discharge coefficient. The literature has shown that a slotted plate's discharge coefficient should decrease with GVF, so the trend seen at 300 psig is consistent with the literature [4].

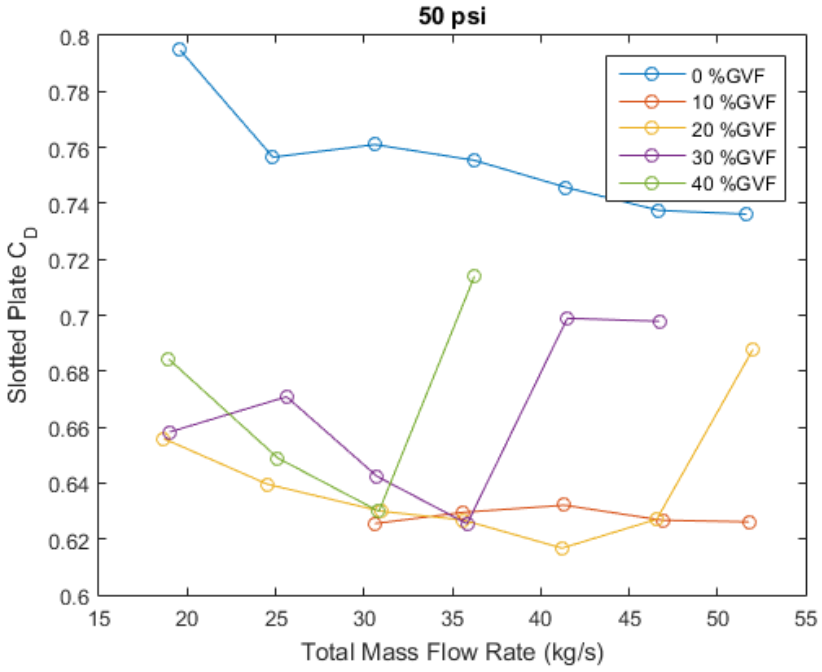

Figure 46. Slotted plate C_D vs. mass flow rate and density at 50 psig

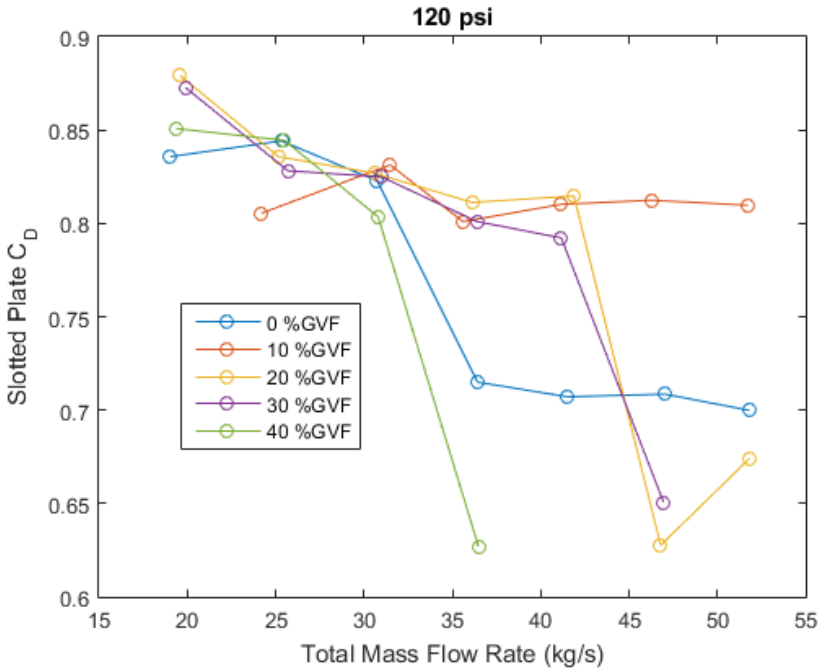

Figure 47. Slotted plate C_D vs. mass flow rate and density at 120 psig

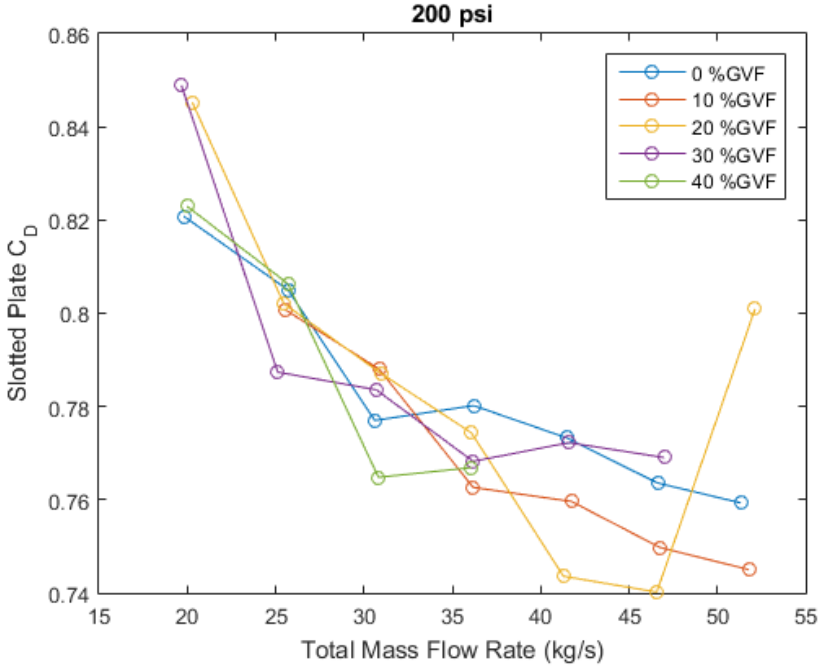

Figure 48. Slotted plate C_D vs. mass flow rate and density at 200 psig

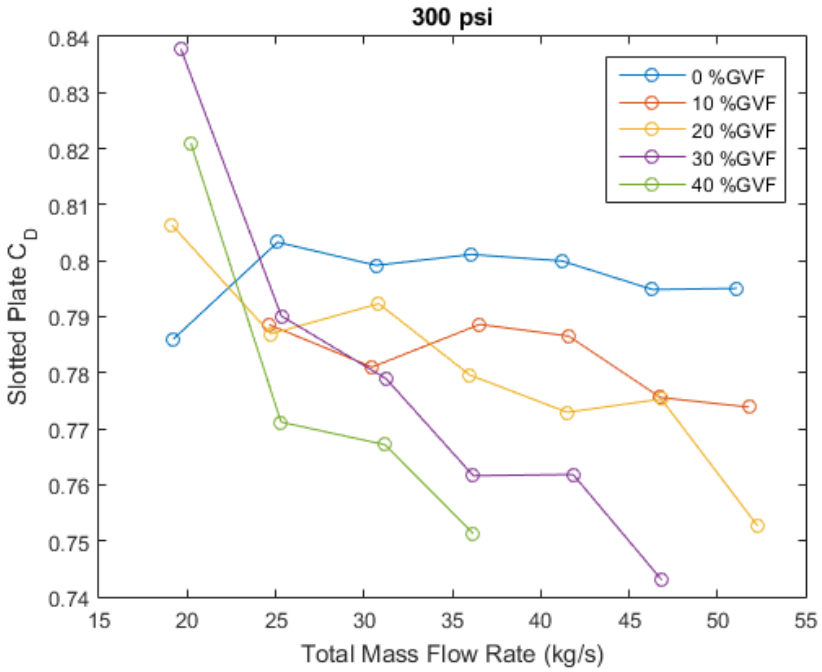

Figure 49. Slotted plate C_D vs. mass flow rate and density at 300 psig

Upon removal of the MPFM from the test loop, several large pieces of plastic were found in the piping upstream of the slotted plate, as seen in Figure 50 and Figure 51. These were most likely from the previous experiment of another student that shares the same outlet piping. During this other experiment, the acrylic pump being used failed and destroyed its own impeller. It is possible that one or more of these plastic pieces became lodged in or blocked a portion of the slotted plate during part of the 50 psi testing. This additional blockage would reduce the coefficient of discharge of the plate, and thus is a possible explanation for the discrepancy.

Figure 50. One of the plastic pieces found before the slotted plate during disassembly

Figure 51. Plastic pieces discovered during disassembly of MPFM

Plotting the slotted plate C_D versus flow rate with error bars included (Figure 52) shows much larger uncertainties at the lowest flow rates. Within these uncertainties, the decreasing trend seen with increasing flow rate could actually be nonexistent.

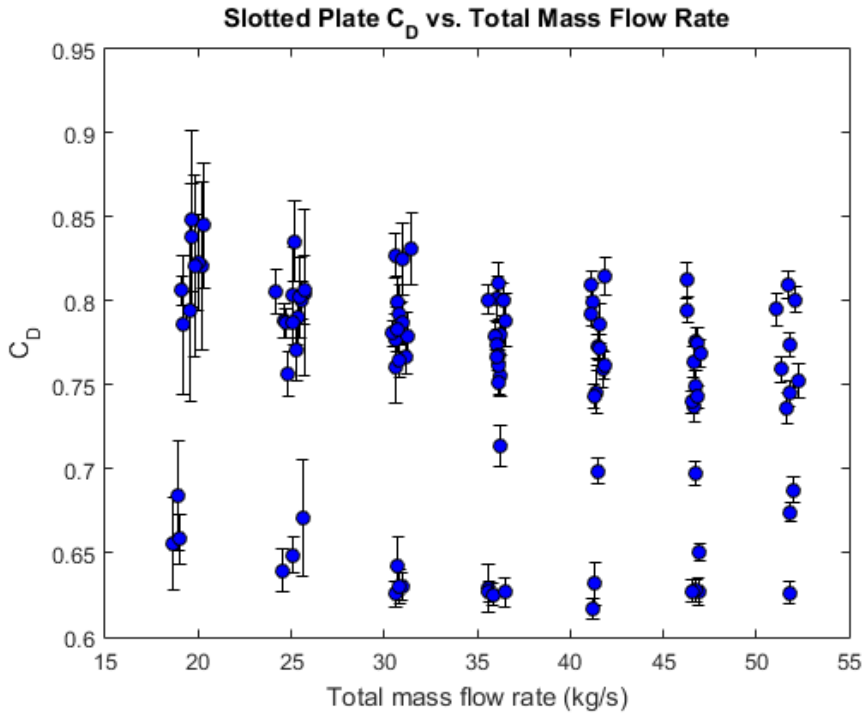

Figure 52. Slotted plate C_D vs. total mass flow rate with error bars

The uncertainties seen at lower flow rates appear to be mostly due to fluctuations in the flow rate. As the flow rate approaches the lower limit of the pump, these fluctuations increase dramatically. Figure 53 shows the standard deviation in flow rate for each data point versus their flow rate. Based on this correlation, it seems that for this test setup, predicting the exact flow rate is more difficult at lower flow rates.

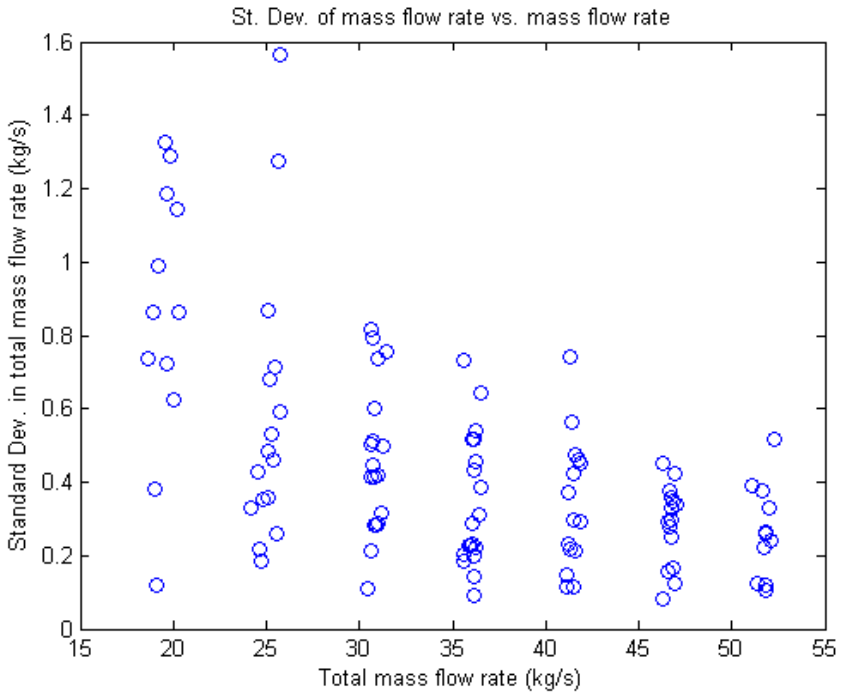

Figure 53. Standard deviation in mass flow rate vs. mass flow rate

Calibration of the Venturi tube flow meter was performed similarly to that of the slotted plate, as the equations are very similar. Equations 13-15 apply to the venturi, where $C_{D,v}$ is the coefficient of discharge for the venturi, β_v is its area ratio, A_2 is the cross-sectional area of the constricted portion of the venturi, and all other variables are identical to those of the slotted plate.

$$\dot{m} = \frac{C_{D,v}}{\sqrt{1-\beta^4}} A_2 \sqrt{2\rho\Delta p} \tag{13}$$

$$\beta_v = \sqrt{\frac{A_2}{A_1}} \tag{14}$$

$$C_{D,v} = \frac{\dot{m}\sqrt{1-\beta^4}}{A_2\sqrt{2\rho\Delta p}} \tag{15}$$

Figure 54 shows $C_{D,v}$ plotted versus the mass flow rate and density. It can be seen that the calculated $C_{D,v}$ stays fairly close to a value of 1, as expected for a venturi.

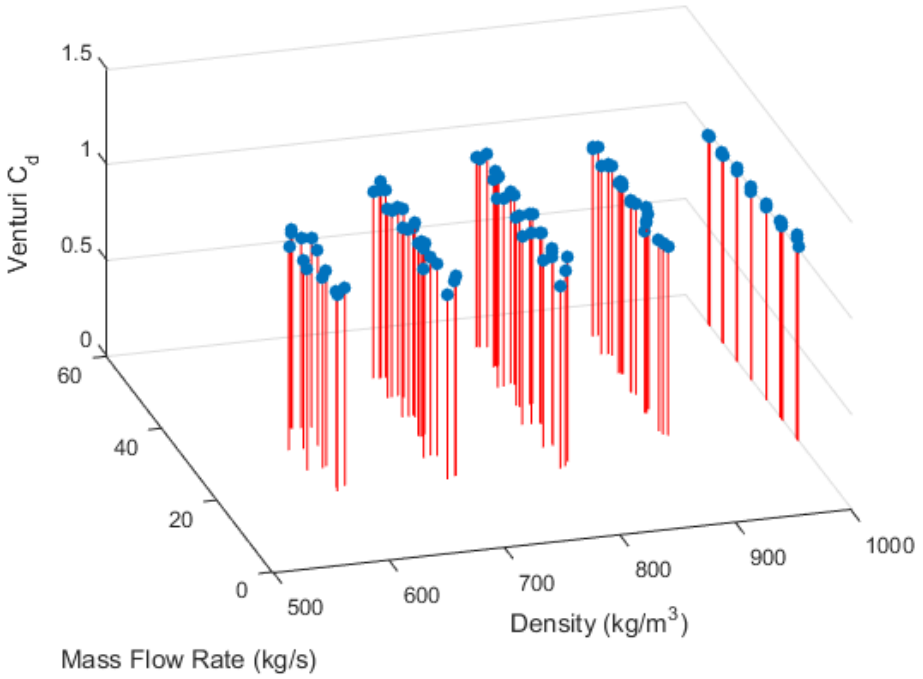

Figure 54. Venturi C_D vs. mass flow rate and density

Plotting the venturi's C_D versus total mass flow rate did not show the same consistent decrease in C_D with increasing mass flow rate seen for the slotted plate except at the higher pressures of 200 and 300 psi, as seen in Figure 55, Figure 56, Figure 57, and Figure 58. Again, any trend associated with GVF is difficult to discern.

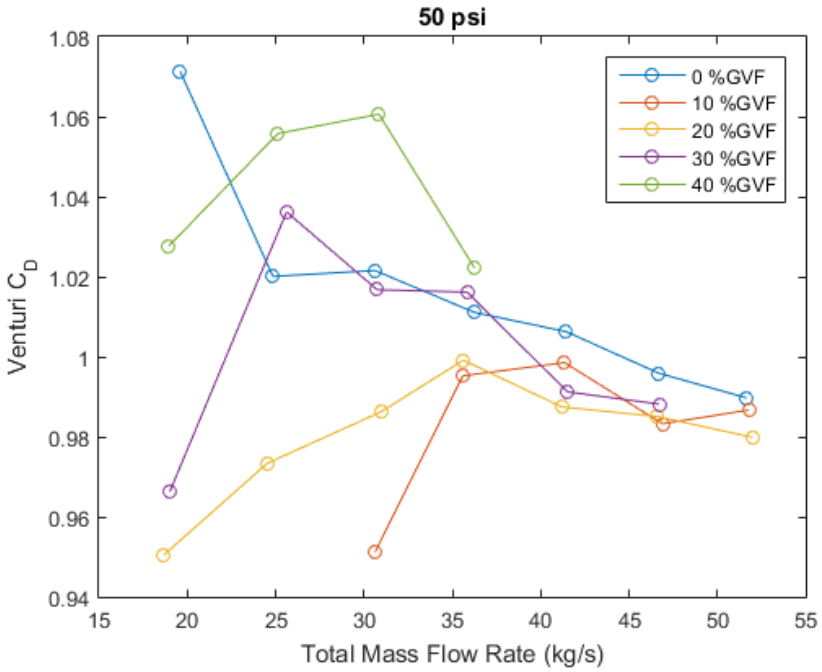

Figure 55. Venturi C_D vs. mass flow rate and density at 50 psig

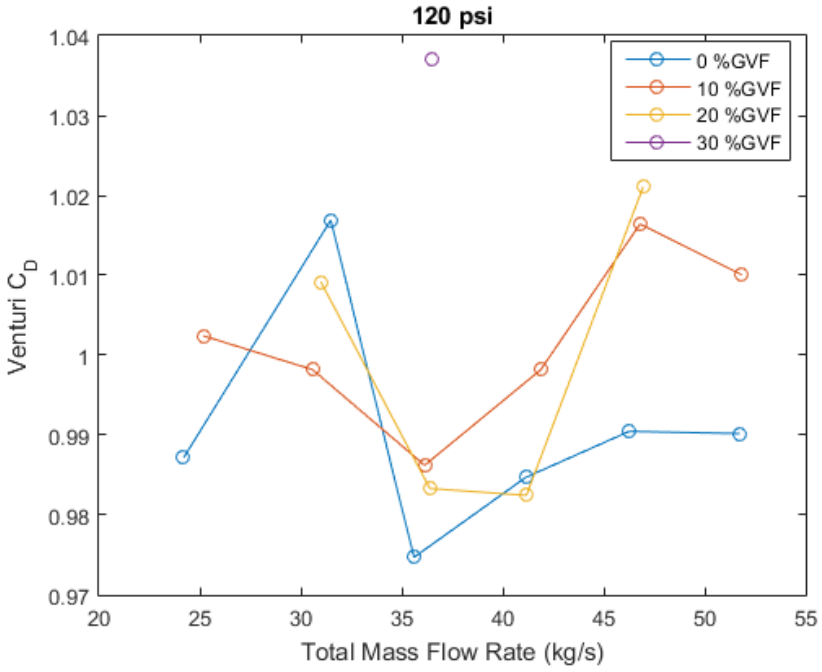

Figure 56. Venturi C_D vs. mass flow rate and density at 120 psig

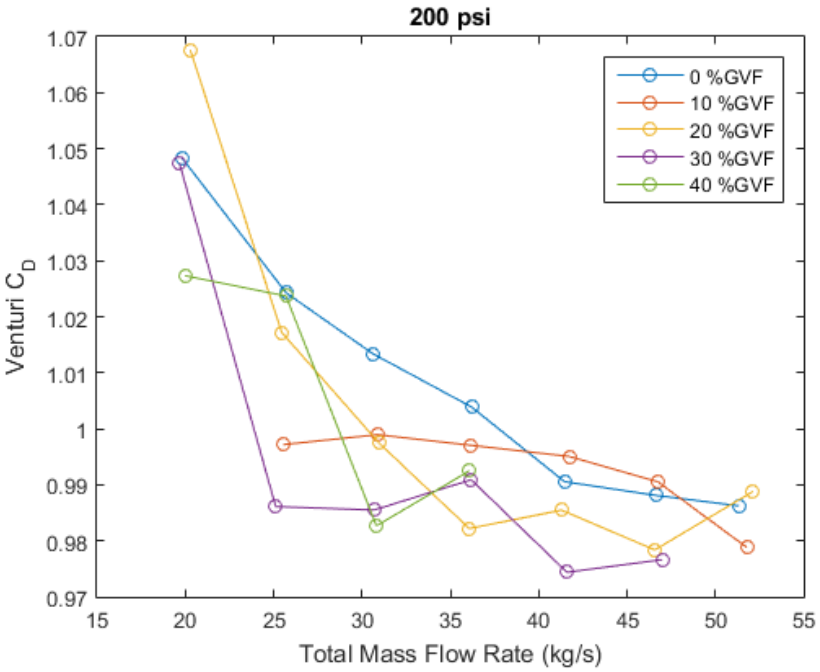

Figure 57. Venturi C_D vs. mass flow rate and density at 200 psig

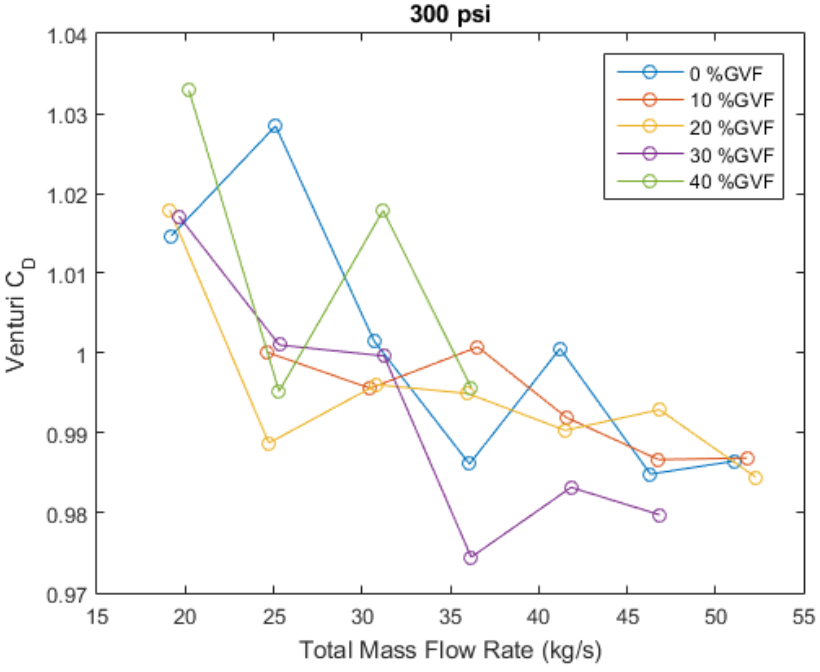

Figure 58. Venturi C_D vs. mass flow rate and density at 300 psig

Plotting the venturi C_D versus mass flow rate with error bars included showed the same trend as with the slotted plate: increased uncertainty for lower flow rates. Again, this is likely due to the fluctuations in flow rate seen at lower flow rates. Similarly, this implies greater difficulty in predicting flow rate at lower flow rates even for the venturi.

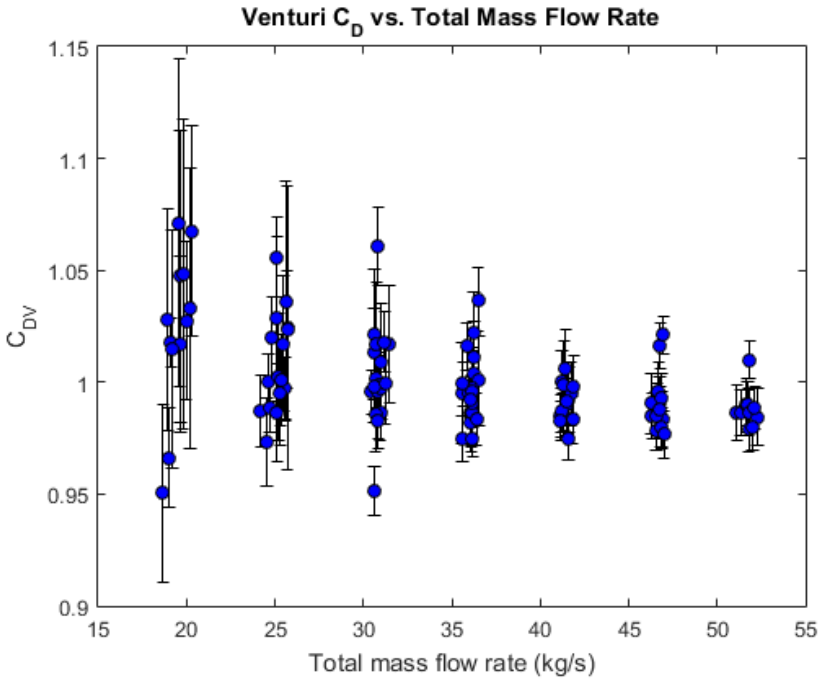

Figure 59. Venturi C_D vs. total mass flow rate

Selecting a single C_D for each flow measurement device to re-calculate the flow rates using their respective equations showed measurement accuracies displayed in Table 6. The C_D's were selected by averaging the calculated C_D's for the slotted plate, and by trial-and-error iterations for the venturi. The slotted plate showed a large measurement uncertainty of ±19.1% with 95% confidence while looking at all data points. If one removes the anomalous C_D data points from the analysis, however, the uncertainty is improved to ±8.80%. This is still about twice the uncertainty of a typical slotted orifice plate meter. The venturi showed a measurement

uncertainty of ±4.53%, which is not optimal for a venturi, but is still certainly within its range. Due to the higher accuracy of the venturi meter (and confounded nature of the slotted plate data), it is the primary device used in determining the overall measurement accuracy of the MPFM.

Table 6. Flow measurement device accuracies

Flow measurement device	**C_D used**	**Uncertainty (95% confidence)**
Slotted plate	0.7535	±19.1%
Slotted plate (anomalous points removed)	0.7854	±8.80%
Venturi	0.9983	±4.53%

5.4 Combined GVF and Flow Rate Measurements

The flow rate prediction accuracy reported in Table 6, however, is only valid when the density of the fluid is already known. This would likely not be the case in a situation where this MPFM is needed, as the MPFM provides the GVF, and therefore density, information. Since flow rate was shown to have a significant effect on the GVF predictions of the MPFM, both GVF and flow rate are interdependent. In other words, to know one accurately, one must know the other.

This trap can be avoided, however, using an iterative prediction method as follows:

1. An initial GVF prediction is obtained by assuming an arbitrary flow rate (in this case, the mean flow rate condition tested) in Equation 9
2. Flow rate is calculated using the initial GVF prediction in Equation 13.
3. The flow rate obtained from Equation 13 is used in Equation 9 to obtain a better GVF prediction.

4. This improved GVF is used to better predict the flow rate using Equation 13.
5. Steps 3 and 4 are repeated until the percent change in GVF or flow rate from each iteration to the next is minimal.

For this analysis, the above method was allowed to continue until the change in predicted flow rate from iteration to iteration was less than 0.1%. This resulted in flow rate measurements with an uncertainty of ±6.14% of the actual value with 95% confidence. GVF measurements showed uncertainty of ±5.85% GVF. These results are similar to those seen by Sihombing (2015), showing that the MPFM concept appears valid even for NPS 6" piping and the more extreme pressures and flow rates tested.

The MPFM design was also relatively inexpensive to produce: the entire prototype including DAQ equipment and the venturi tube flow meter cost less than $50,000. In large scale production, this cost would be reduced significantly.

6. CONCLUSIONS AND RECOMMENDATIONS

The testing and evaluation of the electrical impedance-based MPFM for large diameter pipe described in this thesis showed that multiple variables and mixture properties affected the meter's readings: signal frequency, temperature, pressure, flow rate, and mixture GVF. The signal gains corresponding to the 7.82 MHz frequency showed the strongest difference across the GVFs tested, making 7.82 MHz the primary frequency used for analysis. It was possible to use regression techniques to eliminate the temperature effect for each frequency and GVF tested. The temperature correction factor equations were found not to vary much with GVF, and so the correction equation for 0% GVF could be used.

Analysis of variance techniques were applied to the data and confirmed that pressure, total mass flow rate, GVF, and the interaction between flow rate and GVF all had a statistically significant effect on the MPFM's gain. Flow rate and pressure effects had not been seen with 2" electrical impedance-based MPFMs of similar design. Based on the ANOVA results, a multi-variable regression was performed on the data to obtain a calibration equation for the MPFM. This equation was capable of predicting the GVF of the fluid mixture within ±5.3% GVF with 95% confidence given knowledge of the flow rate.

Calculations of the discharge coefficient were carried out for both the slotted plate and venturi tube flow meters. The slotted plate data had anomalies that could possibly be explained by large pieces of plastic found upstream that could have blocked flow through the plate during operation. Ignoring the anomalous data, however, the slotted plate predicted the total flow rate of the fluid mixture with an uncertainty of ±8.8%. The venturi had much more consistent data, and could predict total flow rate with an uncertainty of ±4.53%.

However, these flow rate prediction accuracies are based on knowing the density (or GVF) of the fluid mixture. So, in order for the MPFM to function accurately, an iterative method was applied to estimate both GVF and total flow rate. This method resulted in flow rate prediction with an uncertainty of ±6.14%, and GVF prediction uncertainty of ±5.85% GVF.

Based on these results, it appears that the MPFM design described in this report has the potential to be a viable flow measurement device for air-water flows in pipes as large as 6", with water flow rates as high as 820 gpm and pressures upward of 350 psig. In addition, it is relatively low cost—the prototype being constructed for less than $50,000. In order to improve the measurement accuracy of the MPFM in future testing, the following recommendations are made:

- Reduce slot size while maintaining β ratio of slotted plate. This could improve mixing of the two fluids, as mixture homogeneity does not necessarily remain the same as slot size is increased [14].
- Increase output voltage of signal generation device. For smaller pipe diameters (and especially those of pipes made of polymers), the ±2V from the Picoscope was sufficient. With a larger diameter, however, there is more room for variation in flow patterns, and so a stronger signal could overpower more signal noise.
- Increase the signal measurement buffer size. This would help reduce random error in the data.

While the MPFM conceptual design sufficed for this experiment, several areas of improvement were identified throughout the testing experience:

- Eliminating the alumina rings in favor of alumina inserts of some kind would reduce the risk of failure due to having the ceramic in tension. While precautions were taken to minimize the amount of tension to be seen in the current design and the rings remained

intact during testing, the ring design does have inherent risk due to putting the ceramic in tension. The alumina rings were also considerably expensive, and so reducing the size and manufacturing difficulty of the insulator parts would greatly reduce cost.

- Manufacturing the brass electrodes in a way that allows wire to be soldered to the electrode prior to installation in the device would be preferred over the current configuration which required attachment through the small access hole in the housing.

REFERENCES

[1] Falcone, G. (2001). *Multiphase Flow Metering: Current Trends and Future Developments*. Proceedings of the 2001 Society of Petroleum Engineers Annual Technical Conference, New Orleans, LA.

[2] Da Silva, M. J. (2008). Impedance sensors for fast multiphase flow measurement and imaging (Doctoral dissertation). Technische Universtaat Dresden, Dresden, Germany.

[3] Sihombing, D. (2015) Temperature Effect in Multiphase Flow Meter Using Slotted Orifice Plate (Master's thesis). Texas A&M University, College Station, Texas.

[4] Morrison, G. L., Pirouzpanah, S., Cevik, M., & Patil, A. (2013, July 7-11). *Evaluation of a close coupled slotted orifice, electrical impedance, and swirl flow meters for multiphase flow*. Proceedings of the ASME 2013 Fluids Engineering Division Summer Meeting, Incline Village, NV. Retrieved June 11, 2015, from http://proceedings.asmedigitalcollection.asme.org

[5] Andreussi, P., Di Donfransesco, A. D., & Messi, M. (1988). An impedance method for the measurement of liquid hold-up in two-phase flow. *International Journal Multiphase Flow, 14*(6), 777-785.

[6] Corneliussen, S., Couput, J. P., Dahl, E., Dykesteen, E., Froysa, K. E., Malde, E., & Tunheim, H. (2005). Handbook of the multiphase flow metering (Rev. 2). The Norwegian Society for Oil and Gas Measurement and The Norwegian Society of Chartered Technical and Scientific Professionals. Retrieved November 6, 2014, from http://www.nfogm.no

[7] Mandhane, J. M., Gregory, G. A., & Aziz, K. (1974). A flow pattern map for gas-liquid flow in horizontal pipes. *International Journal Multiphase Flow, 1*, 537-553.

[8] Coleman, J. W., & Garimella, S. (1999). Characterization of two-phase flow patterns in small diameter round and rectangular tubes. *International of Heat and Mass Transfer, 42*, 2869-2881.

[9] Bratland, O. (2013). Pipe Flow 2: Multi-phase flow assurance. Retrieved June 25, 2015, from http://www.drbratland.com

[10] Orifice, Nozzle, and Venturi Flow Rate Meters. *The Engineering ToolBox.* Accessed June 30, 2015. http://www.engineeringtoolbox.com/orifice-nozzle-venturi-d_590.html

[11] Morrison, G. L., Hall K. R., Holste, J. C., Macek, M. L., Ihfe, L. M., DeOtte, R. E., Jr., & Terracina, D. P. (1994). Comparison of Orifice and Slotted Plate Flowmeters. *Flow Measurement and Instrumentation,* 5(2), 71-74.

[12]Macek, M. L. (1993). A Slotted Orifice Plate Used as a Flow Measurement Device (Master's thesis). Texas A&M University, College Station, TX.

[13] Morrison, G. L., Terracina, D. P., & Brewer, C. (2001). Response of a slotted orifice flow meter to an air/water mixture. *Flow Measurement and Instrumentation, 12*, 175-180.

[14] Sparks, S. A. (2004). Two phase mixing comparison, oil contamination comparison, and manufacturing accuracy effect on calibration of slotted orifice flow meters (Master's thesis). Texas A&M University, College Station, TX.

[15] Annamalai, G. (2014). Characterization of flow homogeneity downstream of a slotted plate in a two-phase flow using electrical resistance tomography (Master's thesis). Texas A&M University, College Station, TX.

[16] Liptak, B. (2003). Instrument Engineers' Handbook: Process Measurement and Analysis, Fourth Edition.. Boca Raton, Florida. CRC Press.

[17] Hasan, Abbas (2012). Theoretical and Experimental Study of Bubbly Gas-water Two Phase Flows through a universal venturi tube. *International Journal of Information Science and Education, 2(1), 43-58.*

[18] Thorn, R., Johansen, G. A., & Hjertaker, B. T. (2013). Three-phase flow measurement in the petroleum industry. *Measurement Science and Technology, 24*(1), 1-17. doi:10.1088/0957-0233/24/1/012003

[19] Fossa, M. (1998). Design and performance of a conductance probe for measuring the liquid fraction in two-phase gas-liquid flows. *Flow Measurement and Instrumentation, 9,* 103-109.

[20] Pirouzpanah, S. (2014). Study of hysteresis and emulsion properties in watercut measurement using high speed multi-frequency impedance sensor. *Flow Measurement and Instrumentation*, 40, 1-8.

[21] Kirkland, K. (2012). Design and fabrication of a vertical pump multiphase flow loop (Master's thesis). Texas A&M University, College Station, TX.

[22] Ihfe, L. M. (1994). Development of the slotted orifice flow conditioner (Master's thesis). Texas A&M University, College Station, TX.

[23] Baker, R. C. (2000). Flow Measurement Handbook: Industrial Designs, Operating Principles, and Applications. Cambridge, UK: Cambridge University Press.

[24] Geng, Y., Zheng, J., & Shi, T. (2006). Study on the metering characteristics of a slotted orifice for wet gas flow. *Flow Measurement and Instrumentation, 17*, 123-128.

[25] Husain, Z. (1995). Theoretical Uncertainty of Orifice Flow Measurement. *Daniel Flow Products, Inc.* Accessed July 8, 2015. http://docslide.us/documents/theoretical-uncertainty-of-orifice-flow-measurement-172kb.html

APPENDIX A FIGURES

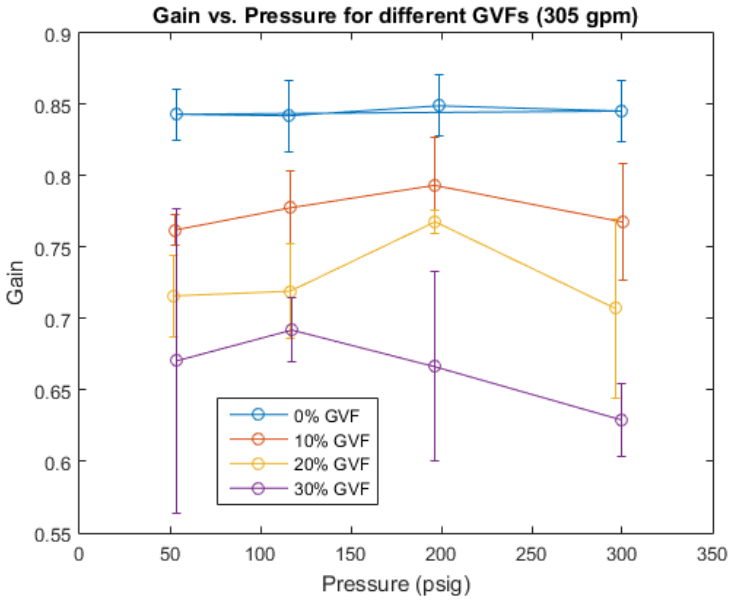

Figure 60. Gain vs. pressure for different GVFs (305 gpm)

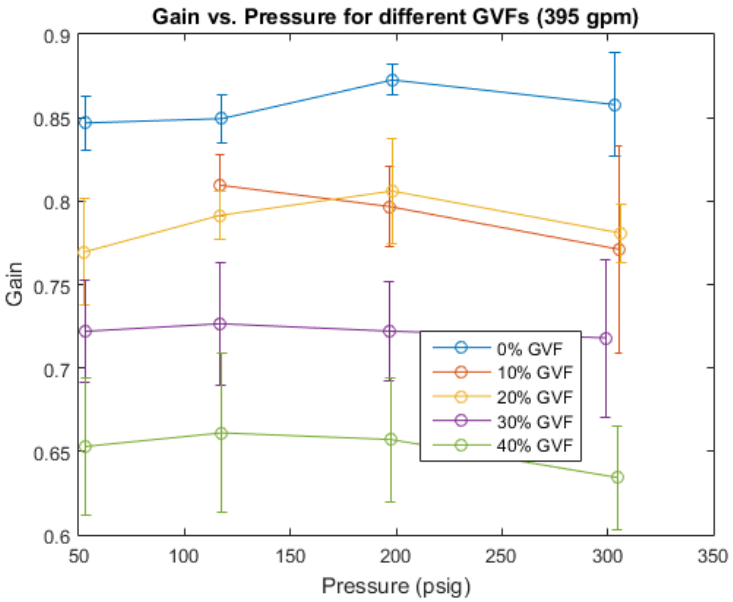

Figure 61. Gain vs. pressure for different GVFs (395 gpm)

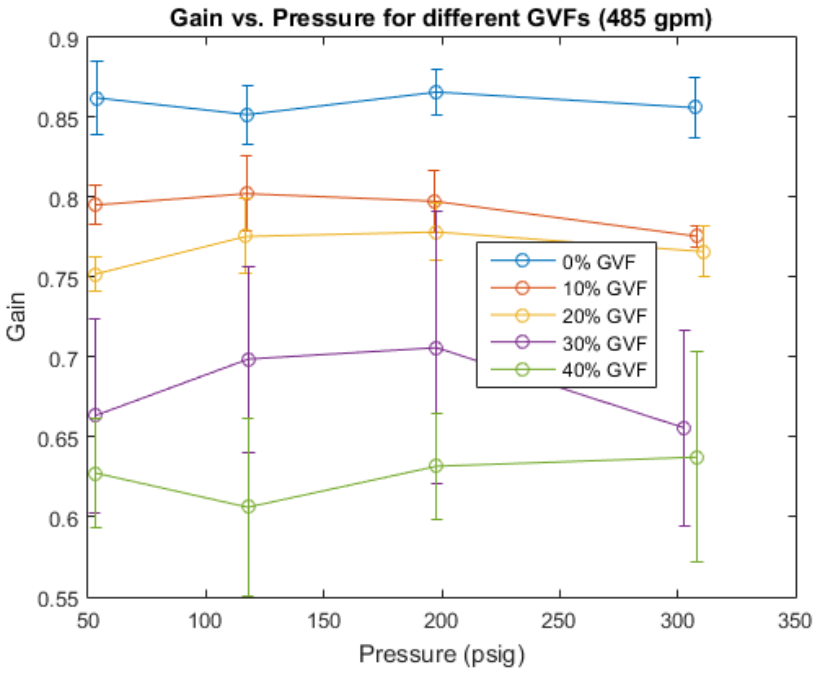

Figure 62. Gain vs. pressure for different GVFs (485 gpm)

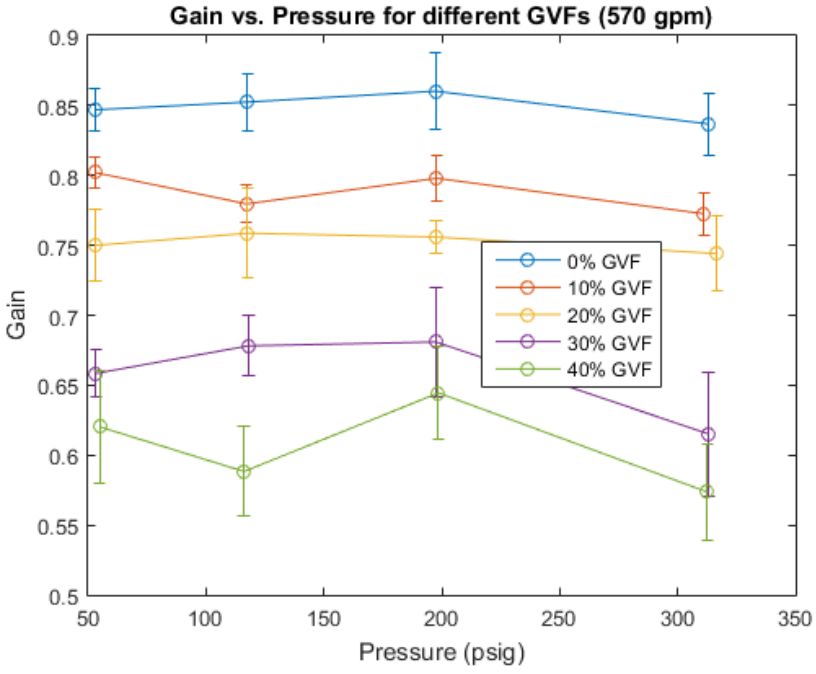

Figure 63. Gain vs. pressure for different GVFs (570 gpm)

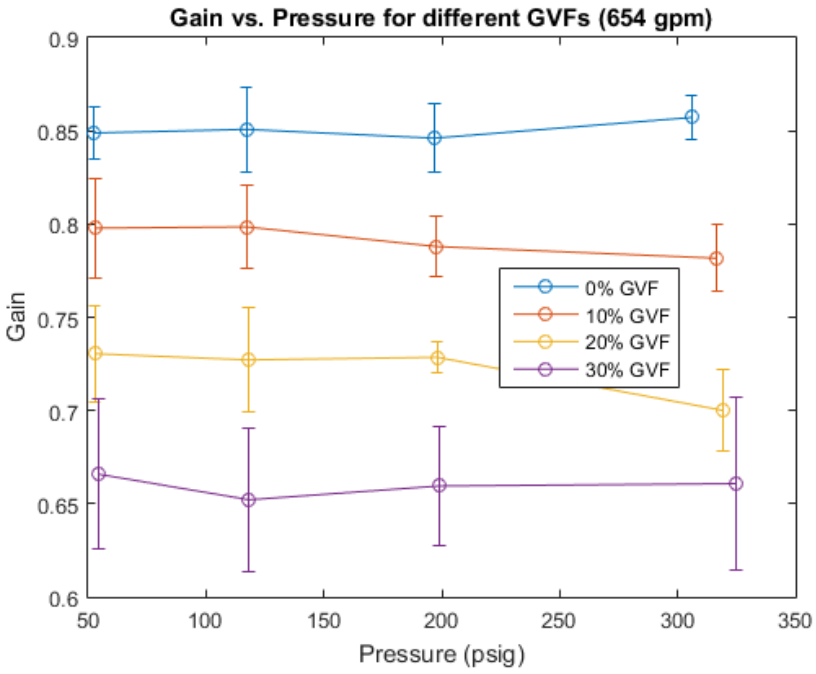

Figure 64. Gain vs. pressure for different GVFs (654 gpm)

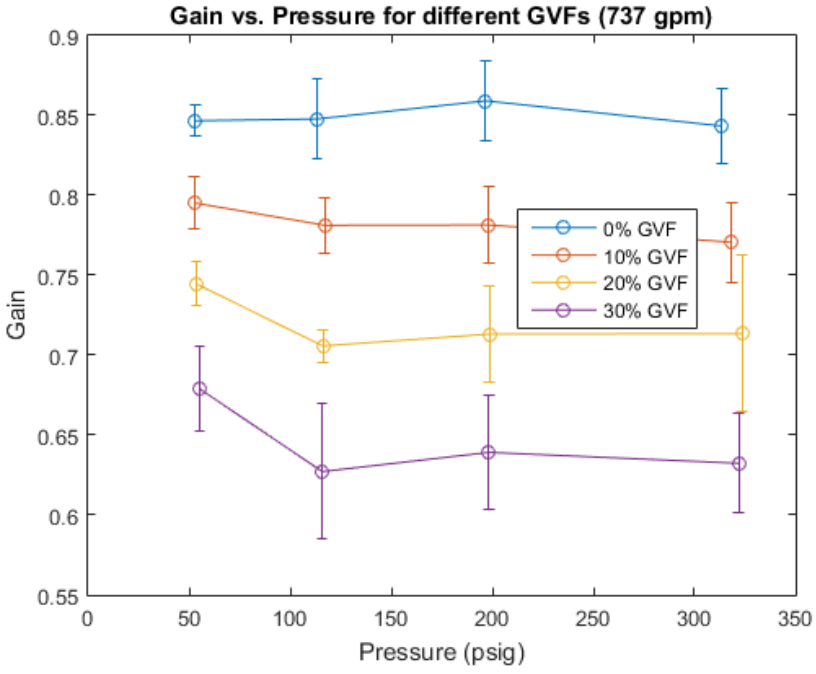

Figure 65. Gain vs. pressure for different GVFs (737 gpm)

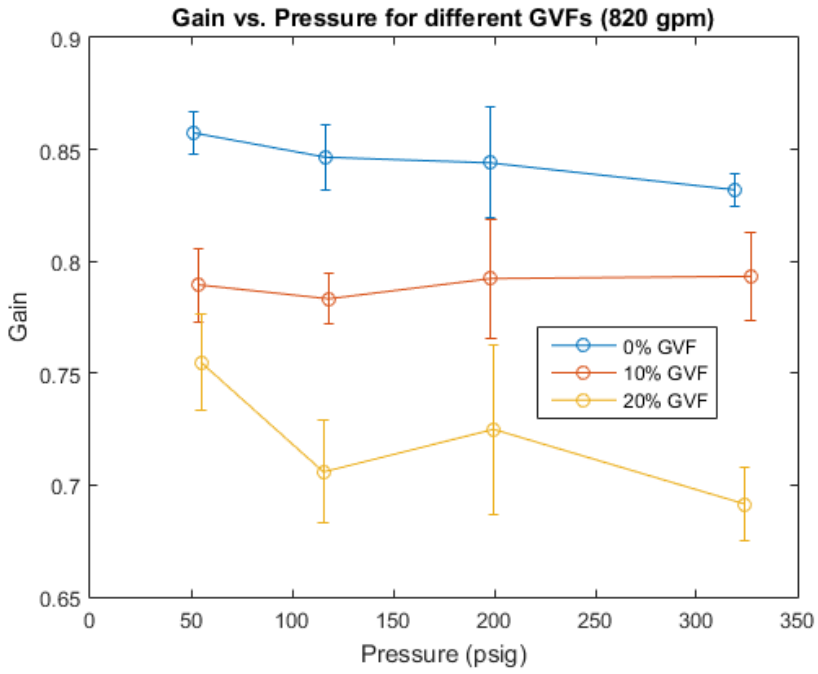

Figure 66. Gain vs. pressure for different GVFs (820 gpm)

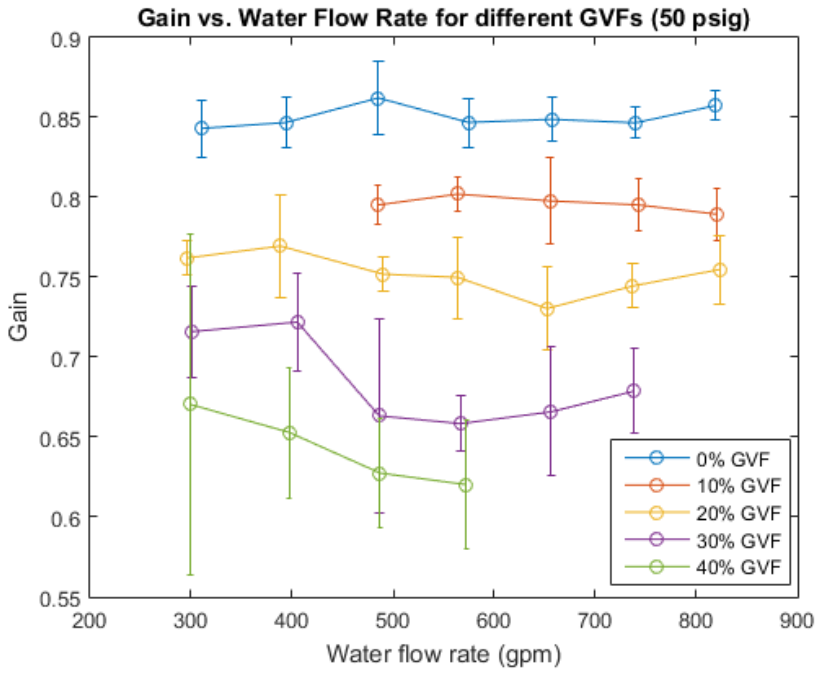

Figure 67. Gain vs. water flow rate for different GVFs (50 psig)

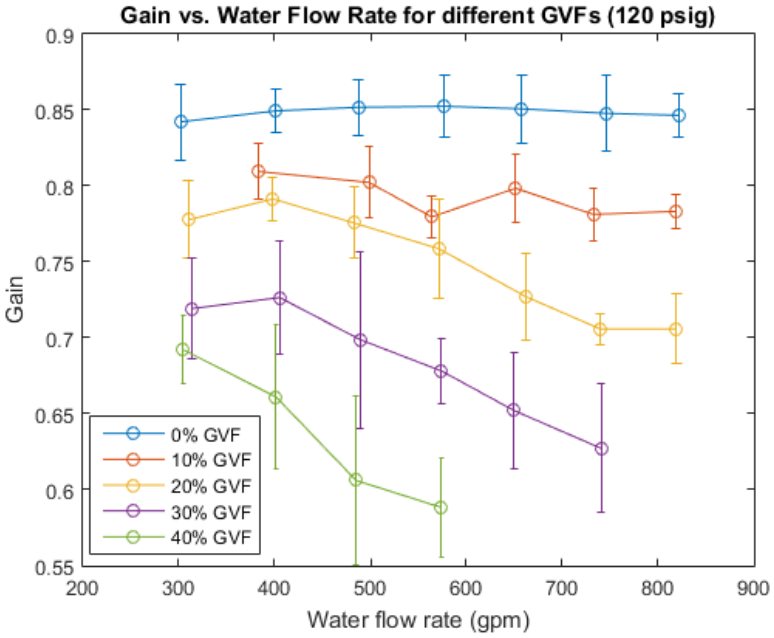

Figure 68. Gain vs. water flow rate for different GVFs (120 psig)

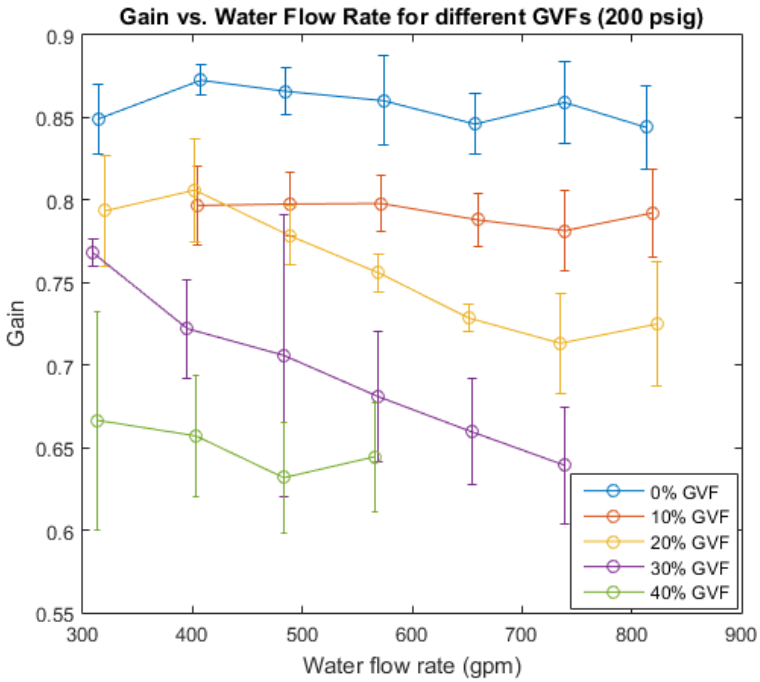

Figure 69. Gain vs. water flow rate for different GVFs (200 psig)

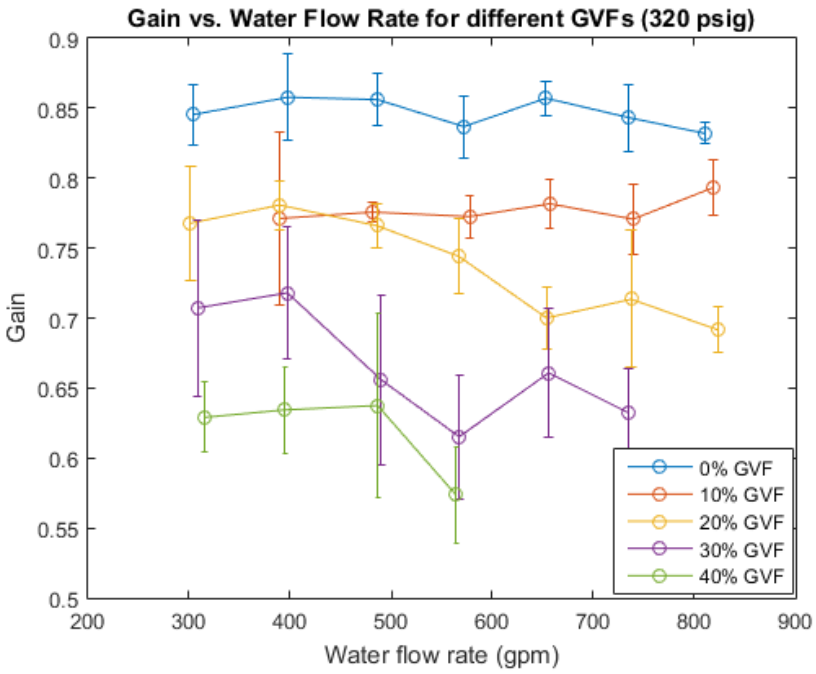

Figure 70. Gain vs. water flow rate for different GVFs (320 psig)

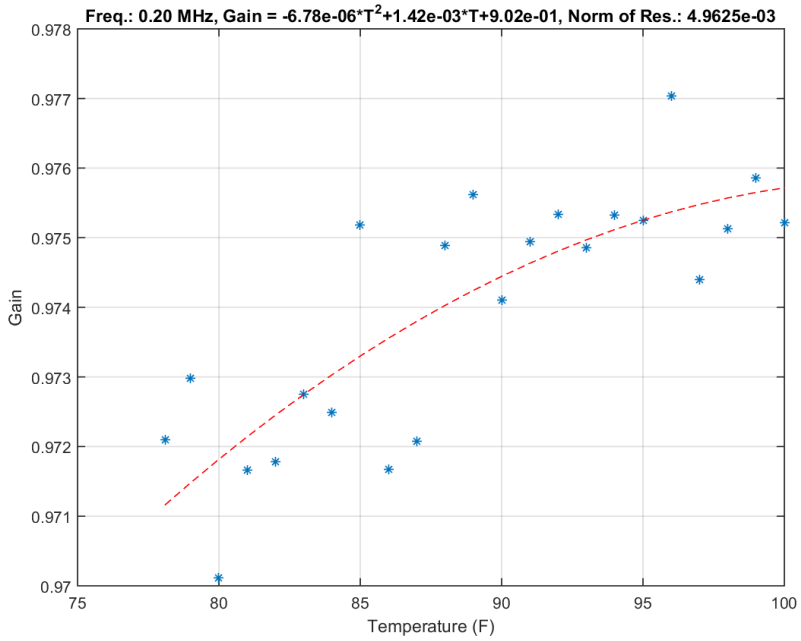

Figure 71. Gain vs. temperature (0.2 MHz)

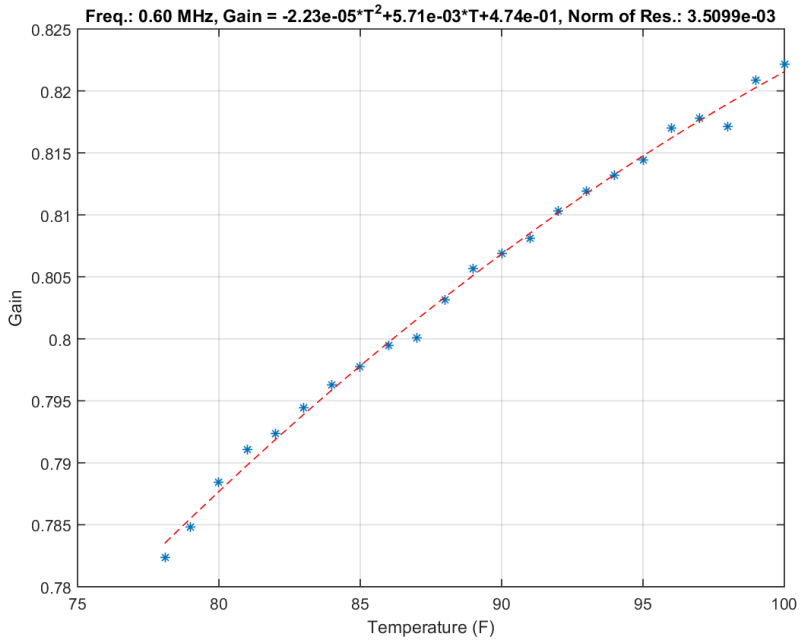

Figure 72. Gain vs. temperature (0.6 MHz)

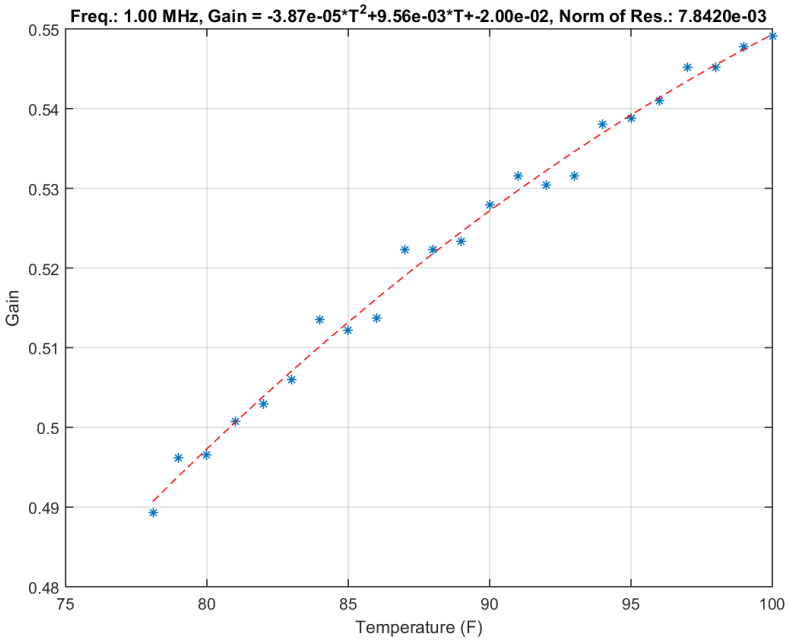

Figure 73. Gain vs. temperature (1.0 MHz)

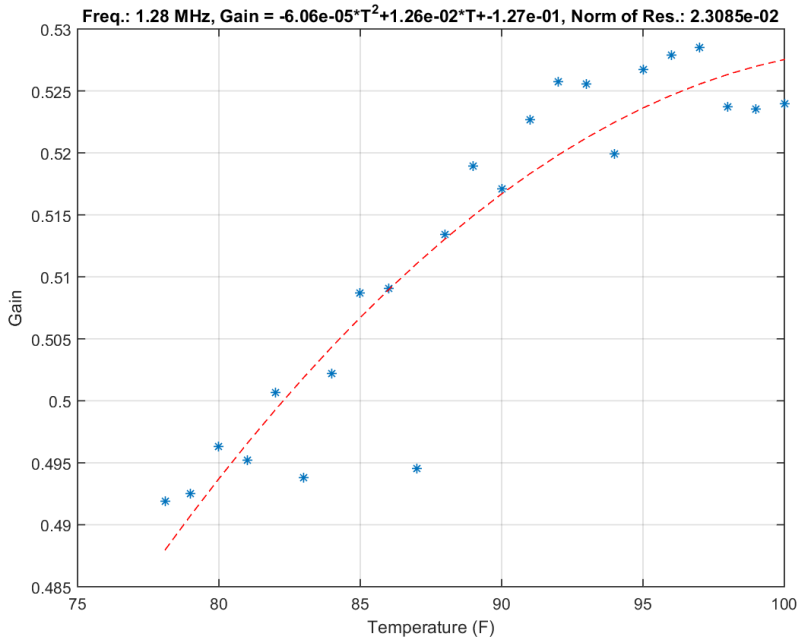

Figure 74. Gain vs. temperature (1.28 MHz)

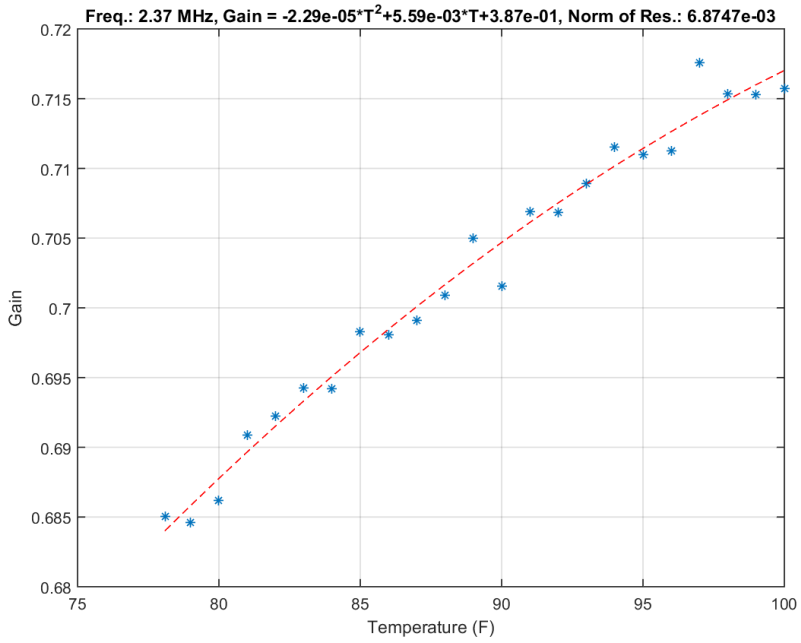

Figure 75. Gain vs. temperature (2.37 MHz)

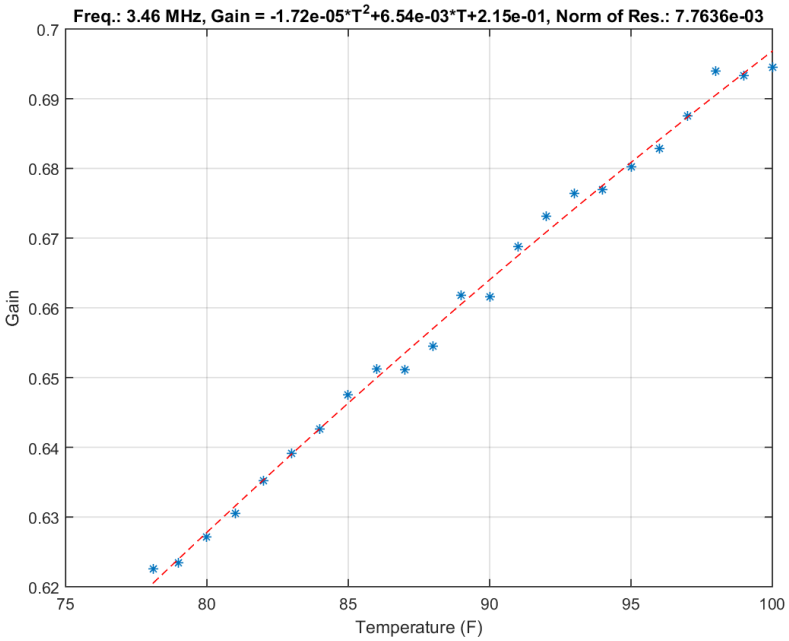

Figure 76. Gain vs. temperature (3.46 MHz)

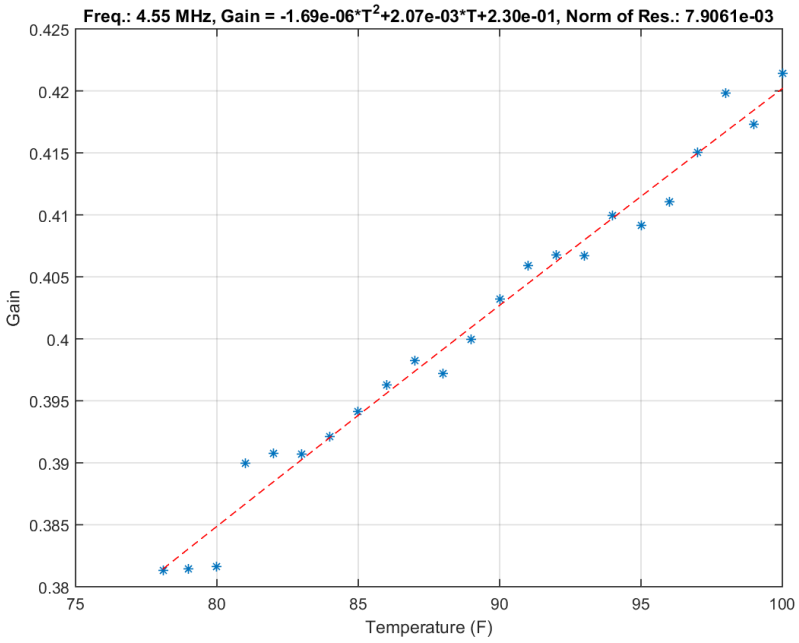

Figure 77. Gain vs. temperature (4.55 MHz)

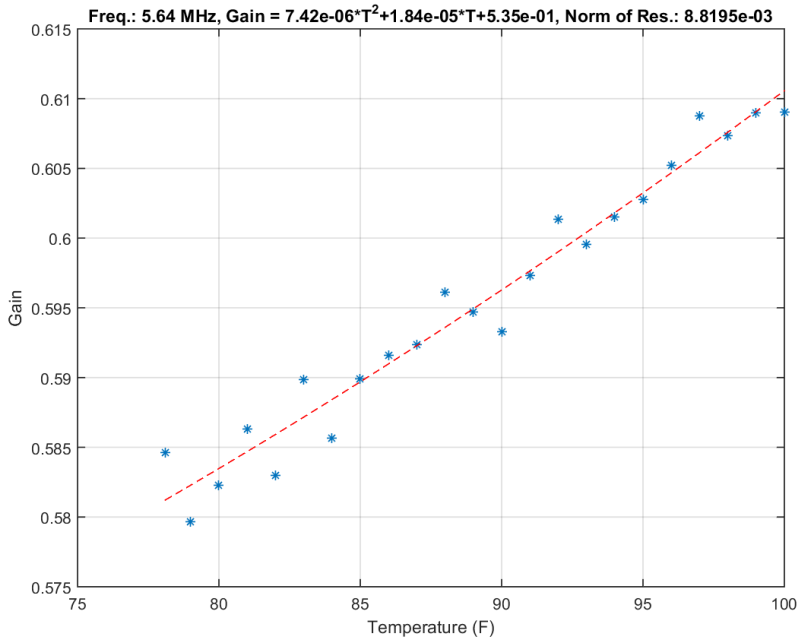

Figure 78. Gain vs. temperature (5.64 MHz)

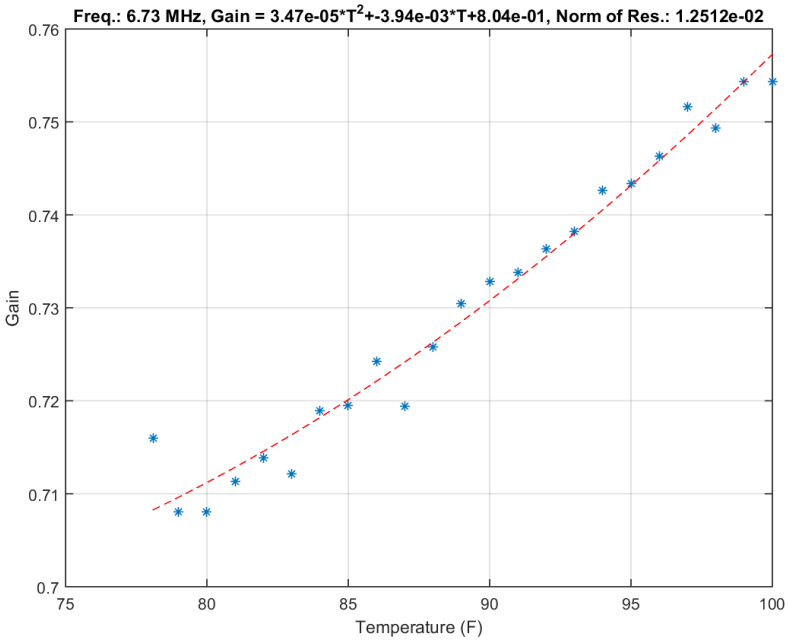

Figure 79. Gain vs. temperature (6.73 MHz)

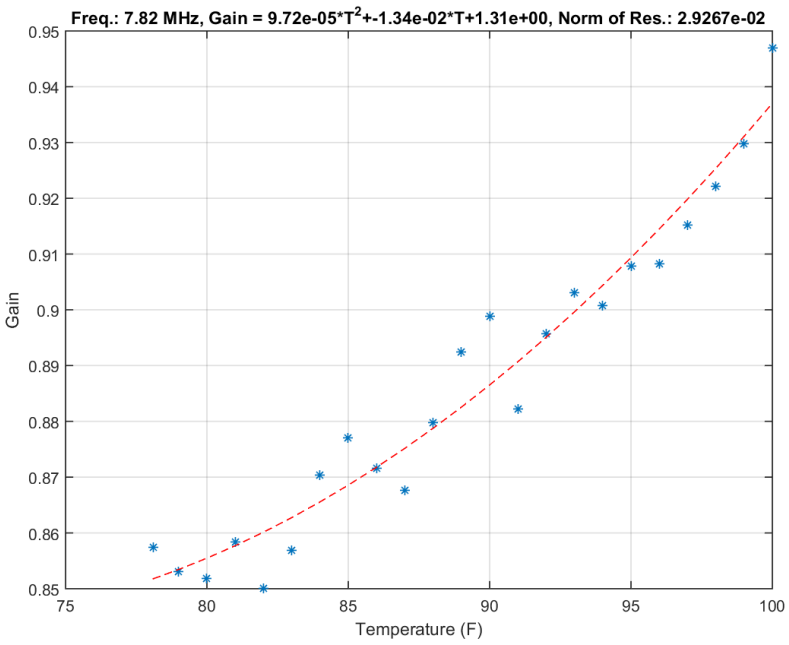

Figure 80. Gain vs. temperature (7.82 MHz)

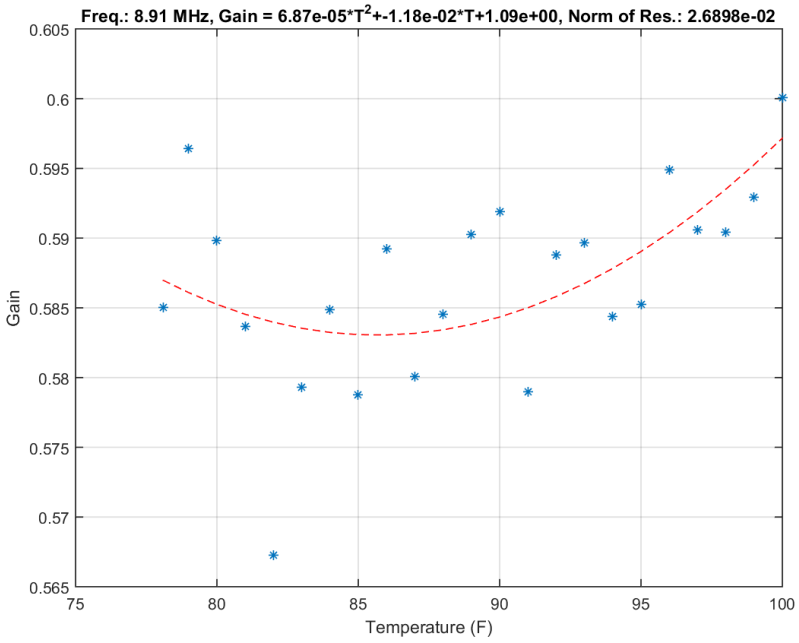

Figure 81. Gain vs. temperature (8.91 MHz)

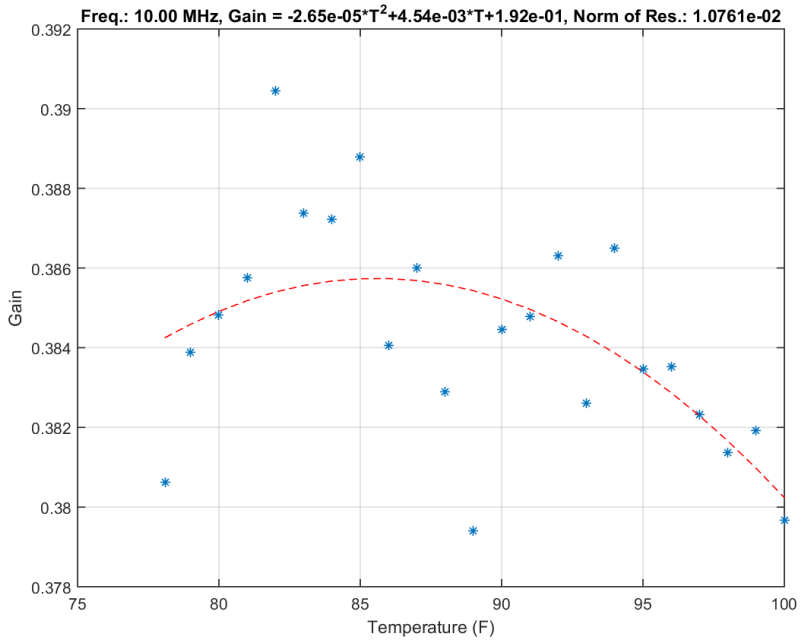

Figure 82. Gain vs. temperature (10 MHz)

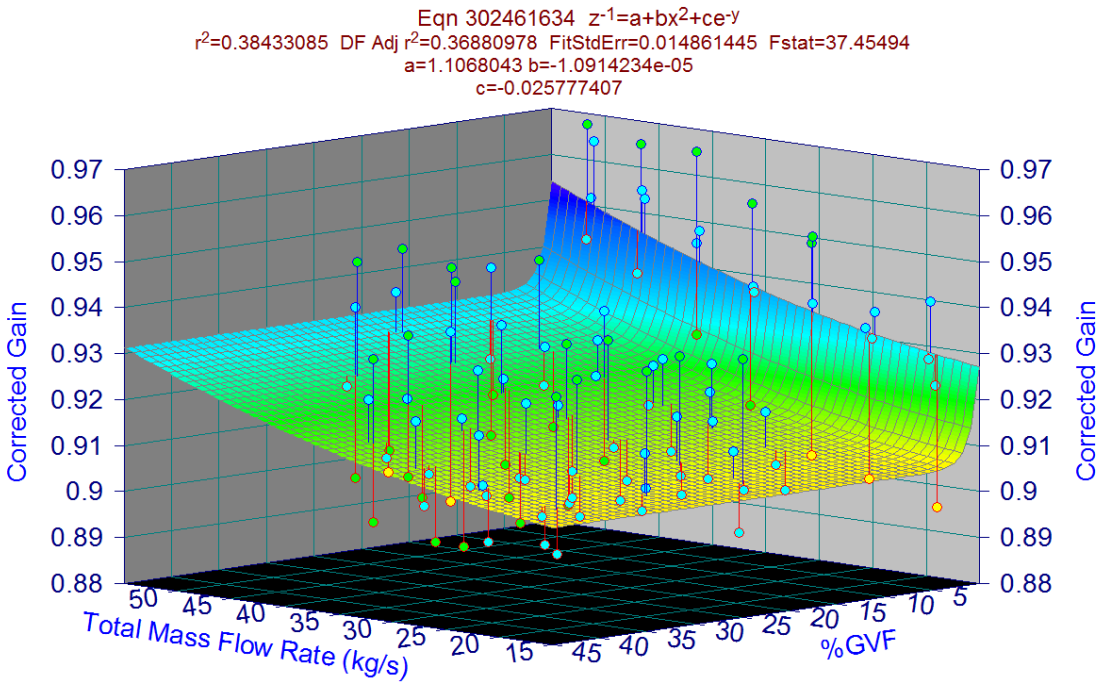

Figure 83. Gain vs. total mass flow rate and % GVF (0.2 MHz)

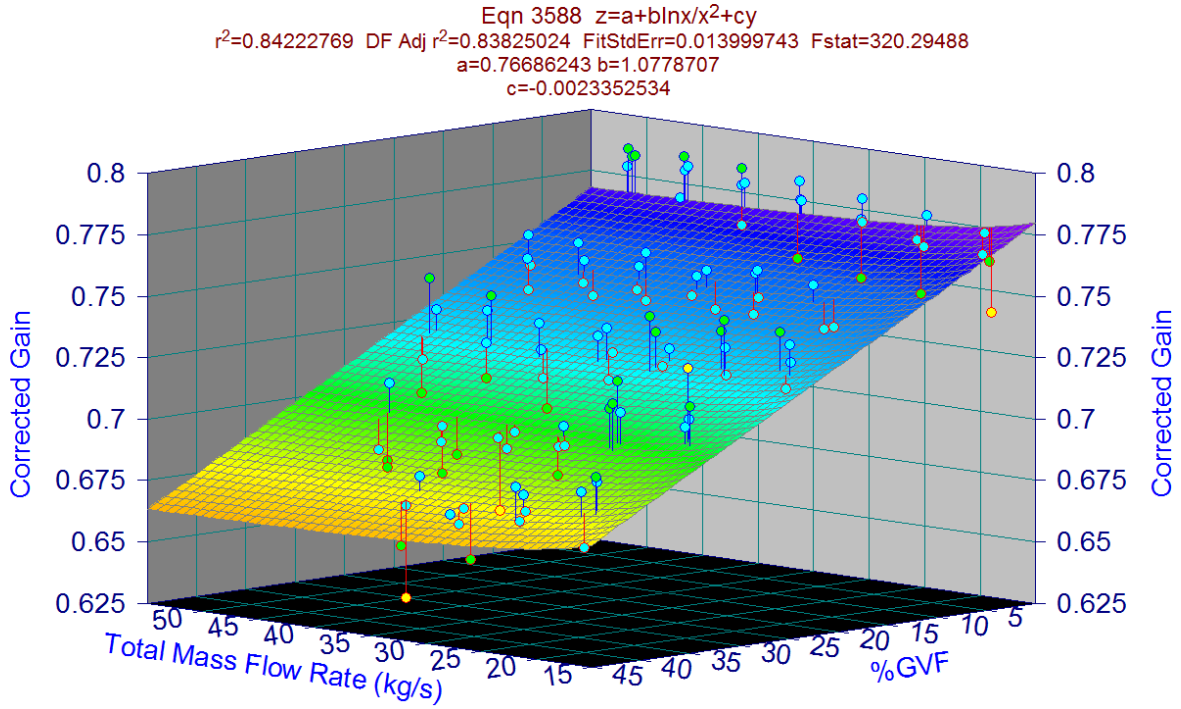

Figure 84. Gain vs. total mass flow rate and % GVF (0.6 MHz)

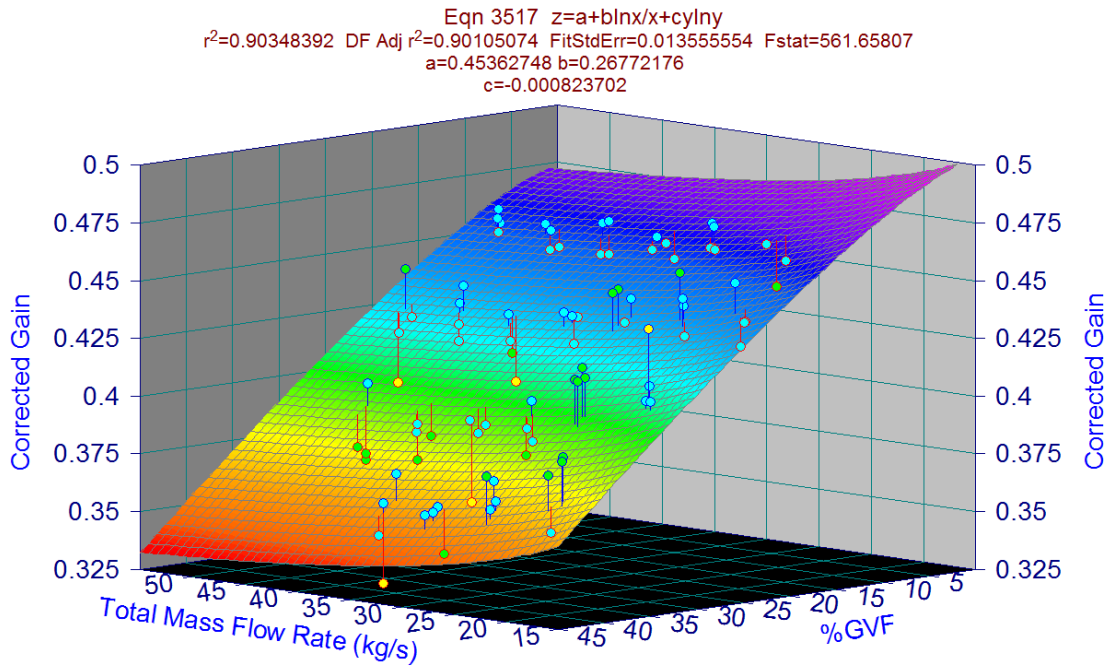

Figure 85. Gain vs. total mass flow rate and % GVF (1.0 MHz)

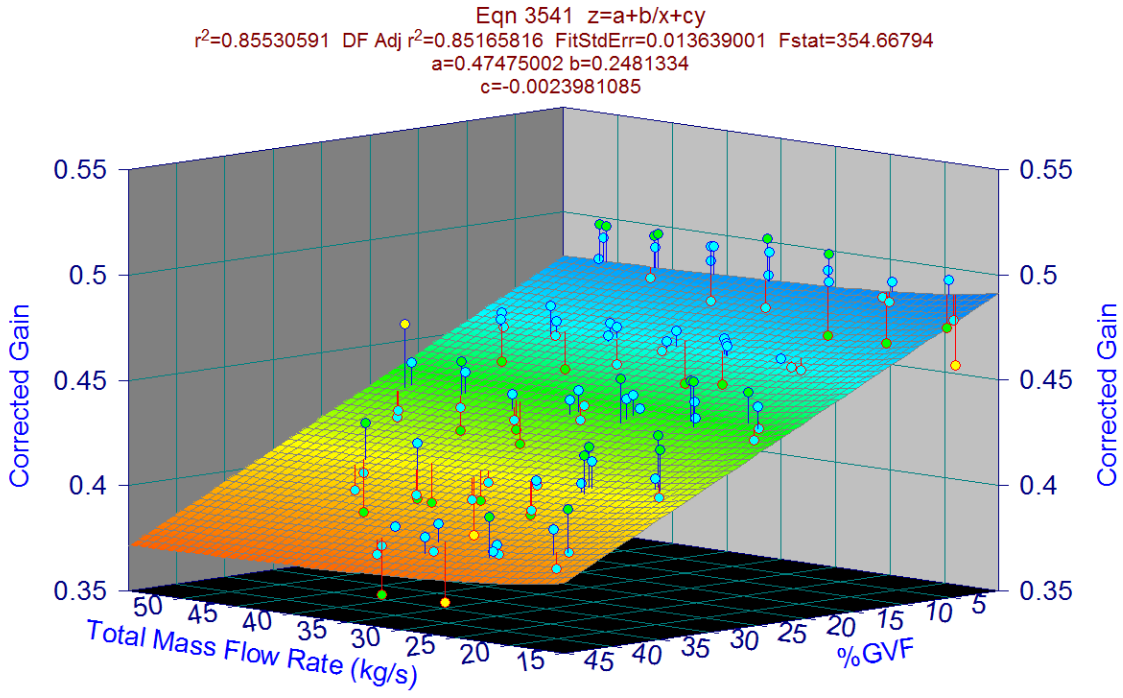

Figure 86. Gain vs. total mass flow rate and % GVF (1.28 MHz)

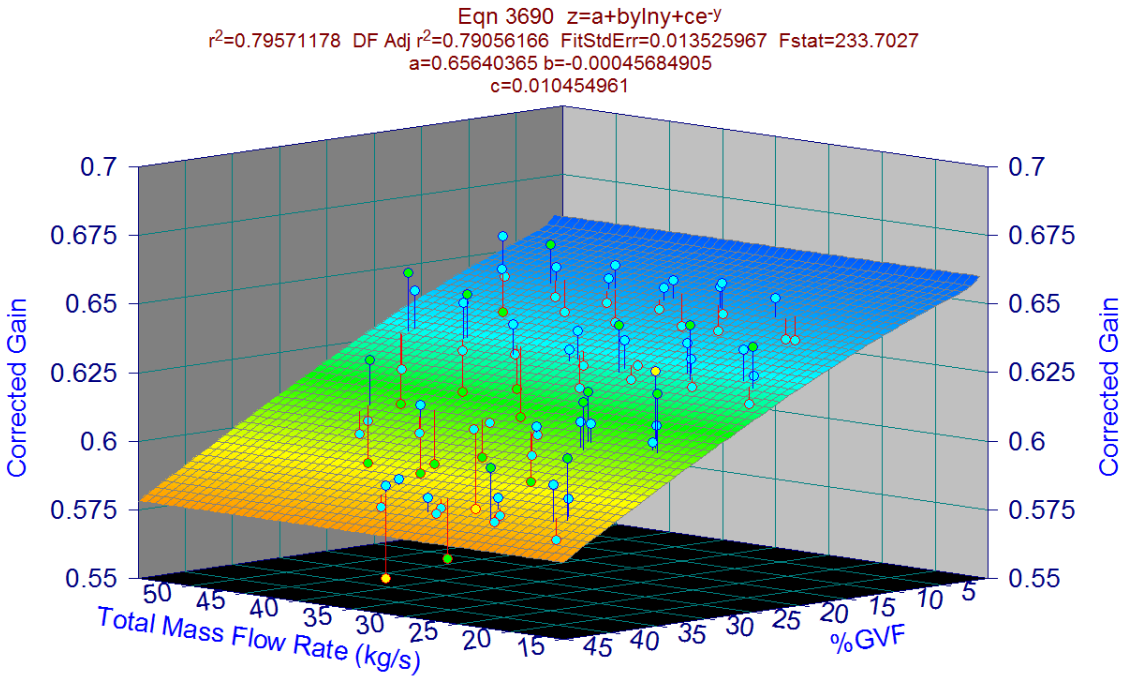

Figure 87. Gain vs. total mass flow rate and % GVF (2.37 MHz)

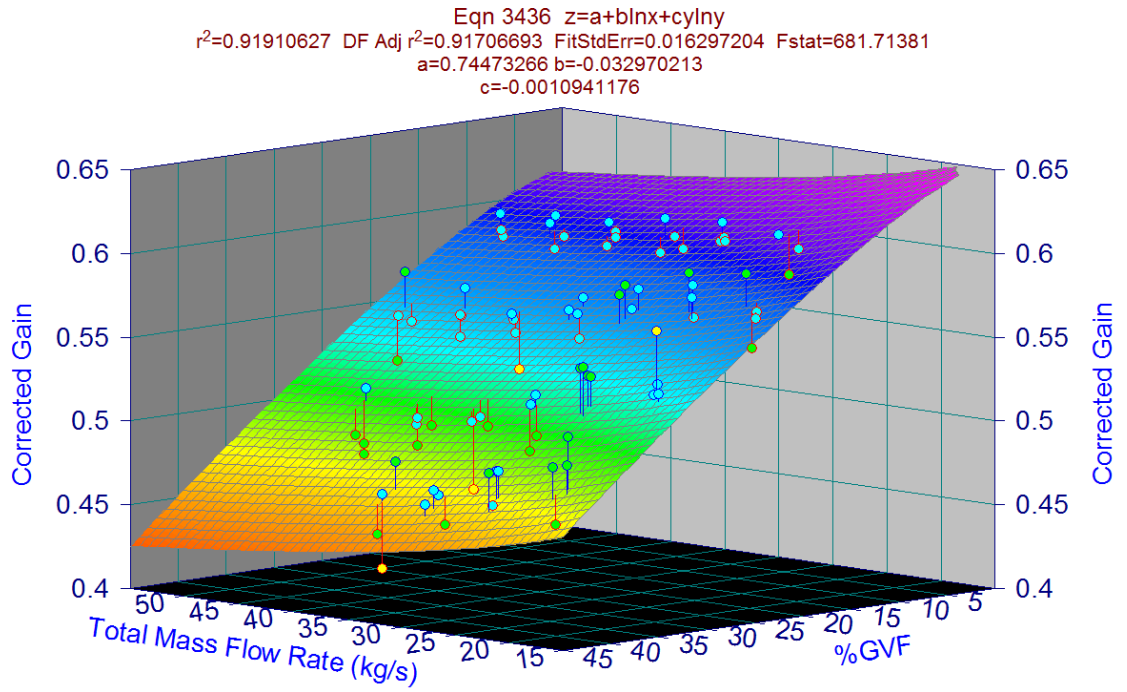

Figure 88. Gain vs. total mass flow rate and % GVF (3.46 MHz)

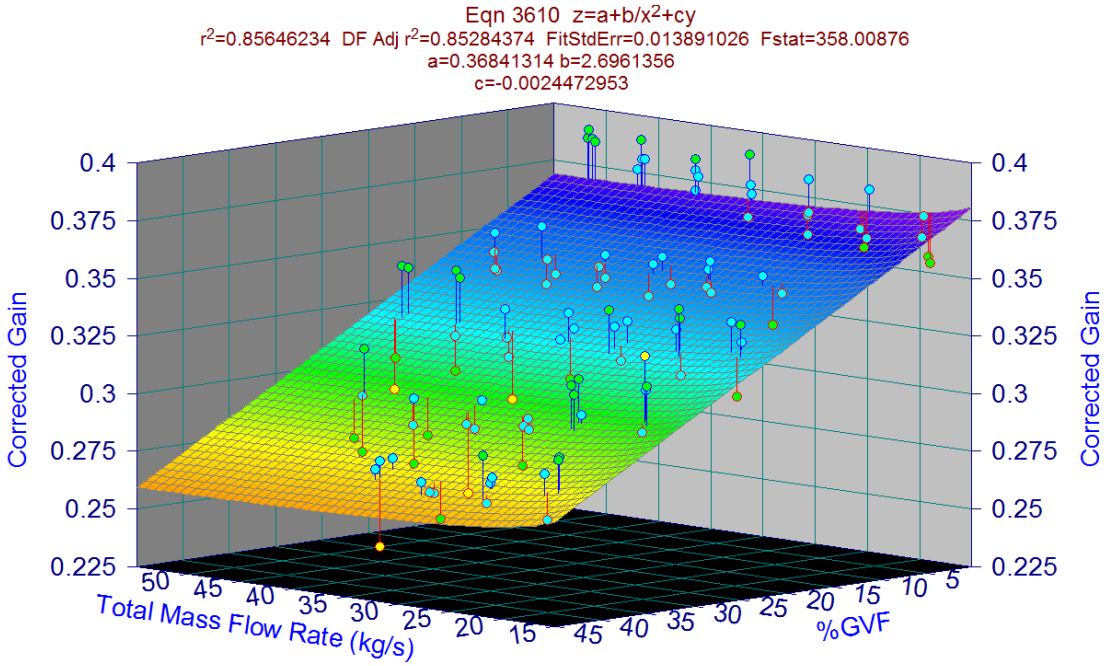

Figure 89. Gain vs. total mass flow rate and % GVF (4.55 MHz)

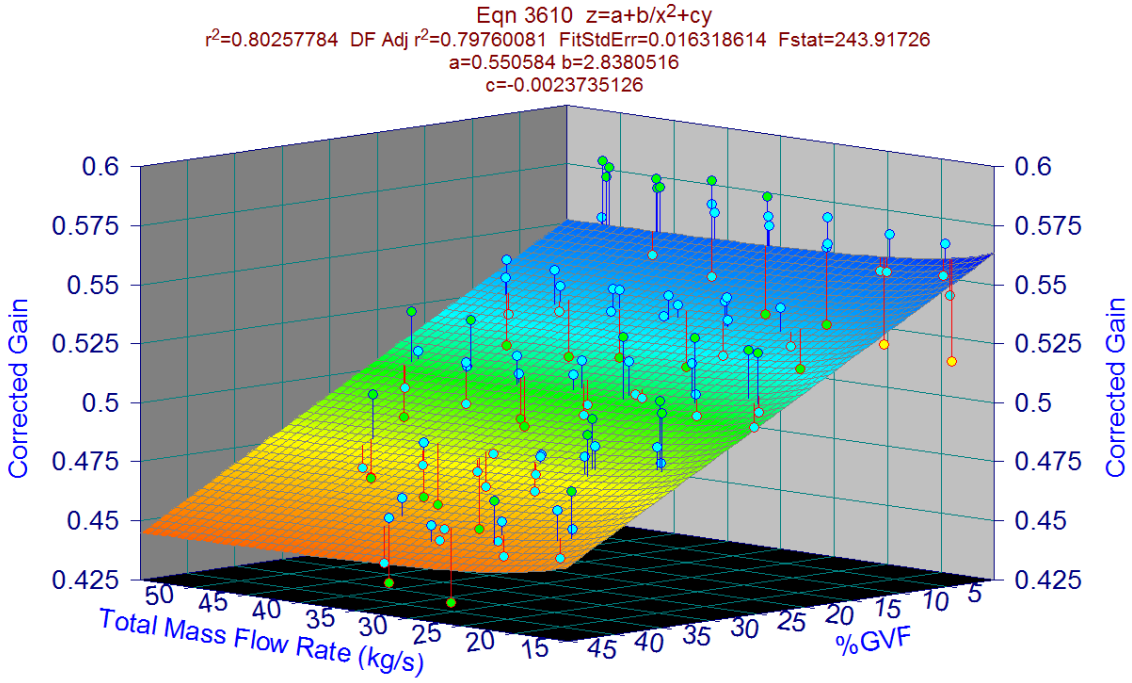

Figure 90. Gain vs. total mass flow rate and % GVF (5.64 MHz)

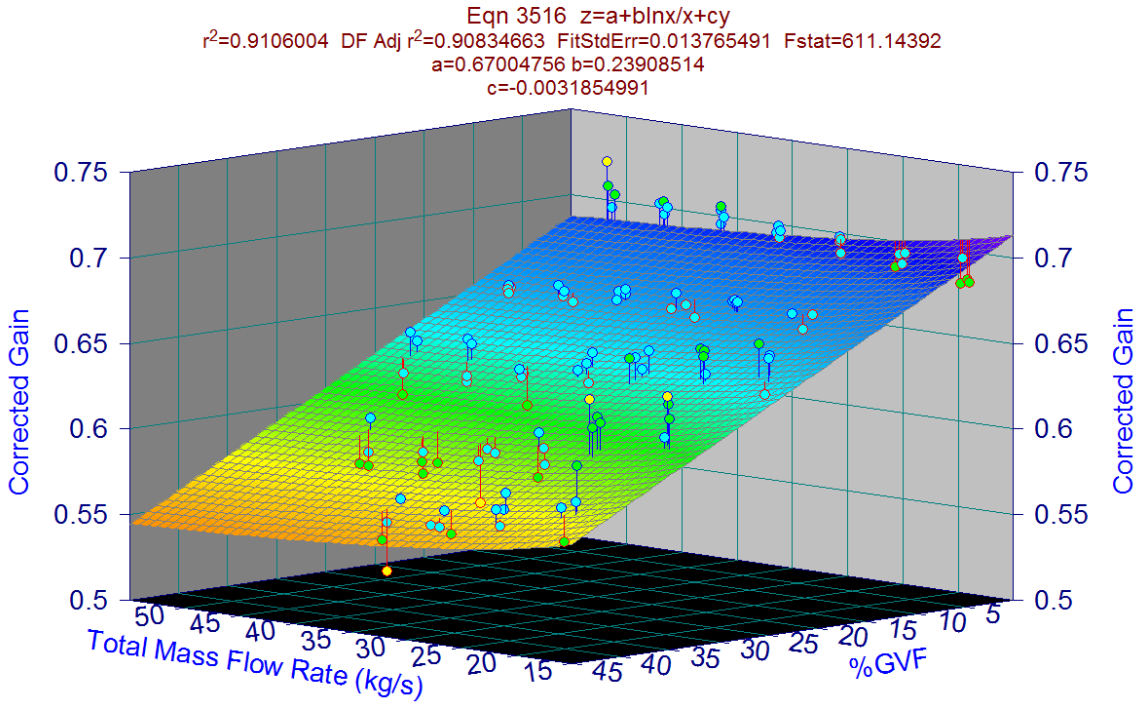

Figure 91. Gain vs. total mass flow rate and % GVF (6.73 MHz)

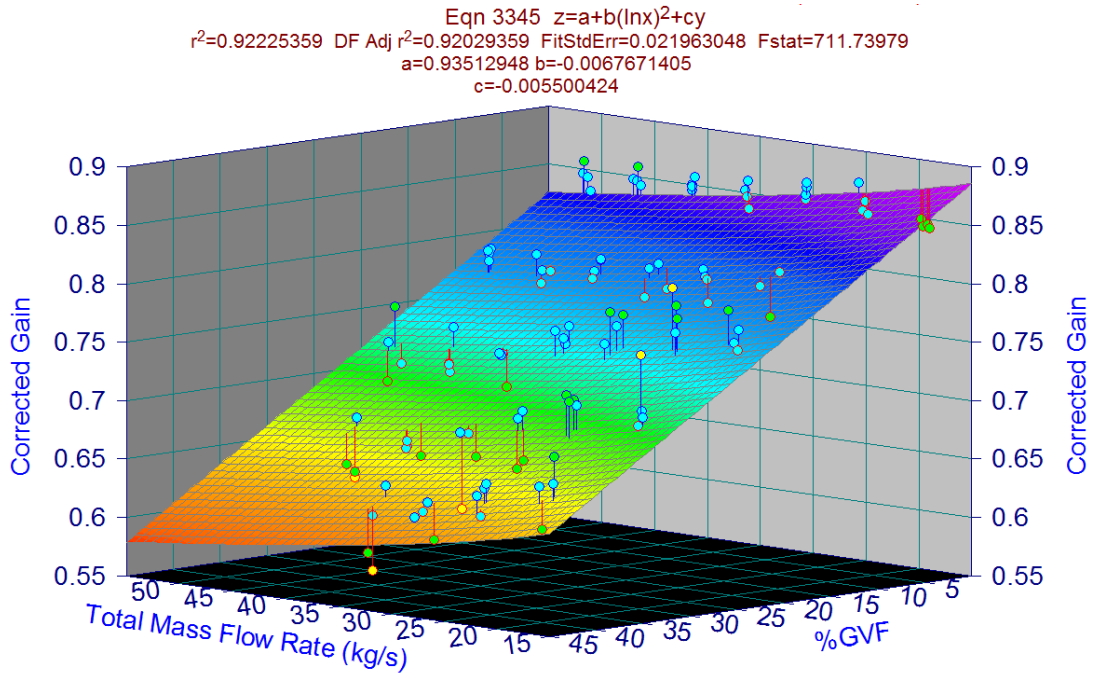

Figure 92. Gain vs. total mass flow rate and % GVF (7.82 MHz)

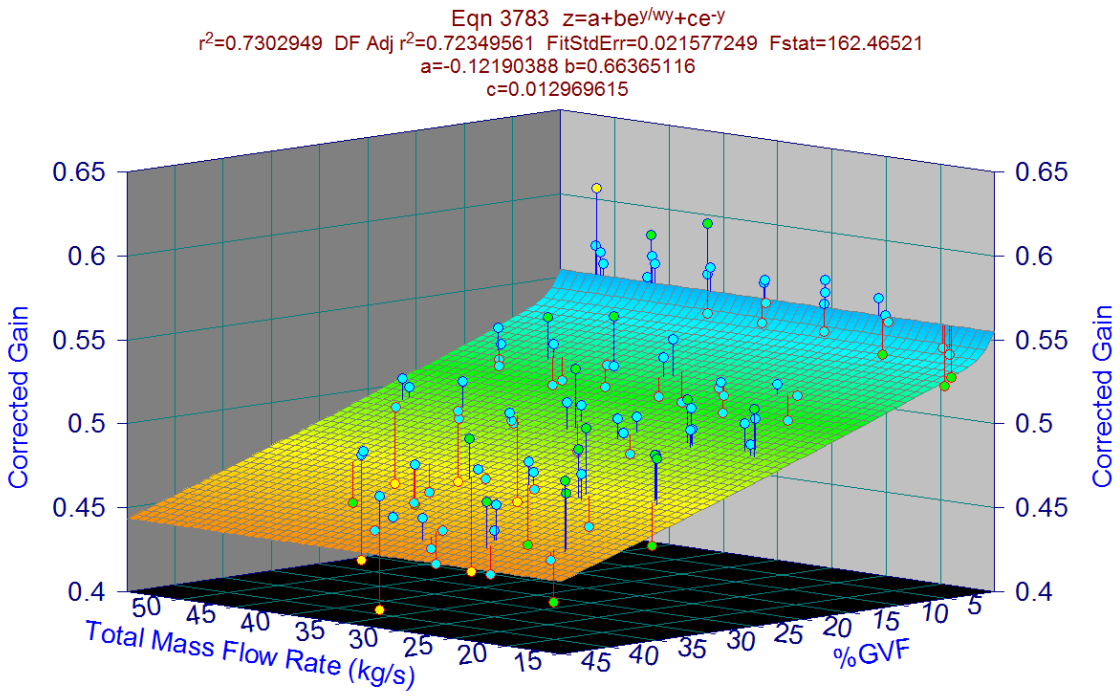

Figure 93. Gain vs. total mass flow rate and % GVF (8.91 MHz)

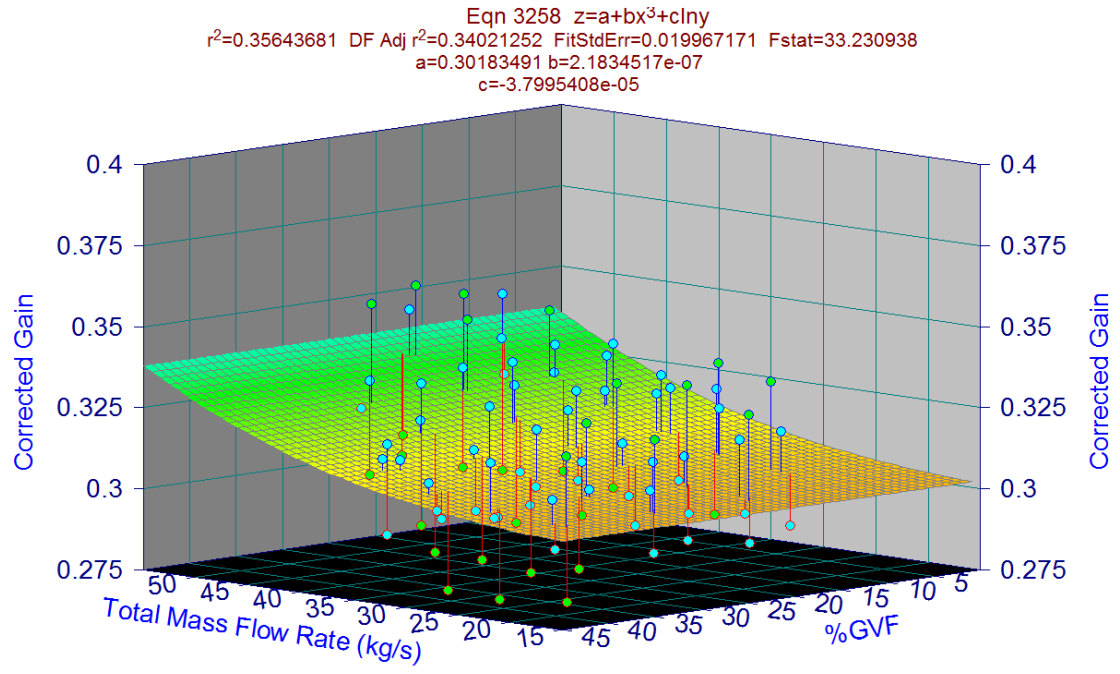

Figure 94. Gain vs. total mass flow rate and % GVF (10 MHz)

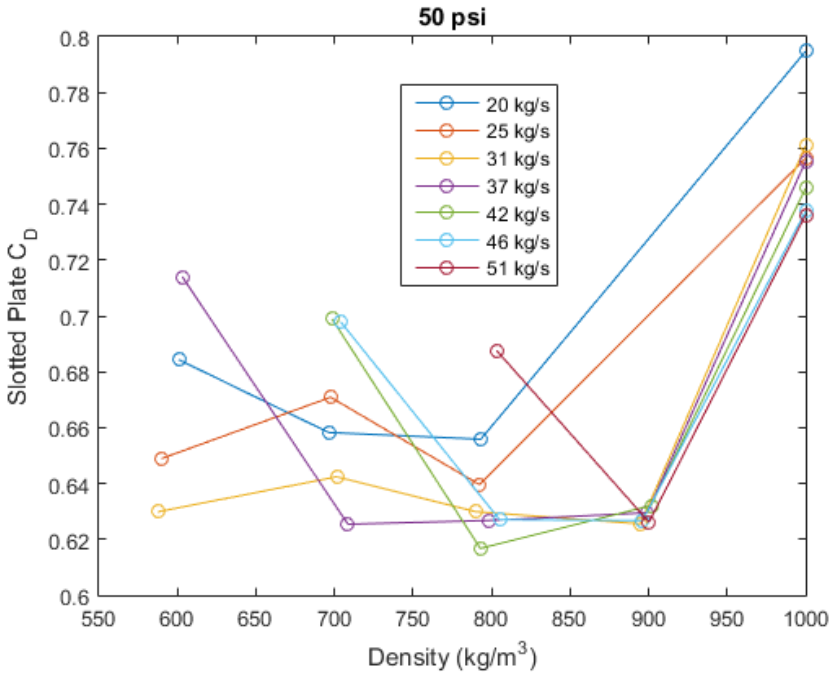

Figure 95. Slotted plate C_D vs. density and mass flow rate at 50 psig

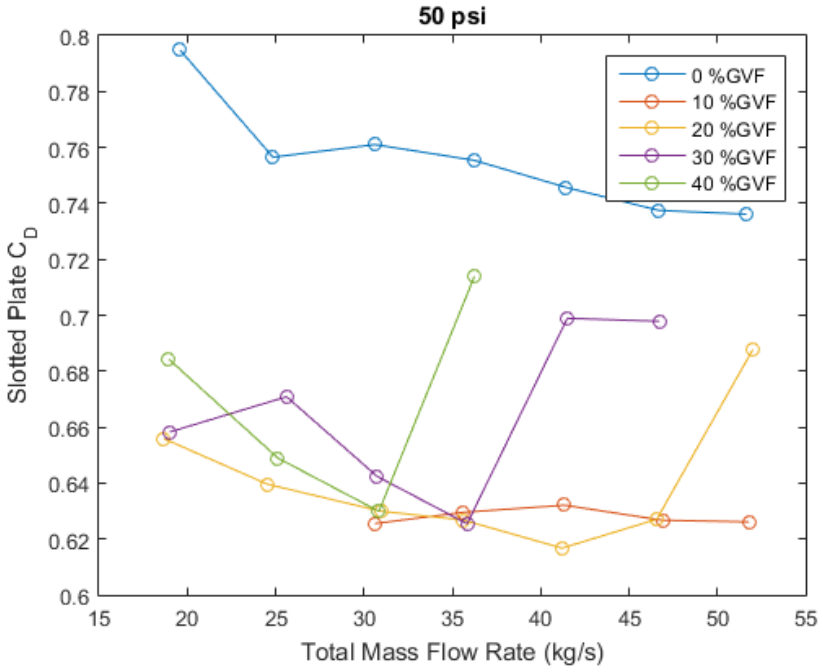

Figure 96. Slotted plate C_D vs. mass flow rate and density at 50 psig

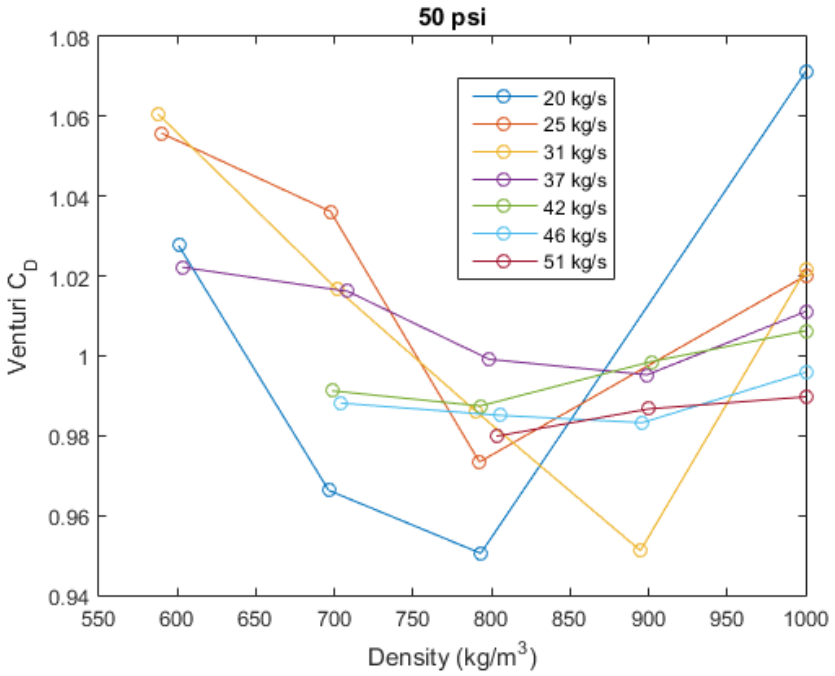

Figure 97. Venturi C_D vs. density and mass flow rate at 50 psig

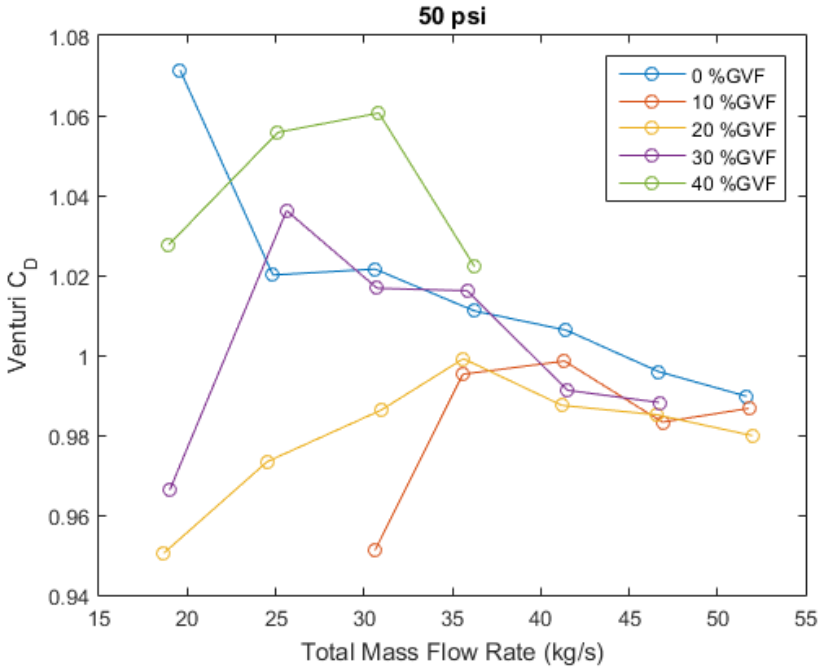

Figure 98. Venturi C_D vs. mass flow rate and density at 50 psig

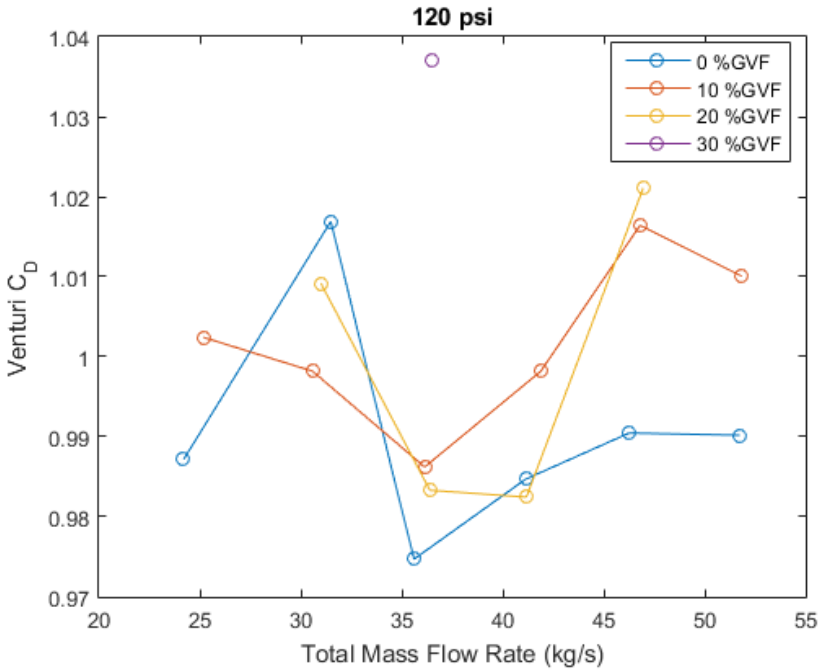

Figure 99. Venturi C_D vs. mass flow rate and density at 120 psig

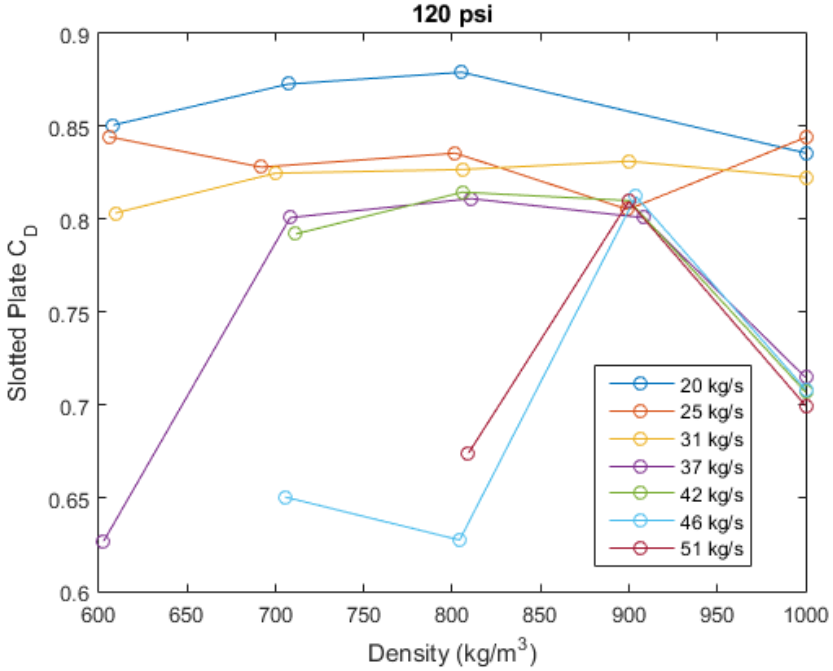

Figure 100. Slotted plate C_D vs. density and mass flow rate at 120 psig

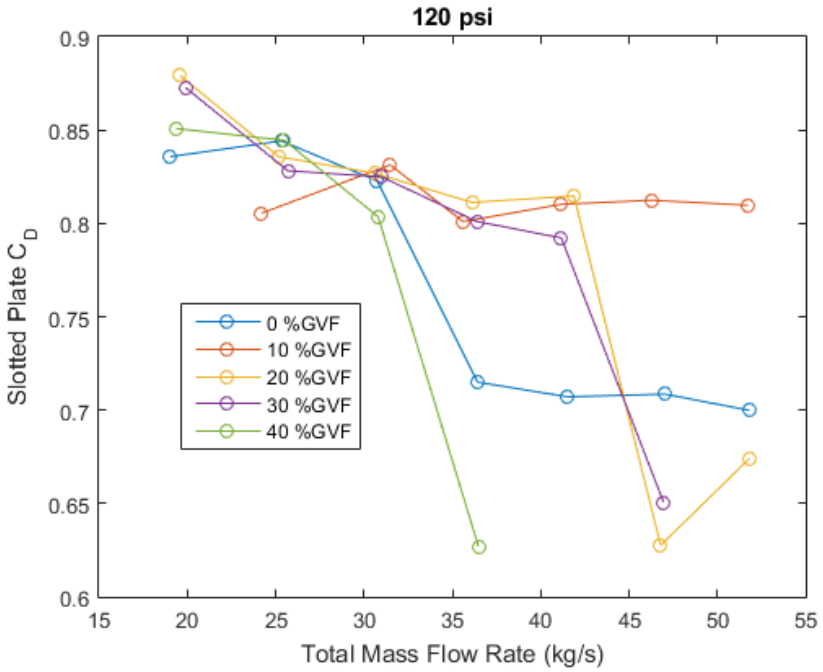

Figure 101. Slotted plate C_D vs. mass flow rate and density at 120 psig

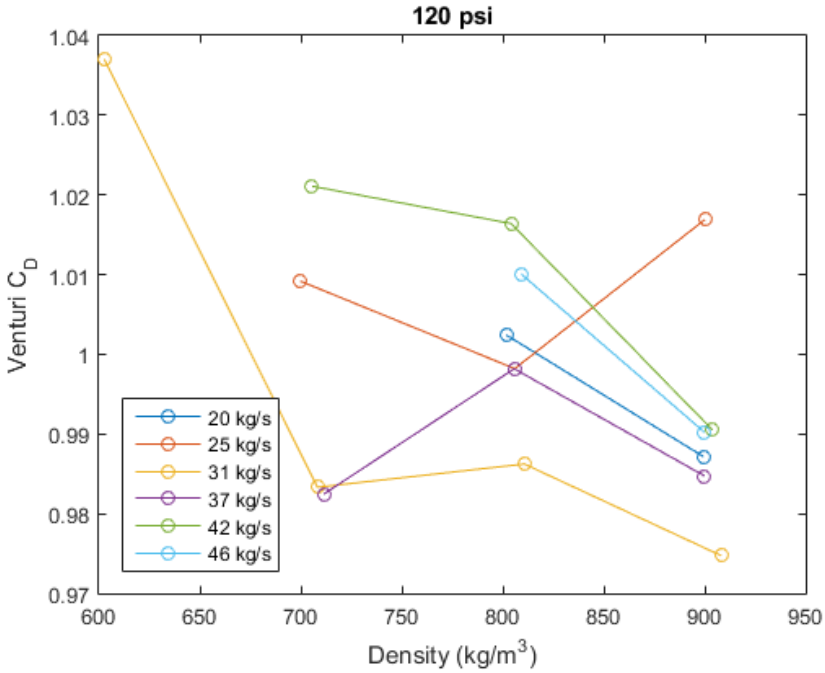

Figure 102. Venturi C_D vs. density and mass flow rate at 120 psig

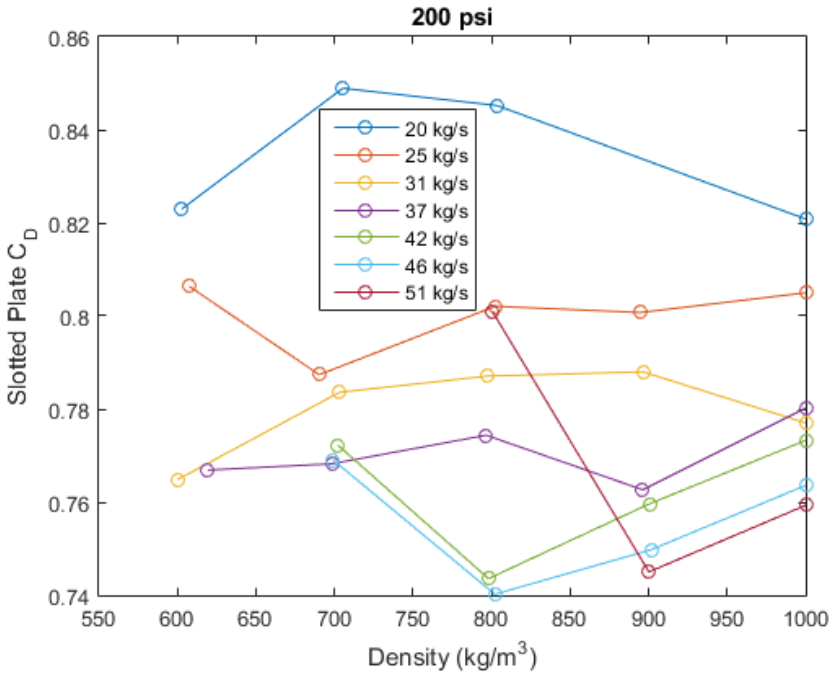

Figure 103. Slotted plate C_D vs. density and mass flow rate at 200 psig

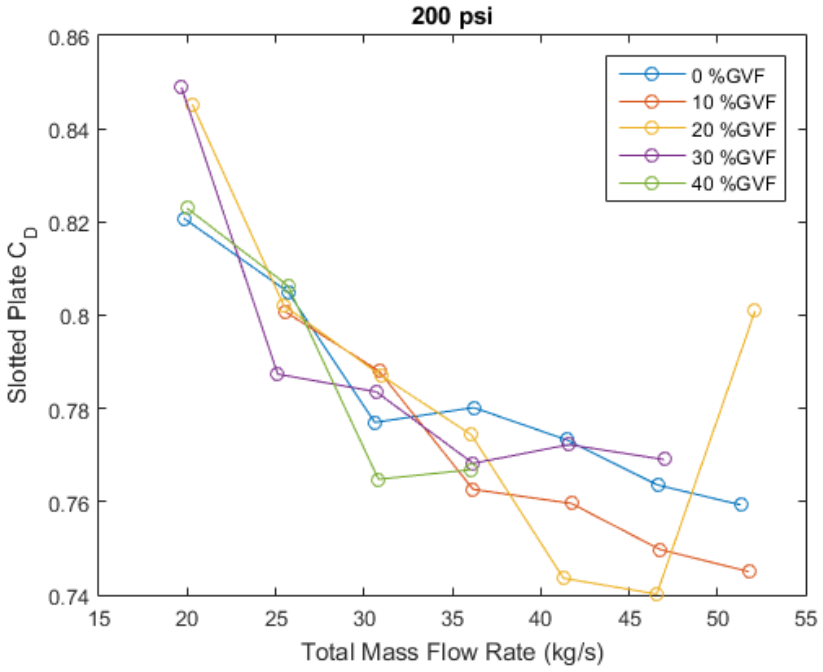

Figure 104. Slotted plate C_D vs. mass flow rate and density at 200 psig

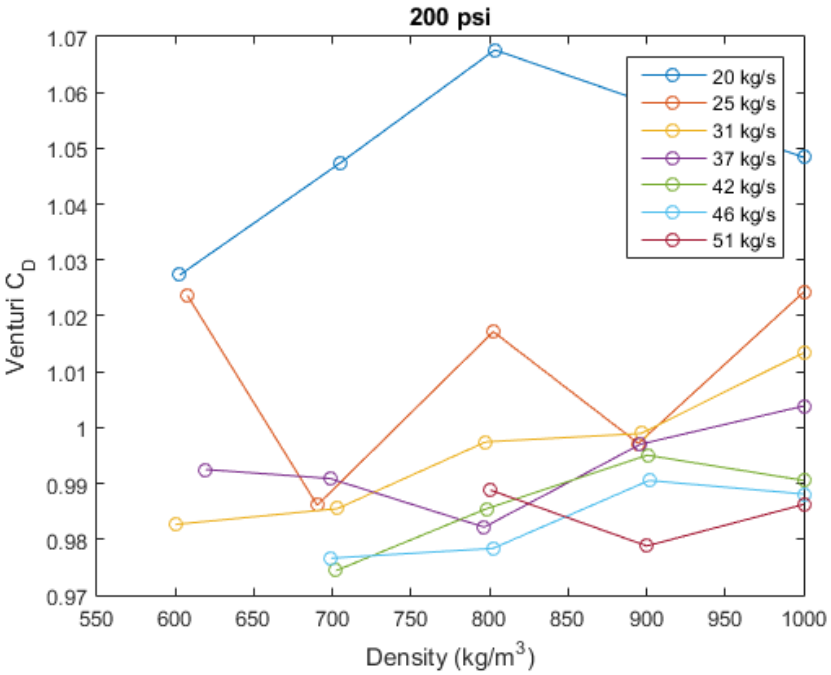

Figure 105. Venturi C_D vs. density and mass flow rate at 200 psig

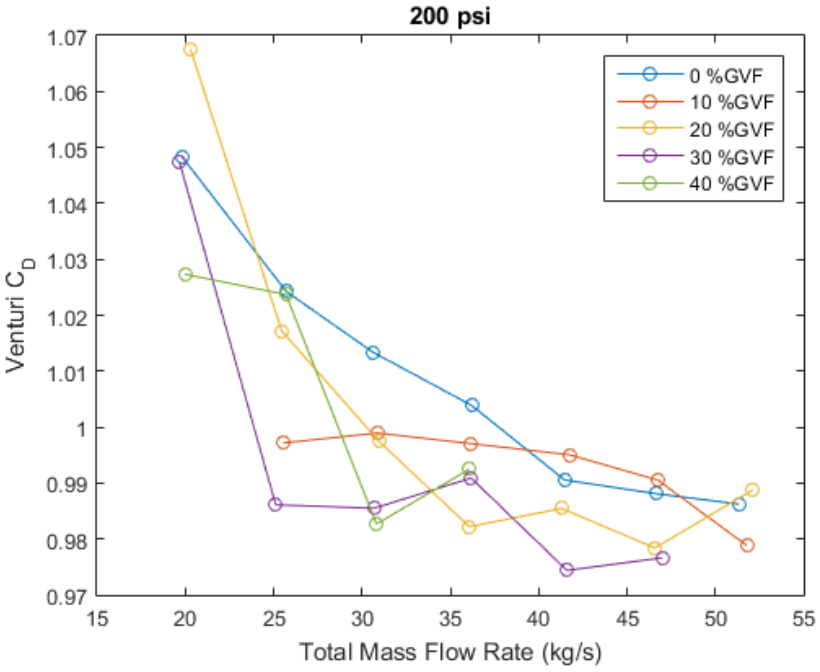

Figure 106. Venturi C_D vs. mass flow rate and density at 200 psig

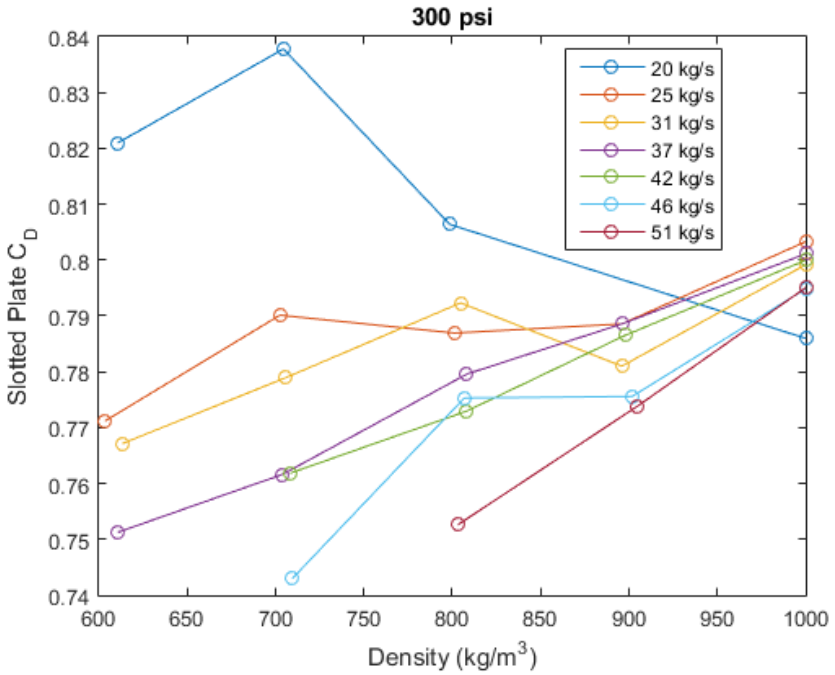

Figure 107. Slotted plate C_D vs. density and mass flow rate at 300 psig

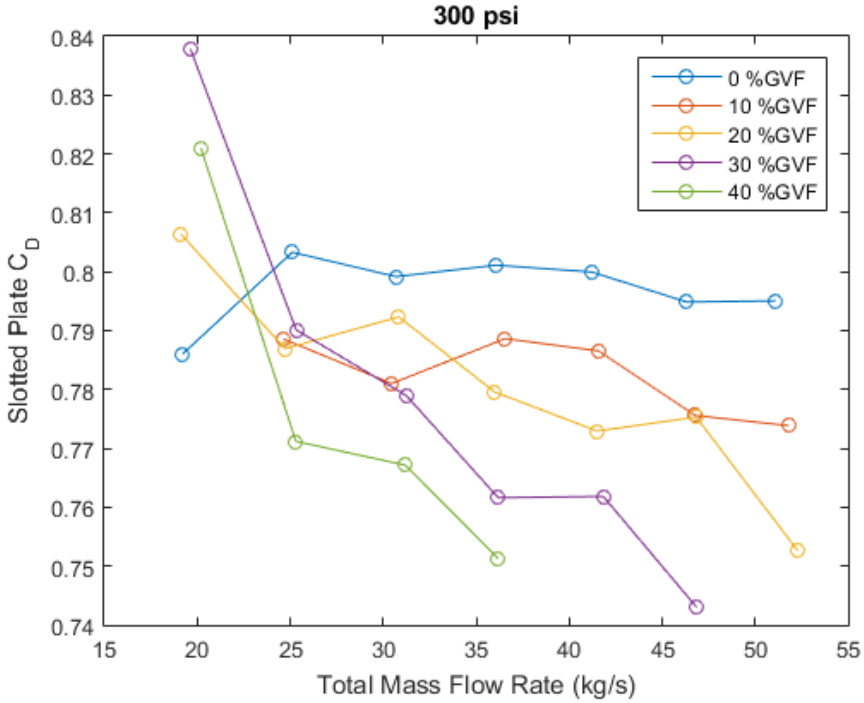

Figure 108. Slotted plate C_D vs. mass flow rate and density at 300 psig

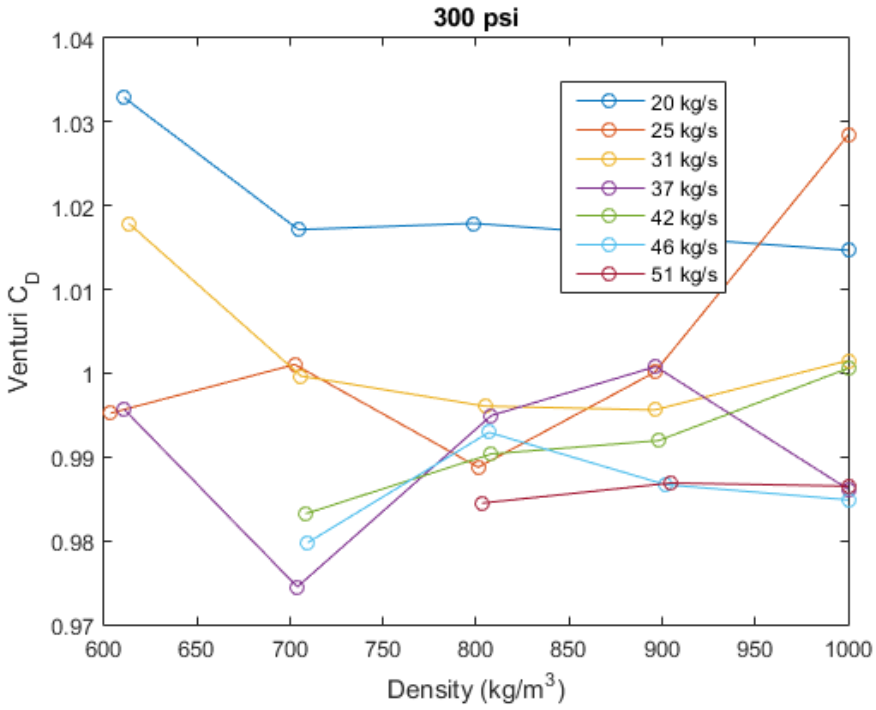

Figure 109. Venturi C_D vs. density and mass flow rate at 300 psig

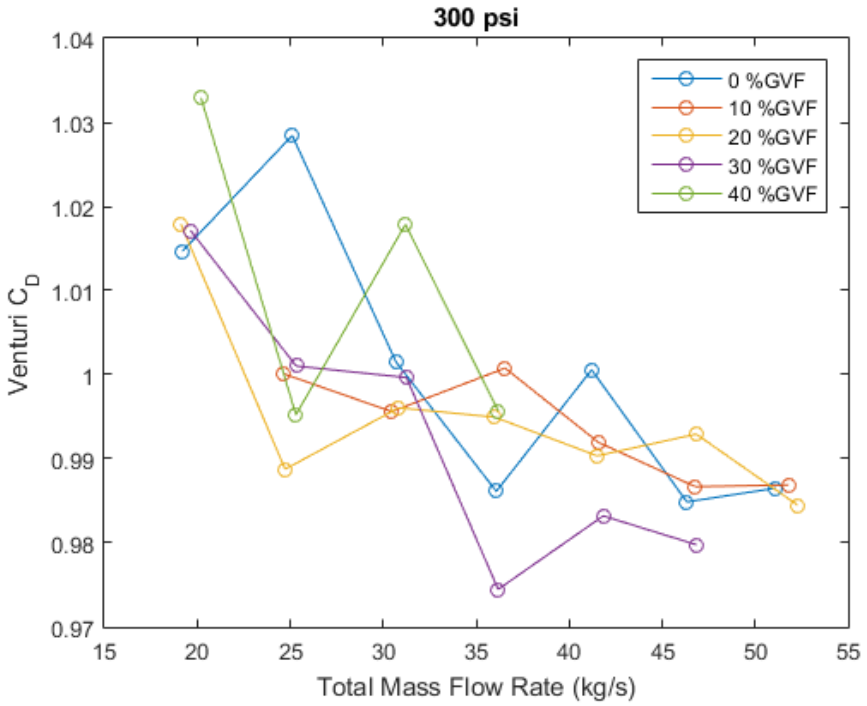

Figure 110. Venturi C_D vs. mass flow rate and density at 300 psig

APPENDIX B DRAWINGS

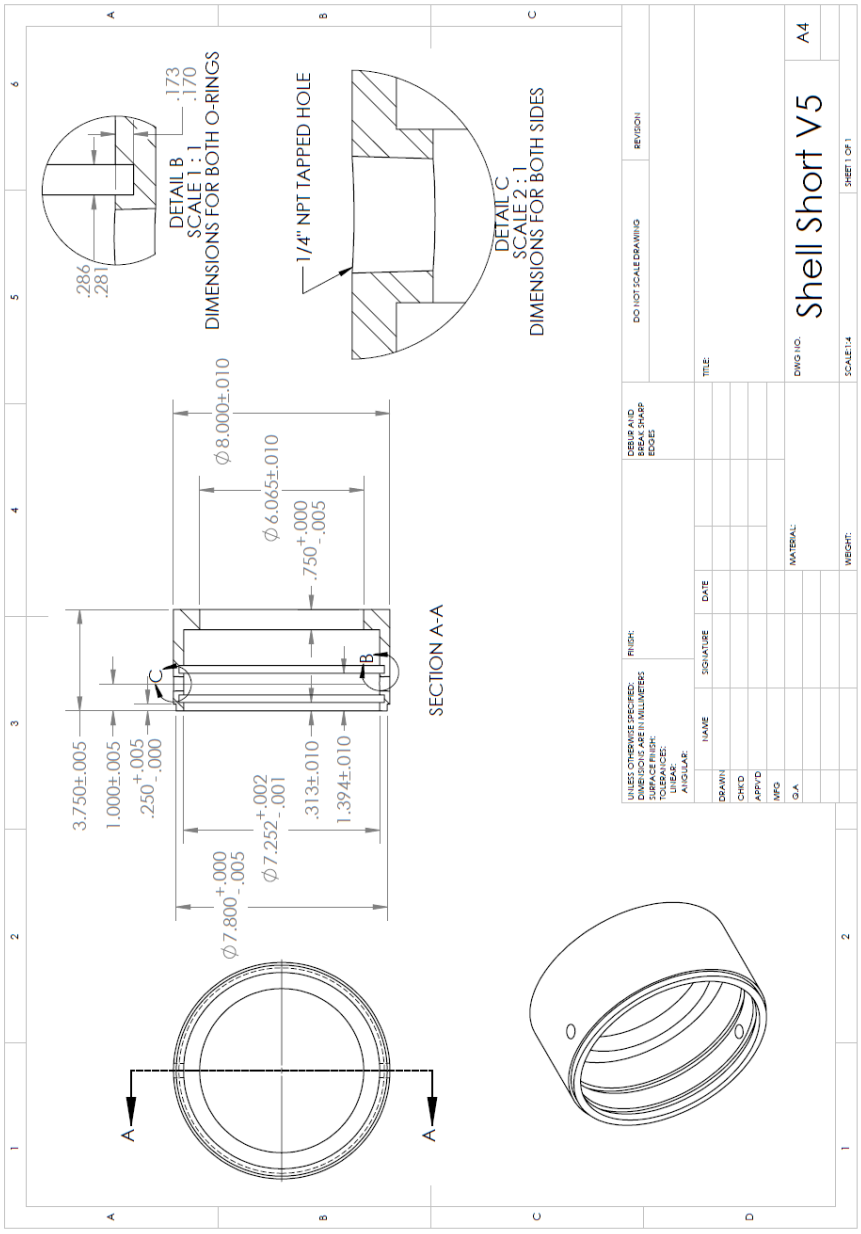

Figure 111. Drawing of short shell piece

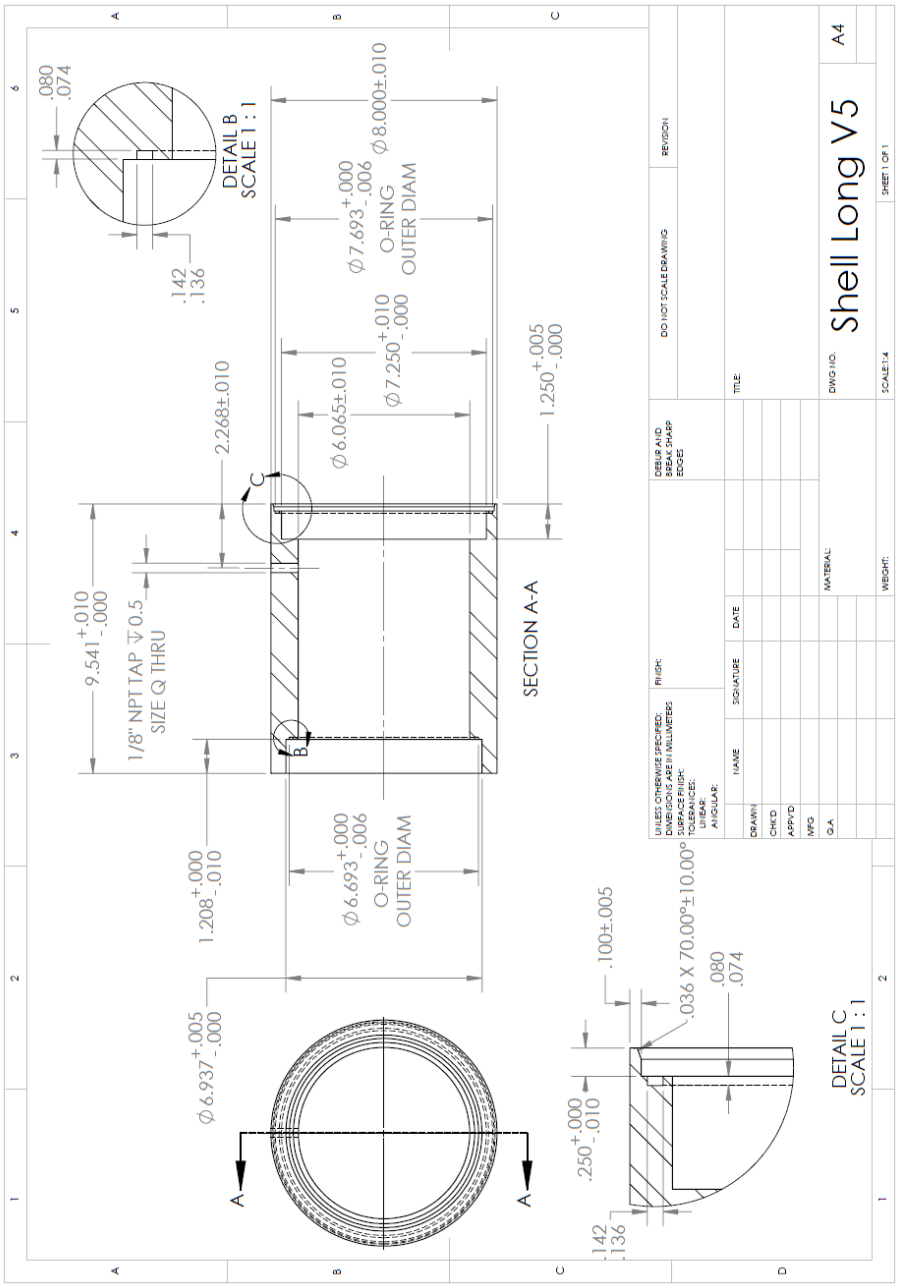

Figure 112. Drawing of long shell piece

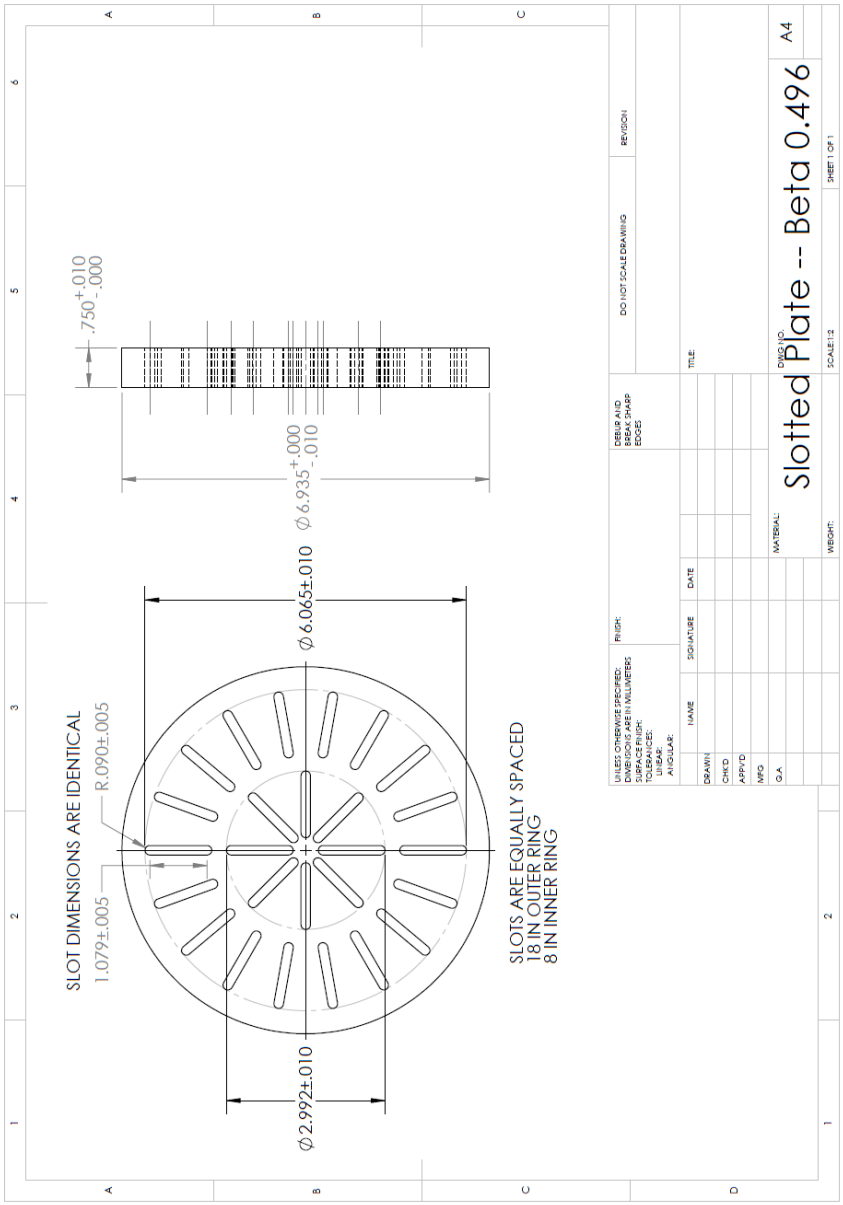

Figure 113. Drawing of slotted plate

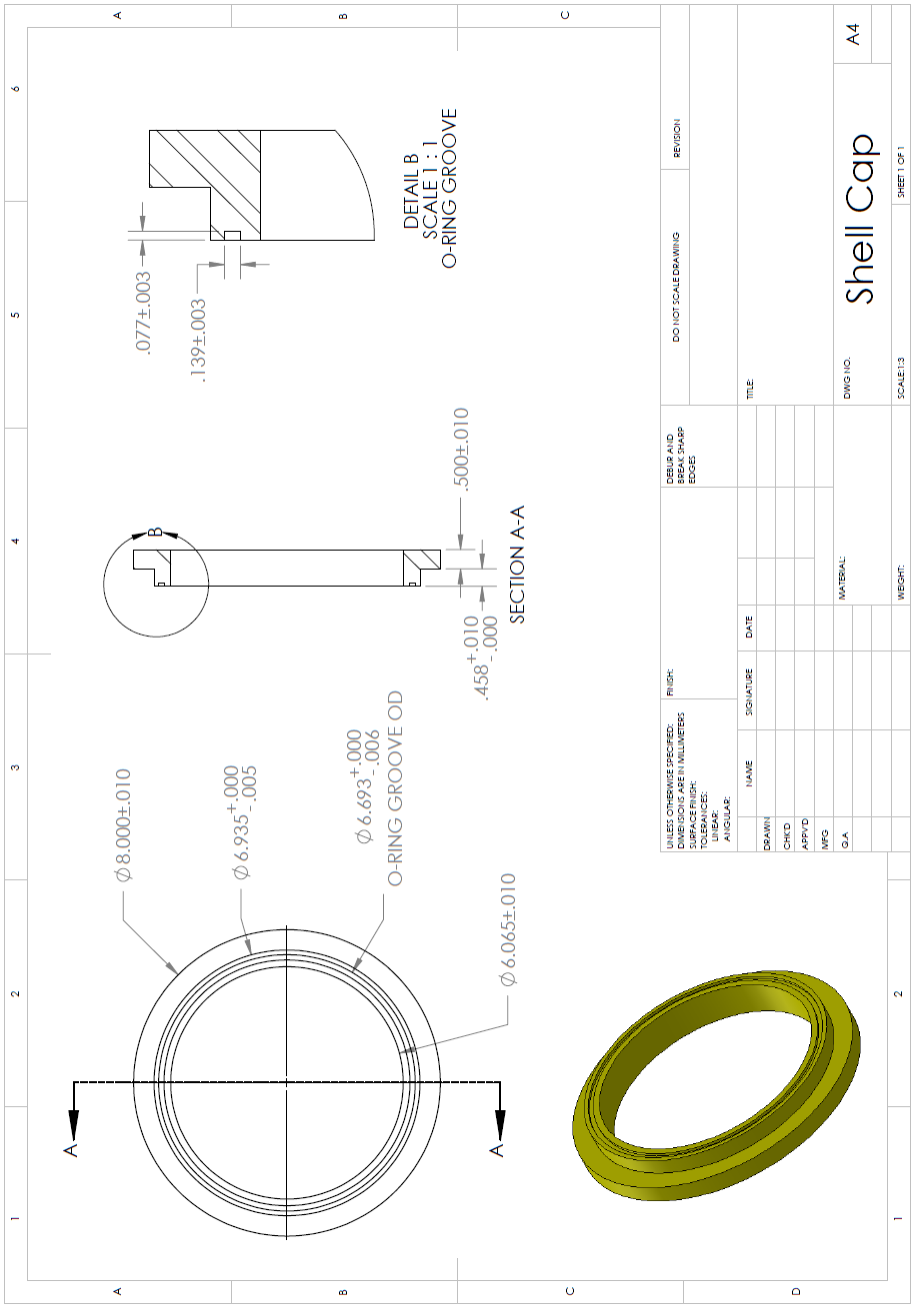

Figure 114. Drawing of shell cap piece

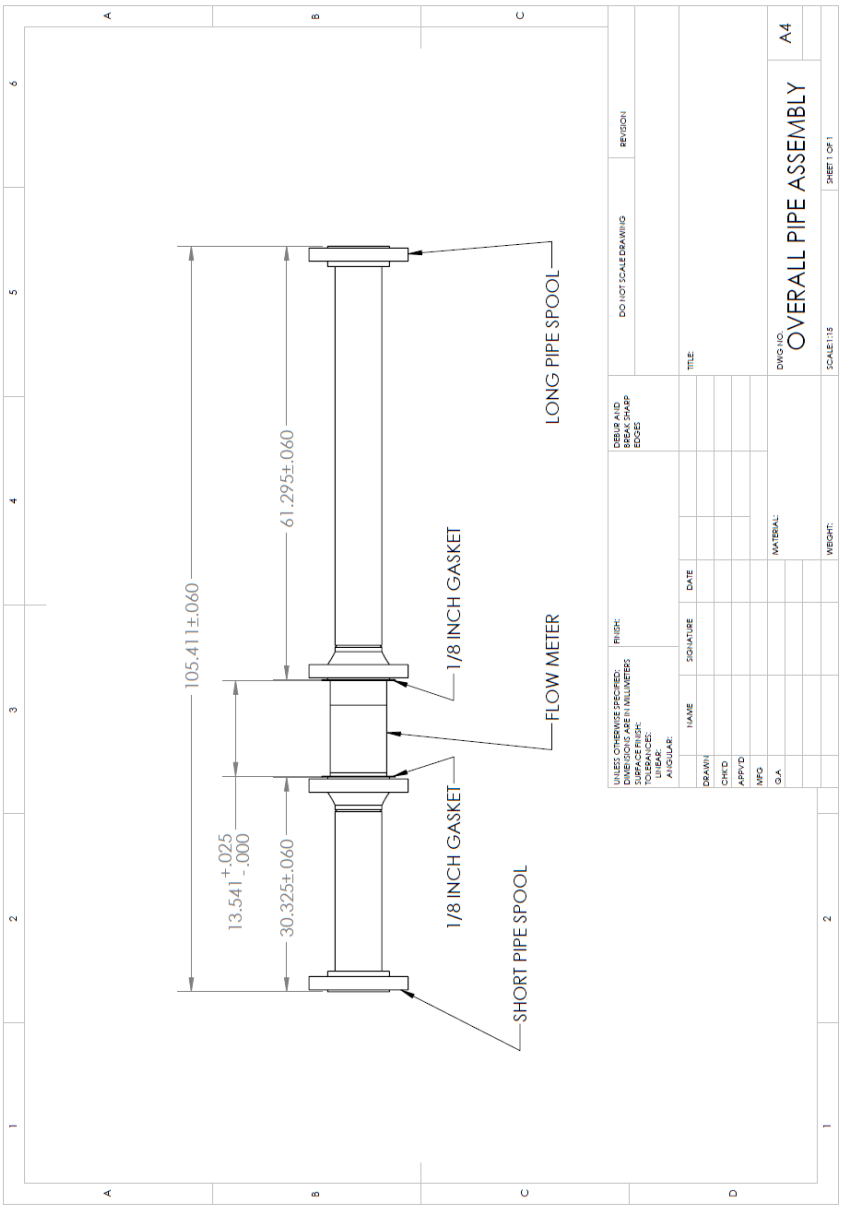

Figure 115. Drawing of pipe assembly with MPFM

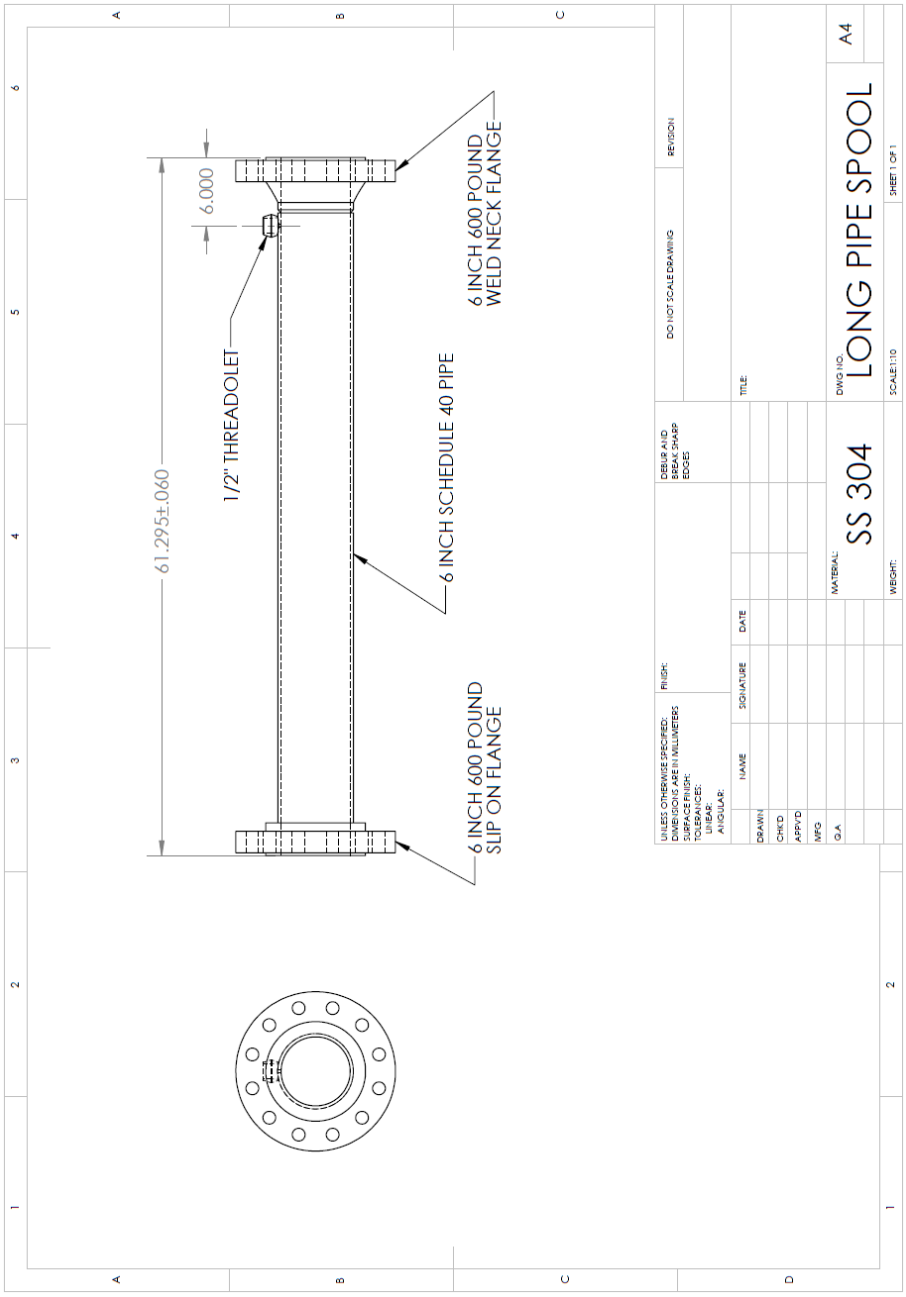

Figure 116. Drawing of long pipe spool

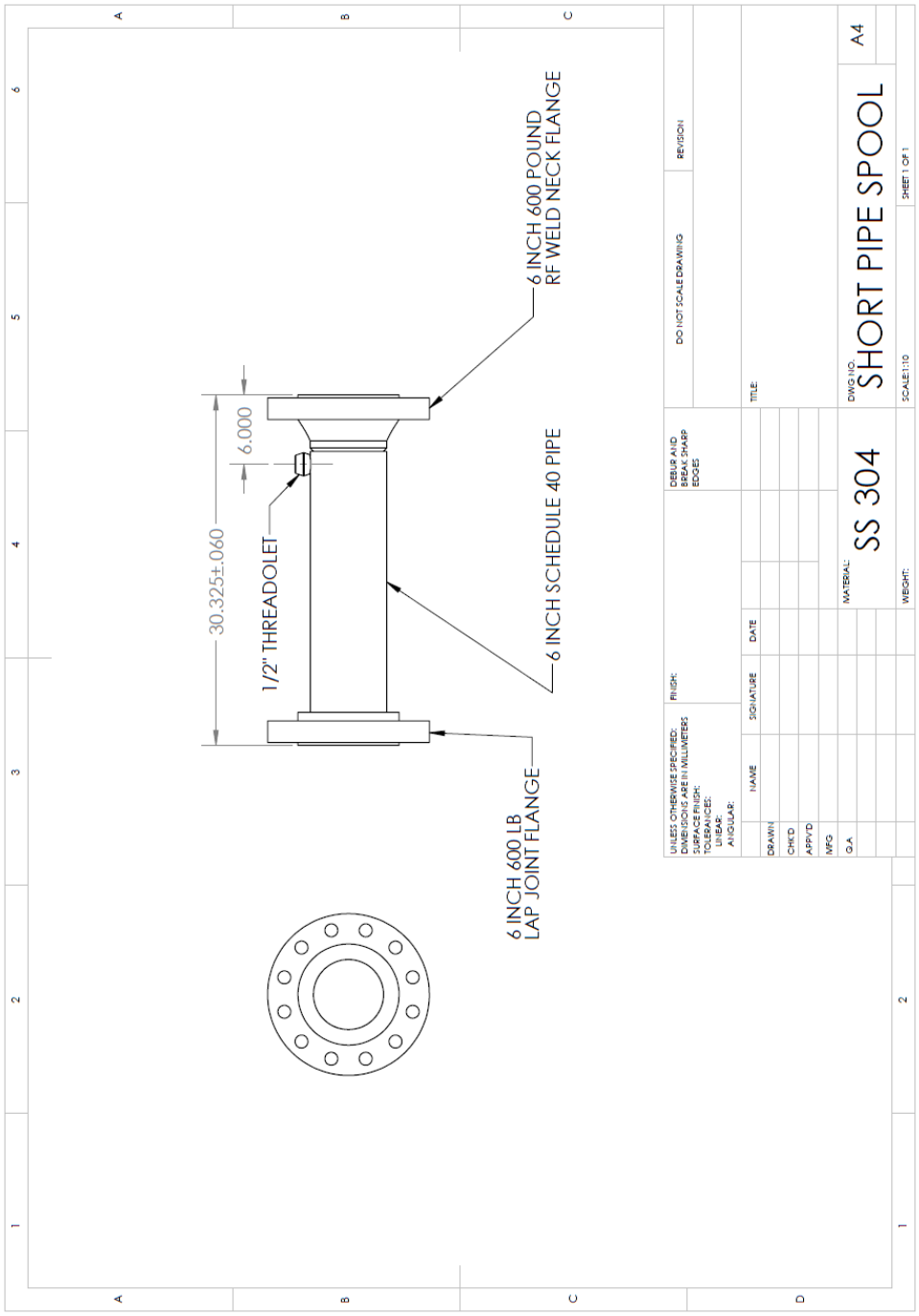

Figure 117. Drawing of short pipe spool

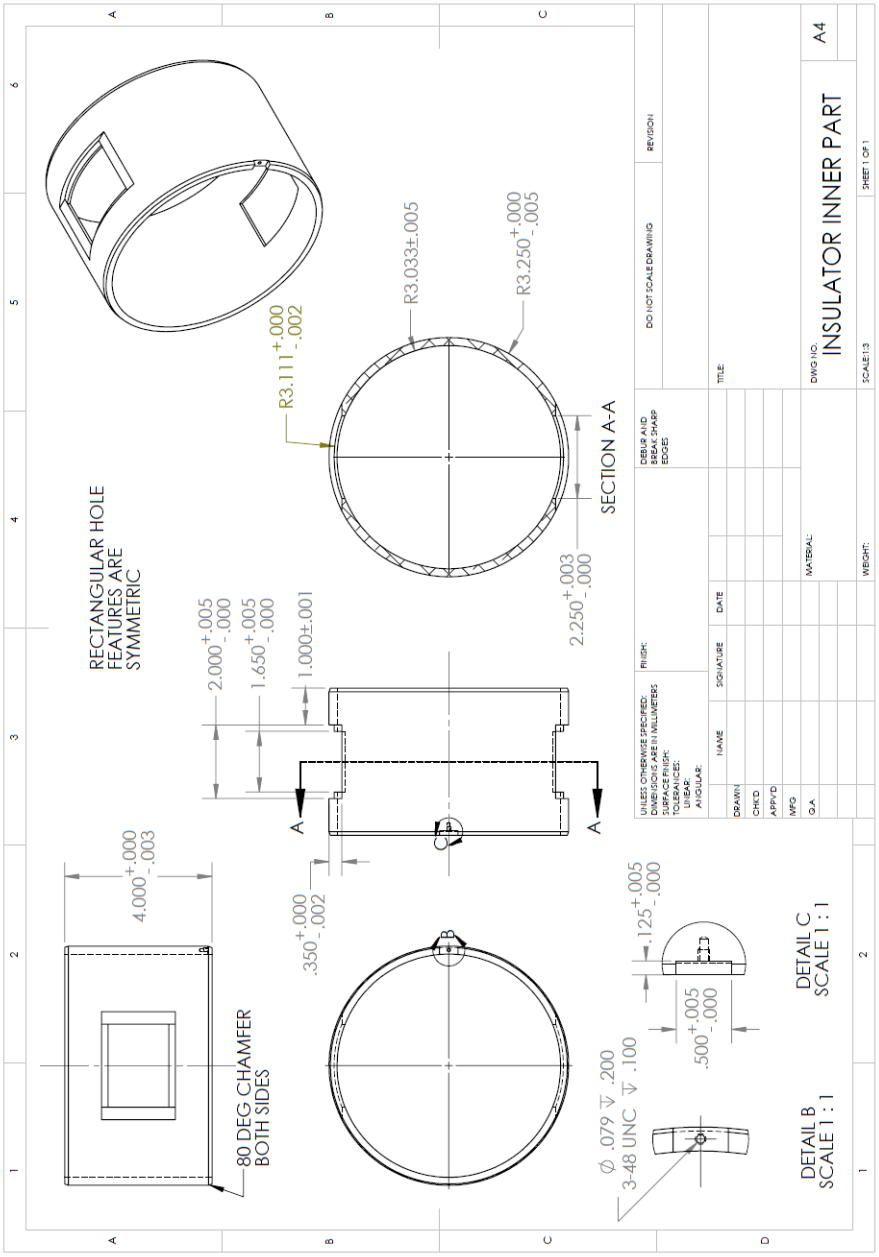

Figure 118. Drawing of inner alumina ring

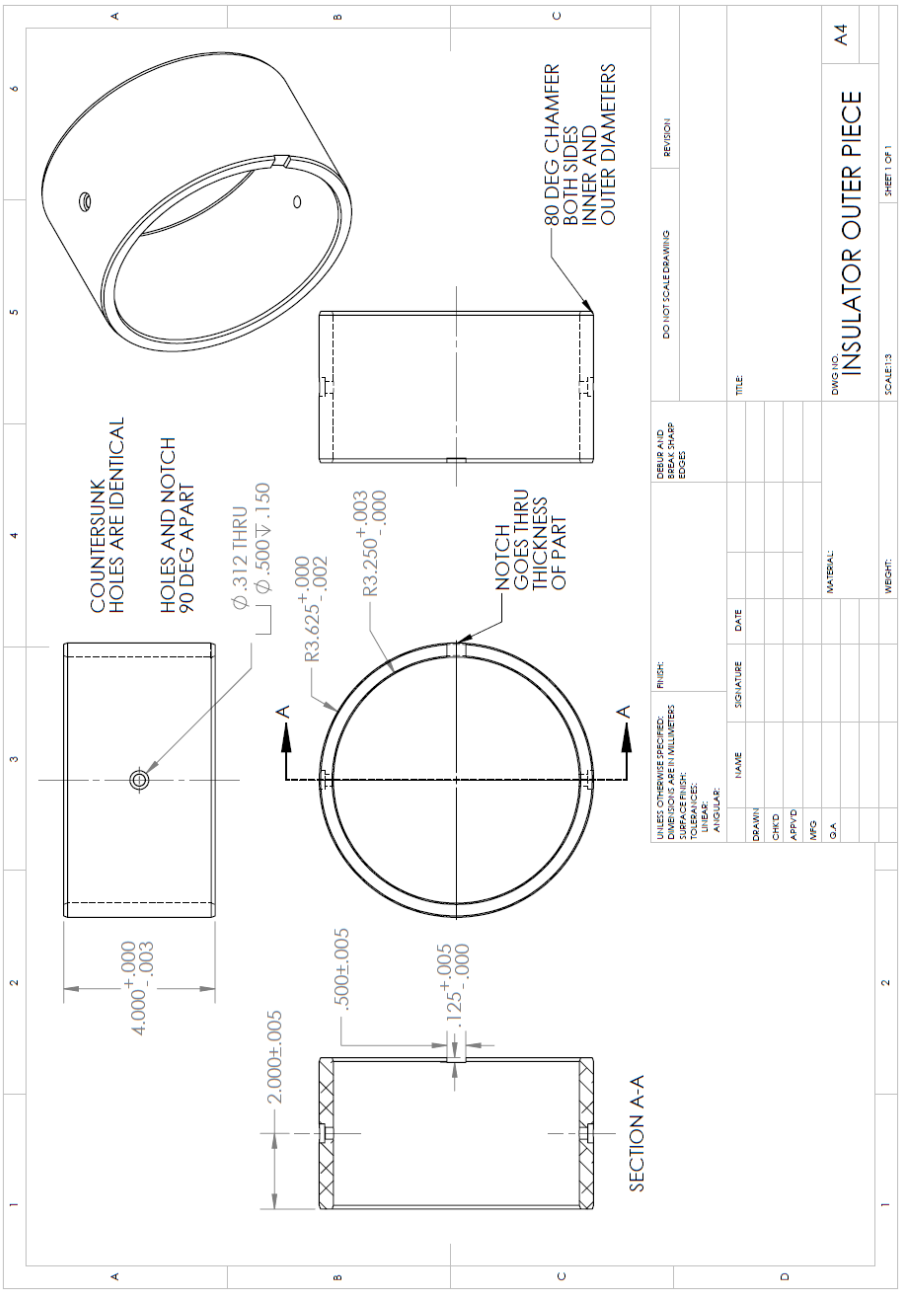

Figure 119. Drawing of outer alumina ring

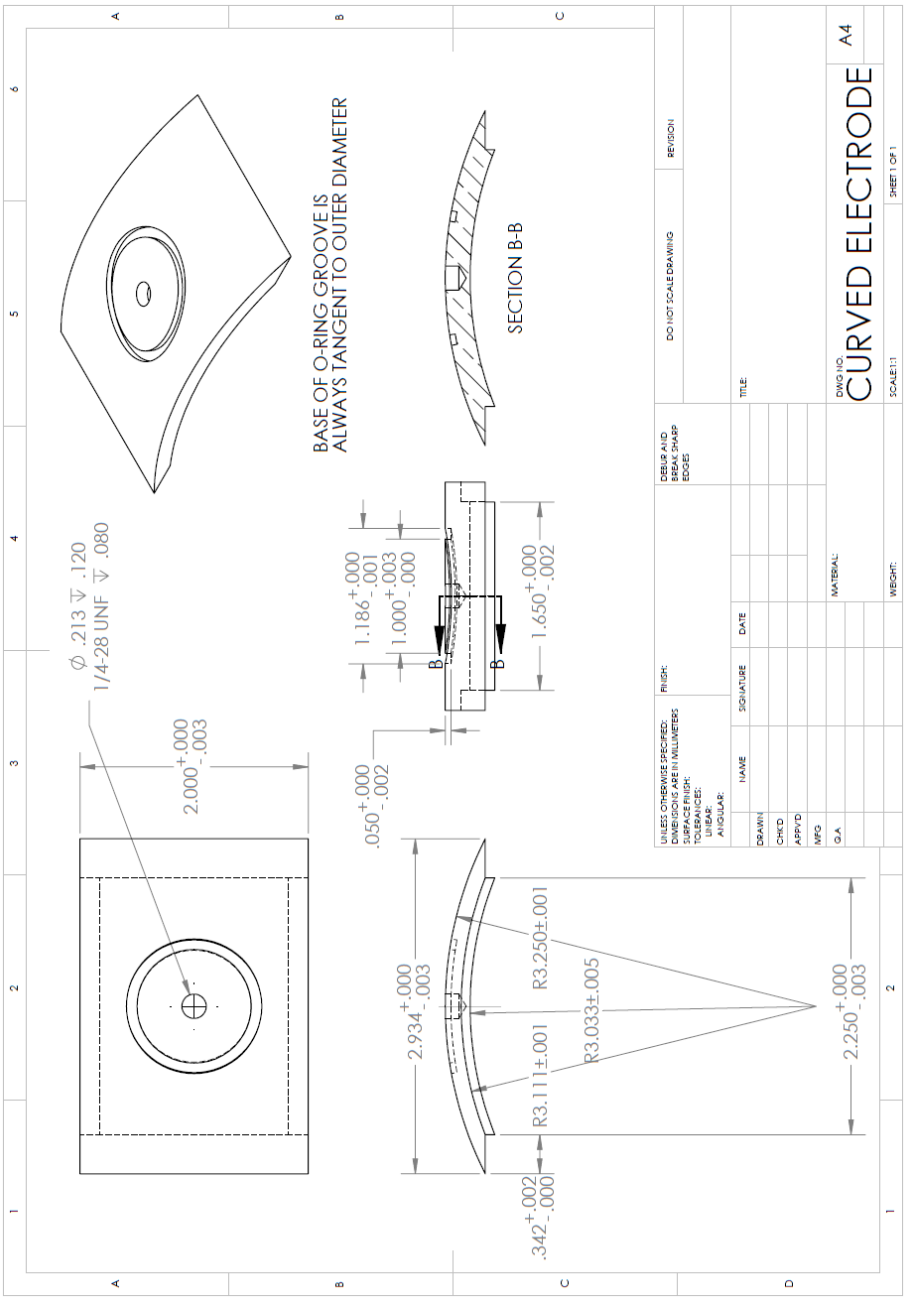

Figure 120. Drawing of brass electrode